

Time Series Searching, Forecasting, and
Classification with Applications in Bioinformatics
時系列の探索・予測・分類とその生命情報学
への応用

Coleman Yu
余 浩旻

Abstract

7

Time series data are ubiquitous across many different fields. Much of the data are inherently time series data. Additionally, some data, such as strings, images, and object shapes, that are not originally time series data, can be transformed into time series. Many data mining tasks, such as classification, clustering, and motif finding, have been defined for time series data. Hence, by developing appropriate transformation methods, we can apply a plethora of well-established time series methods to our problems.

8
9
10
11
12
13
14

This thesis contributes three aspects in time series data mining and bioinformatics. They are a novel application of time series classification to solve complex biological problems by transforming biological data into time series and developing a more expressive distance measure framework that removes certain underlying assumptions.

15
16
17
18
19

In the first part, we demonstrate the utility of time series analysis in bioinformatics by studying the problem of predicting Human Dicer Cleavage Sites. Recall that bioinformatics operates at the intersection of biology, biotechnology, and informatics. In this work, we formulate a specific biology problem, which is predicting Human Dicer Cleavage sites in microRNA biogenesis, into a machine learning framework. In particular, this is a multivariate time series classification problem, which is the informatics component of bioinformatics. Due to current limitations in biotechnology, we are constrained to using 1-D RNA sequence inputs rather than 2-D or 3-D data, because these are more expensive to obtain. We propose MTSCCleav, a method that encodes RNA sequences and the probabilities of base pairs in predicted secondary structures into time series data. To the best of our knowledge, we are the first to make use of the probabilities of base pairs in this kind of classification task on RNA data. By doing this, we frame the problem of predicting Human Dicer Cleavage sites into a Multivariate Time Series Classification (MTSC) problem. Existing approaches rely on opaque deep neural networks or complex feature engineering. They are slow, and the feature engineering is over-designed. In contrast, our approach is simple, intu-

20
21
22
23
24
25
26
27
28
29
30
31
32
33
34
35
36

37 itive, and computationally efficient. The proposed transformation methods allow
38 us to use any well-established time series tools to analyze this biological problem.
39 Experiments demonstrate that MTSCCleav achieves comparable and even better
40 accuracy to state-of-the-art methods while delivering a 3.7X to 28.8X speedup.
41 Furthermore, our perturbation experiments reveal that regions near the center of
42 pre-miRNAs are essential for cleavage-site prediction, consistent with the existing
43 literature.

44 In the second part, we address the limitations of existing similarity measures.
45 Similarity search is a core subroutine in time series data mining tasks. For ex-
46 ample, recent studies show that a simple 1-NN classifier with an appropriate dis-
47 tance measure can outperform many advanced, complicated methods. While Dy-
48 namic Time Warping (DTW) and Uniform Scaling (US) are prevailing measures
49 for handling local distortions and global scaling, respectively, and some studies
50 have demonstrated that combining both DTW and US is necessary to obtain
51 meaningful results. Current approaches apply a single scaling factor to the entire
52 sequence. We argue that since distinct phases of a process often evolve at different
53 speeds, a single scaling factor is insufficient. We introduce the first distance mea-
54 sure framework, namely PSD, that achieves invariance to multiple scaling factors.
55 We also provide speed-up techniques to enable efficient computation of the PSD.
56 Experiments show that PSD better reflects the similarity between time series with
57 multiple phases, and that the identified phases (segmentation) provide a clearer
58 understanding of the data.

59 In the third part, we study a time series primitive, namely matrix profile, in
60 the application of time series forecasting. For a given time series T and an in-
61 teger m , the matrix profile provides the information about (1) the location of
62 its nearest neighbor and (2) the distance between it and the nearest neighbor of
63 **each** m -subsequence in T . Obviously, the matrix profile also provides us the in-
64 formation for the k -nearest neighbors of each subsequence simply by running the
65 same algorithm for k times. In our application, we are only interested in the left
66 nearest neighbors of each subsequence because they refer to the historical occur-
67 rences. We can obtain the immediate subsequences of these historical occurrences
68 as covariates to feed into the forecaster to improve its accuracy.

69 Collectively, this thesis advances the fields of time series data mining and bioin-
70 formatics by demonstrating the use of time series analysis to address fundamental
71 biological questions and proposing a new, more expressive distance measure frame-
72 work.

Acknowledgements

73

To begin, I want to express my deepest gratitude to my PhD supervisor at Kyoto University, Prof. Tatsuya Akutsu. I thank him for his kindness and patience. He is a brilliant researcher who can explain complex concepts simply. In a seminar, he showed that simply using clear notation makes presentations much easier to follow. More importantly, he helps students when they are in “valleys” in their lives. When a car is off track, it needs a push—so do people. I am equally indebted to my MPhil supervisor at The Hong Kong University of Science and Technology (HKUST), Prof. Raymond Chi-Wing Wong. He has continued to help and advise me even after I graduated from HKUST.

Akutsu-sensei taught me the importance of reading good materials. In the weekly seminars, he organized reading seminars, assigning some of his favorite books for us to read and discuss. His favorite book is “Probability and Computing” by Mitzenmacher and Upfal. Additionally, through the journal club he organized, students were asked to present the core ideas from their ten selected papers published in leading venues, such as Nature, Science, Cell, and PNAS. Reading beyond my fields helped me identify research gaps others missed. I think some great ideas are born when we merge the ideas from different fields. He also emphasized the importance of mathematics and proof. It is what computer scientists can stand out in the field of bioinformatics. I think it becomes especially true now, since advances in AI make it possible for almost everyone to code (i.e., Vibe coding). He advised me to use the existing tools, libraries, and studies to leverage my own research. He also taught me that a good researcher must master both oral and written presentation; otherwise, others may misinterpret your talent and the effort you put in. When we are reading a paper, he urges us to identify the novelty and analyze the pros and cons of the paper.

Raymond taught me the power of focus and “First Principles”. I was always surprised that he did not use reference management software like Zotero, preferring to annotate hard copies and even type .bib files manually. He told me that when he starts to do research, he will print out the papers and get focused on the

stack of papers (hard copies) in front of him. I am not saying it is beneficial not to use tools, but I want to emphasize the power of focus that underlies his work routine. He taught me that every good research starts with a set of good papers. He also emphasized that there is no right or wrong in research, only what you choose to do about it. His research receipt works as follows. When you are tackling a problem, you first review the relevant existing studies to understand the state of the art (SOTA) for it. If the existing work addresses your particular problem, you can apply and adapt it to your problem setting. But most of the time, since your problem must be a particular version of a general problem, the existing general solution should not work well for it. It means that you have some room to improve it. And this is the research gap!. It reminds me of when we deal with the NP-complete problem. As Kleinberg and Tardos's Algorithm Design (Chapter 10) suggests, an NP-complete problem (assuming $P \neq NP$) does not allow us to have an algorithm that possesses all three of the following desired properties simultaneously: Efficiency, Correctness, and Generalization. Hence, it is sometimes preferable to address a specific instance of the problem rather than the general one. He also emphasized the theory. He consistently noted that you need to add theory to the paper to strengthen it. He always mentioned that you need three motivations (why you are doing it) and three contributions (what you have done). Sometimes, I ask why he can write so fast, and he replies, "If you know what you are doing, then you write fast.". He also taught me that when you don't know some of the ideas, you just go back to the original idea. Doing a "deep first search" can help you reach the first principle, a concept that Elon Musk, one of the greatest entrepreneurs of our time, always emphasized. Without these two supervisors, I would not have made it this far. I could not have finished this program.

I would like to take this opportunity to share some of my thoughts on my PhD journey. I hope the readers may learn something from what I have gone through. My PhD journey was, to quote Dickens, "the best of times and the worst of times", and to quote Churchill, "This was their finest hour". For the best parts, it allows me to explore both in my daily life and in my research. I tried many things, walked many roads, drank many colas and alcohol, and met many people. This helped me see problems from new perspectives. Regarding the worst parts, I am reminded of a quote from one of my favorite movies, "Les Choristes": "Fond de l'étang". It literally means "Bottom of the Pond". At times, I felt like a frog at the well's bottom, trying hard to get out. Research is fun but also hard. Research is about exploring something new. It is about publishing (so others can learn from

it). When I am stuck, the best solution is to aim for a reachable, well-defined 140
goal. The goal should be clear, with obvious rewards and requirements. Also, 141
make sure the effort of your actions can be accumulated. Like the frog, do not 142
jump randomly, but aim to move to stable platforms towards escape. Then, each 143
jump matters for your progress. Two of the materials helped me; they are “Eat 144
the Frog!” and “THE PH.D. GRIND”. 145

I would like to thank my thesis committee members. I would like to acknowl- 146
edge Tamura-sensei and Mori-sensei (a former member) of the Akutsu laboratory. 147
Tamura-sensei taught me to focus on the input-output relationship when encoun- 148
tering new algorithms/methods, and Mori-sensei introduced me to the fascinating 149
application of time-series analysis to gene expression data, especially in trajectory 150
inferences (i.e., pseudotime). I would like to thank the many communities that 151
made my life in Japan colorful. Thank you to the people of the dormitories where 152
I lived at the Uji and Yoshida campuses. I am grateful to my Japanese language 153
teachers. I also cherish the friends I met through Akutsu’s laboratory and the 154
extracurricular activities, including Kendo, Table Tennis, Naginata, Karate, and 155
Aikido. I also met many interesting people from various international student 156
events. 157

I am honored to receive the Asian Future Leaders Scholarship Program (AFLSP) 158
scholarship to support my studies in Japan. I have made a great choice by enrolling 159
in Kyoto University Design School, which has provided me with many valuable 160
interdisciplinary experiences and opportunities to meet people outside my field. 161
In this program, I have conducted fieldwork in Okinawa, Hong Kong, and Bali, a 162
rare opportunity for researchers in computer science. I would also like to thank 163
the Institute for Chemical Research (ICR) for the Research Assistant position in 164
the Akutsu laboratory. 165

Finally, I would like to express my deepest gratitude to my family and my 166
friends who have stayed by my side with their countless acts of support; I have 167
nothing to return to them but my love and time. 168

A special acknowledgment goes to my niece. As you grow up, I hope you 169
explore the world and fulfill your eagerness for knowledge. Find materials that 170
interest you. One day, you might find this thesis online and, I hope, find it worth 171
reading and inspiring. 172

List of Publications

173

This thesis is based on the following papers.

174

- (Chapter 3) **Coleman Yu**, Raymond Chi-Wing Wong, and Tatsuya Akutsu, “MTSCCleav: a Multivariate Time Series Classification (MTSC)-based Method for Predicting Human Dicer Cleavage Sites”, submitted to *IEEE Access*, under review
175
176
177
178
- (Chapter 4) **Coleman Yu**, Tatsuya Akutsu, and Raymond Chi-Wing Wong, “Scaling with Multiple Scaling Factors and Dynamic Time Warping in Time Series Searching”, submitted to *IEEE Access*, under review
179
180
181
- (Chapter 5) **Coleman Yu**, Raymond Chi-Wing Wong, and Tatsuya Akutsu, “Leveraging Nearest Neighbors for Time Series Forecasting with Matrix Profile”, in preparation
182
183
184

Other publications

185

- **Coleman Yu** and Raymond Chi-Wing Wong, “A Melody Composer for both Tonal and Non-Tonal Languages”, the 43rd International Computer Music Conference 2017, Shanghai, China on 16-20 Oct, 2017
186
187
188
 - In this study, we apply a data mining method called frequent pattern mining to capture the relationships between the pitch trend in the melody and the tone trend in lyrics and use these relationships to create a new melody for the user-given lyrics. The pitch trend and the melody trend are both time series data. It motivates me to do time series analysis from a data mining perspective.
189
190
191
192
193
194
- Yi Zheng, Bogdan Enescu, Jianchang Zhuang, and **Coleman Yu**, “Data replenishment of five moderate earthquake sequences in Japan, with semi-automatic cluster selection”, *Earthquake Science*, 34:310-322, 2021
195
196
197

- 198 – In this study, we apply a data mining method called DBSCAN, which
199 is a clustering method, on seismicity data, to automatically select the
200 nearest significant earthquake cluster of a given mainshock. The clus-
201 tering results are then fed into a downstream replenishment method
202 to discover missing early aftershocks, which follow relatively large or
203 moderate earthquakes.

204 Poster presentations

- 205 • **Coleman Yu** and Tatsuya Akutsu, “Aligning gene expression time series
206 with invariance to uniform scaling with multiple scaling factors”, Inter-
207 national Workshop on Bioinformatics and Systems Biology, Boston, USA
208 (IBSB 2018) on 16-18 July, 2018

- 209 – In this study, we present an idea that, for time series analysis, rather
210 than focusing on the whole sequence analysis, it is more important to
211 focus on the subsequences of a time series. In this poster, we use gene
212 expression data as an example to explain. Genes are expressed over
213 time. But the expression rate is not a constant. The varying rate would
214 be discussed in Chapter 4. The importance of the subsequence has been
215 discussed in the framework of time series forecasting in Chapter 5. We
216 use a data mining primitive called Matrix Profile. Given a subsequence
217 Q with length m , we can find the nearest neighbor (location and the
218 similarity of it with Q) in another time series A . The underlying dis-
219 tance metric is z-normalized ED. If Q is an m -subsequence extracted
220 from A , it means that we annotate each m -subsequence with its nearest
221 neighbor information. To demonstrate that this nearest-neighbor infor-
222 mation is useful, we use it to improve a time-series forecasting model.
223 If information is useful covariates, the performance can be improved.
224 In addition, the usage of finding useful covariates to improve the final
225 prediction results has also been demonstrated in Chapter 3. In that ex-
226 ample, we find a covariate, which is the secondary structure, associated
227 with the probability of each base pair, for the mRNA sequence data,
228 as shown in Figure 3.1.

Contents

229

Abstract	i	230
Acknowledgements	iii	231
List of Publications	vii	232
List of Figures	xiii	233
List of Tables	xv	234
1 Introduction	1	235
1.1 Background	1	236
1.2 Contributions	2	237
1.3 Organization	2	238
2 Preliminaries	5	239
2.1 Distance Measures	5	240
2.1.1 Euclidean Distance (ED)	6	241
2.1.2 Dynamic Time Warping (DTW)	7	242
2.1.3 Derivative Dynamic Time Warping (DDTW)	7	243
2.1.4 Weighted Dynamic Time Warping (WDTW)	7	244
2.1.5 Weighted Derivative Dynamic Time Warping (WDDTW) . .	8	245
2.1.6 Shape Dynamic Time Warping (shapeDTW)	8	246
2.1.7 Amercing Dynamic Time Warping (ADTW)	9	247
2.2 Classification	9	248
2.2.1 Ridge Classifier	10	249
3 MTSCCleav: a Multivariate Time Series Classification (MTSC)-based Method for Predicting Human Dicer Cleavage Sites	11	251
3.1 Background	12	252

253	3.2 Methods	15
254	3.2.1 Data Preparation	16
255	3.2.2 Time Series Encoding	19
256	3.2.3 Time Series Classification	23
257	3.2.4 Evaluation Metrics	26
258	3.3 Results	27
259	3.3.1 Channel Ablation Study	28
260	3.3.2 Predictive Performance	30
261	3.3.3 Running Time Analysis	32
262	3.3.4 Subsequence Importance	33
263	3.3.5 Summary	33
264	3.4 Discussion	34
265	3.5 Concluding Remarks	35
266	4 Scaling with Multiple Scaling Factors in Time Series Searching	37
267	4.1 Background	38
268	4.2 Related Work	41
269	4.3 Preliminaries	42
270	4.3.1 Euclidean Distance (ED)	43
271	4.3.2 Dynamic Time Warping (DTW)	43
272	4.3.3 Uniform Scaling (US)	46
273	4.3.4 Uniform Scaling & Dynamic Time Warping (USDTW)	47
274	4.3.5 Lower Bounds for DTW and USDTW	47
275	4.4 Piecewise Scaling Distance	51
276	4.4.1 Piecewise Scaling & Dynamic Time Warping (PSDTW)	53
277	4.4.2 Speedup Techniques	55
278	4.4.3 Guided Distance	60
279	4.5 Experiments	60
280	4.5.1 Experimental Setup	60
281	4.5.2 Experimental Results	63
282	4.6 Concluding Remarks	67
283	5 Leveraging Nearest Neighbors for Time Series Forecasting with Matrix Profile	69
284	5.1 Background	69
285	5.2 Related Work	73
286	5.3 Method	74

5.3.1	Problem Formulation	74	288
5.3.2	Evaluation Method	75	289
5.3.3	Gradient Boosting Regression Tree (GBRT)	77	290
5.3.4	Matrix Profile	78	291
5.4	Experiments	80	292
5.5	Concluding Remarks	81	293
5.5.1	Future Work	81	294
6	Conclusion and Future Directions	85	295

List of Figures

296

2.1 Alignments.	6	297
3.1 Predicted secondary structure of the sequence S of pri-miRNA “hsa-let-7a-1” ¹ . Experimental evidence suggests that the two deviated mature miRNAs are $UGA \cdots GUU$ and $CUA \cdots UUC$. They are $S(6 : 27)$ and $S(57 : 77)$ (Both ends are inclusive.). The ends are highlighted in bold . Since $S(6 : 27)$ ($S(57 : 77)$) is near the 5' (3') end, we call it “5p (3p) mature miRNA”. The two scissors indicate the two cleavage sites. The color intensity of the nodes reflects their base-pair probability in this predicted secondary structure. The deeper the color, the higher the probability. The unpaired nodes are uncolored. The raw figure is generated by RNAfold web server ²	13	308
3.2 The overall pipeline of this study. Symbol notations: Cylinder - Dataset, Rectangle - Process, Parallelogram - Input / Output, Rounded Rectangle - Component.	15	311
3.3 Relationship of the proposed encoding methods.	19	312
3.4 Features generation in the transformation	24	313
3.5 Convolutions of HYDRA for each input time series with a set of random kernels w , organized into g groups with k kernels each.	25	315
3.6 CD diagrams of channel ablation study.	30	316
3.7 CD diagrams to compare different classifiers.	32	317
3.8 CD diagrams to compare different encoding methods.	32	318
3.9 Results of the perturbation experiment.	34	319
4.1 Applying nearest neighbor interpolation on Q , which result in Scaled Q , that can better reflect its similarity with C	39	321
4.2 Q and C are in different rates. A stretching version of Q is similar to a prefix of C , but not the whole C	39	323
4.3 Intuition of piecewise scaling (PS).	40	324

325	4.4	Z-normalization. Resulting time series have mean = 0 and std = 1.	43
326	4.5	Visualization of D with local constraints. The black cells form the warping path.	45
327			
328	4.6	Visualization of LB _{Keogh} and LB _{Shen}	49
329	4.7	Relationship of L_Q and L_C .	57
330	4.8	Visualization of the GunPoint dataset. Left (Right): A time series of the “Gun” (“Point”) scenario. Critical periods, such as “Aiming”, are annotated.	61
331			
332	4.9	The red solid time series shows an instant in the target set. The blue dashed time series shows an instant in the query set.	61
333			
334	4.10	Runtime and number of distance calls comparison of GunPoint dataset. (a)-(d) $P = 1$, (e)-(h) $P = 2$, (i)-(l) $P = 3$.	65
335			
336			
337	5.1	Flattening a 2D window of size $(1+M) \times w$ to a 1D vector of length $w+M$. The resulting vector serves as the <i>predictor</i> for the regressor. Its expected <i>response</i> is the vector of length h . The regressor learns from this predictor-response pair.	70
338			
339	5.2	The <code>left</code> (<code>right</code>) matrix profile and the <code>matrix profile</code> of a time series. The <code>matrix profile</code> shows the distances between each m -subsequence and its nearest neighbor, where m is a user-given value. The <code>left</code> (<code>right</code>) matrix profile shows the same information but is limited to its left (right) nearest neighbor. For a particular m -subsequence shown by the right gray box, its nearest neighbor is the left gray box, as indicated by the dashed line in the <code>left matrix profile</code> and the <code>matrix profile</code> . Similarly, the nearest neighbor of the left gray box is the right gray box, as indicated by the dashed line in the <code>right matrix profile</code> and the <code>matrix profile</code> . The first (last) point in each box is denoted by a <code>red</code> circle (triangle). h denotes the length of the immediate subsequence of the nearest neighbor. Intuitively, this subsequence should be similar to the immediate subsequence (i.e., future) of the right gray box. To note, the <code>left</code> (<code>right</code>) matrix profile starts (ends) at a later (earlier) index because the corresponding nearest neighbor with length m does not exist.	71
340			
341			
342			
343			
344			
345			
346			
347			
348			
349			
350			
351			
352			
353			
354			
355			
356			

List of Tables

357

3.1	Selected representative records from miRBase. For the last two columns, the first line shows the name, the second line shows its location in the original sequence, and the third line indicates whether its existence has experimental evidence. The selected one is highlighted in bold	358 359 360 361 16 362
3.2	The whole sequence of “hsa-let-7a-1” and its predicted secondary structure by RNAfold. The corresponding positions of the two mature miRNAs and the probability of the unpaired “U” are highlighted in bold	363 364 365 17 366
3.3	The first row shows the “four strings” of “hsa-let-7a-1”. Their complementary strands are shown in the second row. As a whole, they are referred to as the “eight strings”.	367 368 369 18 369
3.4	Time series encoding. P is the corresponding base-pair probability sequence of S . $p_i = 1$ if we encode S without incorporating base-pair probability sequence.	370 371 21 372
3.5	Comparison of rocket-based classifiers [1]. $\mathcal{N}(0, 1)$: a standard normal distribution, $U(0, 1)$: a uniform distribution between 0 and 1, 1 st order difference: $\Delta T = t_2 - t_1, t_3 - t_2, \dots, t_n - t_{n-1}$	373 374 26 375
3.6	Channel ablation study. The best results are highlighted in bold	376 29
3.7	Performance on the 45 combinations between encoding methods and the ROCKET-based classifiers. The best results are highlighted in bold	377 378 31 379
3.8	Comparative analysis between MTSCCleav with the best combination of the encoding method and classifier, with the SOTA, Di-Cleave, on the three datasets. The best results of using MiniROCKET have also been shown to compare the computational efficiency. The best results are highlighted in bold	380 381 382 383 31 384
4.1	Details of the ten datasets for the experiments	63 385

386	4.2	The accuracy comparison for eight distance measures of the Gun-	
387		Point dataset	64
388	4.3	The accuracy comparison for six PSED-guided distance measures	
389		of the GunPoint dataset	64
390	4.4	The accuracy comparison for eight distance measures of the ten	
391		datasets	66
392	4.5	The accuracy comparison for six PSED-guided distance measures	
393		of the ten datasets	66
394	4.6	The number of distance calls and runtime on PSED_vanilla and	
395		PSED_parallel_bsf of the ten datasets	67
396	5.1	Dataset Statistics. N is the number of time series in the dataset,	
397		while $ T = n$ is the length of each time series. “rate” refers to the	
398		measuring rate. w is the size of the look-back window. h is the size	
399		of the forecasting window, also known as the forecasting horizon.	
400		T_{train} is the training subsequence of T . T_{test} is the test subsequence	
401		of T . To note, $ T_{\text{train}} + T_{\text{test}} = n$	80
402	5.2	Experimental Results without original covariates (bold represents	
403		the best result and underlined represents the second best) (* refers	
404		to the results reported from [2]).	81
405	5.3	Experimental Results with original covariates (bold represents the	
406		best result and underlined represents the second best) (* refers to	
407		the results reported from [2]).	81

Chapter 1

408

Introduction

409

1.1 Background

410

Human generates a ton of data nowadays. We are producing more new data in one single day today than in the first twenty-one centuries of AD combined. We are drowning in information but thirsty for knowledge. It is natural for us to develop computational methods to accelerate the process of “harvesting” knowledge from information.

411

412

413

414

415

Computational tasks focus on the relationship between input and output. We would like to find the hidden function behind. To note, there are two ways to solve a problem. One is the algorithmic approach, and the other is the machine-learning approach.

416

417

418

419

There are two large categories of machine learning. They are supervised learning and unsupervised learning. Classification may be the most intuitive form of supervised learning. The input is data points with labels. We learn a model from the relationship between data points and the labels. The model predicts the labels for the new data points. They have many applications. For example, in medical applications, it involves classifying patients as healthy or diseased, or tumors as benign or malignant. The term “supervised” means the model has access to labeled data. In other words, it requires labeled training examples that provide ground truth. So, the model can learn the boundary between the categories. Our first study focuses on a classification problem in biology.

420

421

422

423

424

425

426

427

428

429

A representative of unsupervised learning is undoubtedly clustering. We aim to group data into distinct clusters. The key difference is that the data lack predefined labels. By grouping them, we aim to identify natural patterns hidden in the data. One example is clustering cells based on their gene-expression profiles. These

430

431

432

433

434 clusters might reveal distinct cell types. Note that we do not have the ground
435 truth for the cluster set. In bioinformatics, we typically use enrichment analysis
436 to determine whether specific gene functions are enriched in these clusters. Cell
437 types often show enrichment for genes responsible for specific functions. This set of
438 genes defines their biological role. In clustering, we first need to define a measure
439 of similarity between two objects and decide what details should be ignored. This
440 is called invariance. For example, in image classification, it should be invariant to
441 zooming and rotation.

442 1.2 Contributions

443 In this study, our contributions mainly include three parts. First, in chapter 3, we
444 demonstrate a machine learning approach to analyze a biology problem. We pro-
445 pose the usage of the base pair probability sequence from the predicted secondary
446 structure of RNA sequence as new information for the classification task. We
447 apply Rocket-based classifiers to identify the human dicer cleavage sites. Because
448 of the simplicity of the transformation method and the classifiers, our proposed
449 method achieves 3.7X to 28.8X speedup while achieving better or comparable re-
450 sults than the current state-of-the-art method. Second in Chapter 4, we solve an
451 algorithmic problem on distance measure. We propose a new distance measure
452 framework, namely PSD, that can incorporate any existing distance measures to
453 achieve invariance for two time series with multiple rates (i.e., different scaling fac-
454 tors). Experiments show that our methods outperform ED, DTW and the other
455 five DTW-based methods. Besides, we propose to use the segmentation result
456 returned by PSD to improve the accuracy of other distance measures. Third in
457 Chapter 5, we improve a forecaster with the usage of a data mining primitive,
458 namely Matrix Profile. We propose leveraging left nearest neighbors for each
459 forecasting window as new covariates to improve the accuracy of the underlying
460 forecaster. We use a simple gradient boosting regression tree as the underlying
461 forecaster. The experiment shows that this simple method can improve the accu-
462 racy.

463 1.3 Organization

464 In Chapter 2, we review some of the basic knowledge in biology and time series
465 data mining, in particular, we focus on distance measures and Rocket-based clas-
466 sifiers. In Chapter 3, we introduce our study of the problem of predicting human

dicer cleavage sites. We proposed a novel approach to frame this task as a multivariate time series classification problem by introducing nine encoding methods and making use of Rocket-based classifiers. In Chapter 4, we introduce a new distance measure framework, namely PSD. It releases the assumption that there is only one scaling factor existing throughout the whole time series. In Chapter 5, we introduce how to create new covariates in time series forecasting using matrix profile. This method can improve the accuracy of the existing forecaster by providing useful covariates. In Chapter 6, we give a conclusion to these two studies and provide future work on them.

Chapter 2

476

Preliminaries

477

In this chapter, we provide background on time series, with a focus on distance measures and classification, particularly the ridge classifier, which is used in the ROCKET-based classifiers for time series classification. The remaining preliminary knowledge will be provided in the corresponding chapters. Section 2.1 gives an overview of the existing distance measures used in the evaluation in Chapter 4. Section 2.2 reviews the additional knowledge about the classifiers used in Chapter 3. We start with the definition of a time series.

478

479

480

481

482

483

484

2.1 Distance Measures

485

A general form of a time series T is an ordered pair of n real-valued variables, $T = (b_1, c_1), (b_2, c_2), \dots, (b_n, c_n)$, where b_i is the behavioral attribute and c_i is the contextual attribute, where $1 \leq i \leq n$. c_i refers to the time stamp at which the measurement b_i is taken. Since the measurements are always taken in a uniform manner, t_i is simply incrementing from 1 to n uniformly. Hence, we can represent a time series more concisely as $T = t_1, t_2, \dots, t_n$, where $t_i = b_i$.

486

487

488

489

490

491

We may be interested not only in the entire time series but also in a segment of it, called a subsequence. A subsequence $T(i : j)$ of a time series T is a shorter time series, which is a contiguous subset of time points in T , that starts from position i and ends at position j . Formally, $T(i : j) = t_i, t_{i+1}, \dots, t_j$, where $1 \leq i \leq j \leq n$. We call $T(1 : m)$ as the prefix of length m of T , m -prefix in short.

492

493

494

495

496

To quantify the similarity between two time series, we need to define a distance measure, also known as a similarity measure, between them. Many distance measures have been proposed in the literature. Among them, the most established measures are undoubtedly Euclidean Distance (ED) and Dynamic Time Warping

497

498

499

500

501 (DTW). They are representatives of the two board classes of distance measures,
 502 namely “lock-step” and “elastic”.

503 **2.1.1 Euclidean Distance (ED)**

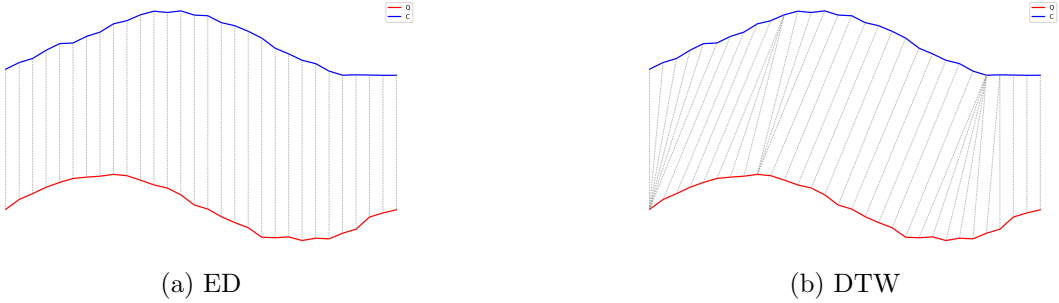


Figure 2.1: Alignments.

504 ED is a lock-step distance measure. Given two time series Q and C with the
 505 same length n , it compares the time point q_i of Q with the time point c_i of C at the
 506 same time (index). Note that, traditionally, lockstep distance measures require
 507 the two time series to have the same length because of the one-to-one alignment,
 508 as shown in Figure 2.1. However, in the setting of query by content, where it is
 509 always the case that $|Q| < |C|$, we can still apply a lock-step distance measure
 510 by either comparing Q with $C(1 : |Q|)$ or padding Q using its last element to
 511 lengthen it to the same length of C . Minkowski distance is a generalization of
 512 Euclidean distance. Minkowski distance is the L_p -norm of the difference between
 513 the two time series X and Y , defined as:

$$D(X, Y) = \left(\sum_{i=1}^n |x_i - y_i|^p \right)^{\frac{1}{p}} \quad (2.1)$$

514 When $p = 2$, it corresponds to the Euclidean distance. When $p = 1$, it corresponds
 515 to the Manhattan distance. When $p = \infty$, it corresponds to the Chebyshev dis-
 516 tance. In our studies, we focus on the Euclidean distance. Other lock-step distance
 517 measures include Pearson correlation distance. It accounts for the linear associa-
 518 tion between the two time series using the Pearson correlation coefficient. To note,
 519 there is another measure called Edit Distance for strings. And Edit Distance is
 520 also sometimes abbreviated as ED in string processing or bioinformatics. In this
 521 study, we focus on time series analysis and use ED to denote Euclidean distance
 522 rather than edit distance.

2.1.2 Dynamic Time Warping (DTW) 523

Dynamic Time Warping is an elastic measure [3]. In contrast to lock-step distance measures, elastic distance measures allow one-to-many point matching, as shown in Figure 2.1. The one-to-many point matching allows the elastic distance measures to warp in the time axis (i.e., temporally) such that it can handle the local temporal distortions. While it will be detailed in Chapter 4, it is briefly explained here. In short, it minimizes the cumulative distance between two time series, subject to constraints, by finding an optimal warping path W^* in a cost matrix, where W is the set of all possible paths. The constraints typically are (1) Boundary conditions, (2) Continuity, and (3) Monotonicity. 524
525
526
527
528
529
530
531
532

2.1.3 Derivative Dynamic Time Warping (DDTW) 533

The Derivative Dynamic Time Warping (DDTW) is a variant of DTW [4]. Instead of comparing original raw values, it compares two time series using their first-order derivatives, but with an approximation. In DTW, a point on a rising trend may be mapped to a point on a falling trend. It goes against our intuition. It can be solved by comparing their first-order derivatives, which encodes the slope information. The derivative T' of a time series T is computed approximately as follows. 534
535
536
537
538
539

$$t'_i = \frac{(t_i - t_{i-1}) + \frac{t_{i+1} - t_{i-1}}{2}}{2} \quad (2.2)$$

This estimate is simply the average of “the slope of the line through t_i and t_{i-1} (i.e., its left neighbor)” and “the slope of the line through t_{i-1} (i.e., its left neighbor) and t_{i+1} (i.e., its right neighbor)”. The $1/2$ term in the second item of the numerator comes from the fact that the separation in time of the t_{i-1} and t_{i+1} is 2. Note that the estimate is not defined for the first and last elements of the time series in the above equation. In these boundary cases, we use the estimates of the second and penultimate (i.e., the second-to-last thing) as the estimates for the first and last elements, respectively. 540
541
542
543
544
545
546
547

2.1.4 Weighted Dynamic Time Warping (WDTW) 548

The Weighted Dynamic Time Warping (WDTW) is a variant of DTW [5]. It is a penalty-based DTW designed to prevent pathological paths. Recall that a warping window (e.g, Sakoe-Chiba band) is enforced on the cost matrix of DTW, such that some paths are excluded. Only the paths that reside entirely in the 549
550
551
552

553 warping window are feasible. This constraint may be too strict. WDTW uses a
 554 softer way for the same purpose. Instead of using a window to forbid the alignment
 555 of x_i and y_j that are far away in time. WDTW weights the cost of such alignment
 556 by multiplying it by a modified logistic weight function (MLWF) $\omega(k)$, defined as
 557 follows.

$$\omega(k) = \frac{\omega_{\max}}{1 + \exp(-g \cdot (k - m_c))} \quad (2.3)$$

558 Where:

- 559 • $k = |i - j|$. It is the phase difference (i.e., distance on the time axis from
 560 the diagonal. The diagonal refers to the line where $i = j$.)
- 561 • ω_{\max} is the desired upper bound for the weight parameter, which is suggested
 562 to be set to 1.
- 563 • m_c is the midpoint of a sequence. $m_c = m/2$.
- 564 • g is a constant that controls the level of penalization. It controls the curva-
 565 ture (slope) of the function.

566 Intuitively, if x_i and y_j are far apart temporally, it will have a larger weight to
 567 discourage their alignment and vice versa.

568 2.1.5 Weighted Derivative Dynamic Time Warping (WD- 569 DTW)

570 [5] also proposed the weighted version of DDTW. In brief, a weight is applied to
 571 the local cost function when computing DTW on the first derivative.

572 2.1.6 Shape Dynamic Time Warping (shapeDTW)

573 The Shape Dynamic Time Warping (shapeDTW) is a variant of DTW [6]. The
 574 main modification to the original DTW is the way the local distance between
 575 points is computed. Recall that DTW compares single scalar points. shapeDTW
 576 compares local descriptors. The local descriptors are constructed using a sliding
 577 window on the original series, such that for each point x , a L -subsequence with x
 578 as the center is extracted to compute the higher-level feature of x . L is the user-
 579 given length of the subsequence to consider. By default, it is set to 15. There are
 580 several ways to construct such a descriptor. For example, a raw subsequence (i.e.,
 581 a set of neighbor points surrounding the point of interest), Piecewise aggregate
 582 approximation (PAA) [7, 8], slope, derivative, HOG-1D [9].

Then, the distance between descriptors is calculated rather than between raw values. When a raw subsequence is chosen to construct the local descriptors, a common metric used for comparing two local descriptors is the Euclidean distance. In the evaluation, a raw subsequence is chosen to construct the local descriptors.

2.1.7 Amercing Dynamic Time Warping (ADTW) 587

The Amercing Dynamic Time Warping (WDTW) is a variant of DTW [10]. It is also designed to constrain the amount of warping, as in cDTW and WDTW. While cDTW imposes a hard window and WDTW uses multiplicative weights (i.e, MLWF), ADTW introduces an additive penalty for non-diagonal alignment. The word “Amercing” means “fining”. The non-diagonal alignments are required to pay the fines. Unlike WDTW, which uses a multiplicative weight based on the position of the alignment, ADTW applies an additive penalty ω based on the action of warping. The non-diagonal alignments are penalized. Formally, the recursive relation for ADTW is defined as:

$$D(i, j) = d(q_i, c_j) + \min \begin{cases} D(i - 1, j - 1), \\ D(i - 1, j) + \omega, \\ D(i, j - 1) + \omega \end{cases} \quad (2.4)$$

ADTW penalizes the last two alignment actions. ω is a user-given hyperparameter. It should be a non-negative scalar constant. In practice, it is defined through cross-validation, which determines the optimal ω by training on a subset of data or heuristic search, which searches values in a user-given range.

To note, ADTW generalizes ED and DTW. If $\omega = 0$, no need to pay the fine for the non-diagonal alignment, which reduces to DTW. If $\omega \rightarrow \infty$, the non-diagonal alignment becomes prohibitive, and it reduces to ED.

2.2 Classification 604

In Chapter 3, we use ROCKET (RandOm Convolutional KErnel Transform) and its variants, including MiniRocket, MultiRocket, and Hydra, as the time series classifiers on the time series resulting from our encoding methods. Technically, they are not classifiers in their own right but rather feature extractors. These

609 features are also called summary statistics. They are high-dimensional feature
610 vectors that capture the characteristics of the original time series. The summary
611 statistics are then fed to the classifiers to output the final classification results.

612 2.2.1 Ridge Classifier

613 The classifier that is usually chosen to work with ROCKET and its variants is
614 a ridge classifier. The main advantage of it is speed. ROCKET and its variants
615 generate a large number of features.

616 A ridge classifier is a wrapper that uses a ridge regression model as a routine to
617 perform classification. It first maps the categorical labels of targets into continuous
618 numbers, does the regression, and finally thresholds the numerical results from the
619 regressor to obtain the classification result.

620 Given a training dataset $D = \{(x_i, y_i)\}_{i=1}^n$ with n instances, where $x_i \in \mathbb{R}^P$ is
621 the feature vector with P dimensions and $y_i \in \{+1, -1\}$ is its label, it minimize
622 the following optimization function.

$$\min_w \left(\sum_{i=1}^n (x_i^T w - y_i)^2 + \lambda \|w\|_2^2 \right) \quad (2.5)$$

623 Where $\|w\|_2^2 = \sum_{j=1}^P w_j^2$ is the L_2 norm of the weight vector and $\lambda > 0$ control
624 the penalty. We explain the equation in brief. There are two terms inside the
625 bracket. The first term is simply the sum of the residual, same as the one in the
626 least squares method. The second term is called the L_2 penalty and is used to
627 introduce bias in the fit to avoid overfitting. Hence, λ serves as a regularization
628 hyperparameter between the trade-off between bias and variance.

629 Since the above optimization function in a ridge classifier has a closed-form
630 solution, it can be solved using linear algebra rather than iterative optimization,
631 as in logistic regression. Besides, the generated features by the random kernels
632 in ROCKET and its variants are highly correlated. Ridge regularization, also
633 known as the L_2 norm, can handle this case. Ridge regression shrinks regression
634 coefficients toward zero by adding an L2 penalty. It reduces model complexity
635 and helps with multicollinearity.

Chapter 3

636

MTSCCleav: a Multivariate Time Series Classification 637

(MTSC)-based Method for Predicting Human Dicer Cleavage Sites 638

639

640

641

MicroRNAs (miRNAs) are small non-coding RNAs (ncRNAs) that regulate gene expression at the post-transcriptional level, thereby playing essential roles in diverse biological processes. The biogenesis of miRNAs requires dicer to cleave at specific sites on the precursor miRNAs (pre-miRNAs). Several machine learning approaches have been proposed to predict whether an input sequence contains a cleavage site. However, they rely heavily on complex feature engineering or opaque deep neural networks. It results in a lack of generalizability and a long running time. There is a need for an alternative modeling paradigm that is accurate, fast, and simple.

We proposed a novel approach to frame the task as a multivariate time series classification problem. Nine encoding methods have been proposed to convert the sequence and the predicted secondary structure into a time series. We also leveraged the probabilities of the base pairs in the predicted secondary structure. Computational experiments demonstrate that our proposed method can achieve better or comparable results in terms of using a simpler, more intuitive model and less computational time. It achieves 3.7X to 28.8X speedup. Through perturbation

658 experiments, we found that regions close to the center of pre-miRNAs are essential
659 for predicting human dicer cleavage sites.

660 By transforming the RNA sequence and its secondary structure information
661 into a time series and utilizing simple, state-of-the-art time series classifiers, we
662 achieved comparable or even superior performance in a simpler and faster manner.

663 Code is available at: <https://github.com/colemanyu/time-series-classification-cleavage>.

665 3.1 Background

666 One of the most important theories in molecular biology is the central dogma. It
667 depicts the flow of genetic information [11, 12]. Proteins are the functional units.
668 The information stored in DNA is used to create them. Genes (segments) in DNA
669 are used as templates for messenger RNAs (mRNAs) synthesis. An mRNA acts
670 as a set of instructions to assemble a chain of amino acids, which form a linear
671 polypeptide. To become biologically active, this chain is folded into a specific 3D
672 structure, a proper configuration that enables it to perform its desired functions.
673 This folded polypeptide is called a functional protein, or simply a protein. This
674 entire process closely resembles how a computer program runs on a machine. The
675 source code does not function by itself. First, it is translated into an assembly
676 code (a lower-level, less human-readable form) and then into an executable file
677 that can actually perform the intended tasks [13].

678 These mRNAs are called “coding RNAs” because they code for proteins. There
679 are other genes in which the final product is the RNA molecule itself. They are
680 called non-coding RNAs (ncRNAs). Two types of small ncRNAs are particularly
681 important. They are microRNAs (miRNAs) and small interfering RNAs (siR-
682 NAs). Their discovery was recognized with the 2006 Nobel Prize in Physiology or
683 Medicine¹, awarded for work completed only eight years prior [11].

684 In this study, we focus on miRNAs. An miRNA can regulate the expression
685 of several proteins. Hence, understanding the biogenesis of miRNAs is of great
686 value. It involves the processing of primary miRNAs (pri-miRNAs). RNAs are 3D
687 molecules. However, it is hard to measure the 3D structure (tertiary structure)
688 from the experiment and predict it from 1D sequence. We can understand their
689 properties by analyzing their 1D sequence or 2D structure, known as secondary
690 structure. RNA sequence is easily obtained through sequencing. The sequence

¹The Nobel Prize in Physiology or Medicine 2006 - NobelPrize.org:
<https://www.nobelprize.org/prizes/medicine/2006/summary/> (Accessed on: 2025-06-13).

and its predicted secondary structure of a pri-miRNA “hsa-let-7a-1” is shown in 691
 Figure 3.1. 692

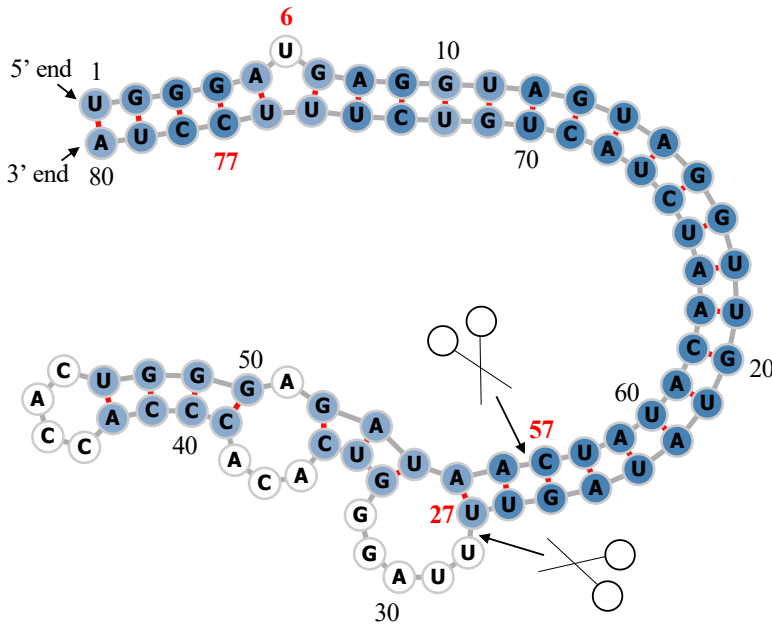


Figure 3.1: Predicted secondary structure of the sequence S of pri-miRNA “hsa-let-7a-1”². Experimental evidence suggests that the two deviated mature miRNAs are $UGA \cdots GUU$ and $CUA \cdots UUC$. They are $S(6 : 27)$ and $S(57 : 77)$ (Both ends are inclusive.). The ends are highlighted in **bold**. Since $S(6 : 27)$ ($S(57 : 77)$) is near the 5' (3') end, we call it “5p (3p) mature miRNA”. The two scissors indicate the two cleavage sites. The color intensity of the nodes reflects their base-pair probability in this predicted secondary structure. The deeper the color, the higher the probability. The unpaired nodes are uncolored. The raw figure is generated by RNAfold web server³.

Recall that a pri-miRNA contains a hairpin loop, also called a stem loop. A 693
 microprocessor complex comprising Drosa and DCGR8 cleaves the pri-miRNA 694
 to form a precursor miRNA (pre-miRNA) inside the nucleus. The stem-loop is 695
 still preserved, but the two arms become shorter. After that, the pri-miRNA is 696
 transported by Exportin 5 from the nucleus to the cytoplasm. It is further cleaved 697
 by an enzyme called dicer [14]. Dicer cleaves the stem-loop from the two arms 698
 at the two cleavage sites, shown as the two scissors in Figure 3.1. The stem- 699
 loop is removed. It results in a short double-stranded miRNA molecule, known 700

²Its miRBase entry: <https://mirbase.org/hairpin/MI0000060>. (Accessed on: 2025-06-12).

³RNAfold web server: <http://rna.tbi.univie.ac.at/cgi-bin/RNAWebSuite/RFold.cgi>. (Accessed on: 2025-06-12). The figure is viewed in “forna”. This view option can be chosen on the website.

701 as an miRNA duplex, which consists of the 5p strand and the 3p strand⁴. These
702 molecules may be subjected to additional trimming. The miRNA duplex is loaded
703 into an RNA-induced silencing complex (RISC). RISC unwinds the duplex and
704 tends to retain the strand with the less stable 5' end as the guide strand. The
705 other strand is called the passenger strand. The retained strand guides the RISC
706 to silence the target mRNA. Note that both strands can become the guide strand.

707 Dicer plays an important role in the biogenesis of miRNAs. It is reasonable
708 to argue that the structure of the pre-miRNAs informs dicer about the cleavage
709 process. It would be of great benefit to understand how dicer selects cleavage sites
710 from the neighborhood information near the cleavage sites. Studies [15, 16, 17]
711 revealed that the secondary structures are essential for cleavage site determina-
712 tion. Hence, to predict or classify whether a subsequence, extracted from the
713 sequence of a pri-miRNA, contains a cleavage site, we can make use of both the
714 sequence and secondary structure information. PHDcleav employed support vec-
715 tor machines (SVM), leveraging sequence and structure-based features for the
716 classification [18]. LBSIZECLEAV improved upon it by considering the loop and
717 bulge lengths [19]. [20] proposed an ensemble learning approach, using a gradi-
718 ent boosting machine for better accuracy. [21] developed a deep learning model,
719 namely DiCleave. This model used an autoencoder to learn the secondary struc-
720 ture embeddings of pre-miRNAs from all the species in the miRBase database
721 and leveraged this information. All these methods begin with curated pre-miRNA
722 sequences from the miRBase database. Their secondary structures are predicted.
723 Patterns are extracted from the sequence and the secondary structure. They cre-
724 ate the positive cleavage patterns by setting the cleavage sites at the middle of
725 the patterns. The follow-up work of [21], which created the cleavage pattern by
726 allowing cleavage sites to appear at any position within the pattern, instead of
727 the middle only [22]. It created a much larger dataset. This increased dataset
728 facilitates the learning of the deep learning method at the cost of increased run-
729 ning time. We utilized the original dataset setting [18, 19, 20, 21]. DiCleave is the
730 current state-of-the-art (SOTA) for this problem with the original dataset setting.

731 These models suffer several limitations. They rely heavily on complicated
732 feature engineering or opaque deep learning models [20, 21, 22]. It results in a
733 lack of generalizability and a long running time. There is a need to design a
734 simpler model so that it can be easily extended to other prediction tasks on RNA
735 data. One way to analyze sequence data is to transform it into time series data.

⁴The 5p strand comes from the 5' arm while the 3p strand comes from the 3' arm. For the directionality, the 5p (3p) strand retains the original 5' (3') end of the pre-miRNA.

In response to this, we proposed a multivariate time series classification-based method. Our contributions are shown as follows.

1. To the best of our knowledge, we are the first to frame the prediction of the cleavage sites as a multivariate time series classification problem. 738
739
2. We introduced several encoding methods to convert RNA data to time series. 740
3. We proposed utilizing the base-pair probabilities in the predicted secondary structure for the prediction. To our surprise, this information has been ignored in the existing studies. 741
742
743
4. For computational efficiency, our method achieves a 3.7X to 28.8X speedup 744
compared to the state-of-the-art (SOTA). 745
5. We conducted perturbation-based experiments. It shows that regions close 746
to the cleavage sites are important for this problem. It is consistent with the 747
existing study [20]. 748

3.2 Methods

749

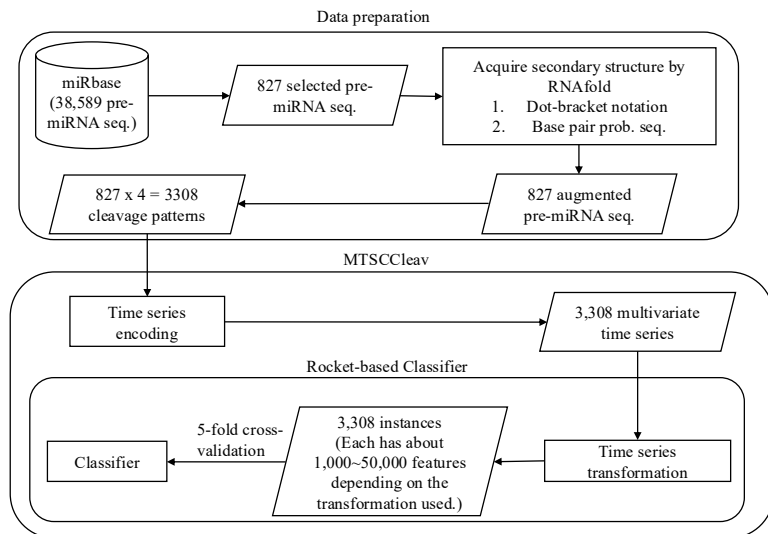


Figure 3.2: The overall pipeline of this study. Symbol notations: Cylinder - Dataset, Rectangle - Process, Parallelogram - Input / Output, Rounded Rectangle - Component.

The overall pipeline of this study is summarized in Figure 3.2.

750

751 **3.2.1 Data Preparation**

Accession	Name	Organism	Sequence	Mature miRNA 1	Mature miRNA 2
MI0000001	cel-let-7	Caenorhabditis elegans	<i>UACAC…UUCGA</i>	cel-let-7-5p 17:38 experimental	cel-let-7-3p 60:81 experimental
MI0000060	hsa-let-7a-1	Homo sapiens	<i>UGGGA…UCCUA</i>	hsa-let-7a-5p 6:27 experimental	hsa-let-7a-3p 57:77 experimental
MI0000114	hsa-mir-107	Homo sapiens	<i>CUCUC…ACAGA</i>	hsa-miR-107 50:72 experimental	NA
MI0000238	hsa-mir-196a-1	Homo sapiens	<i>GUGAA…UUCAC</i>	hsa-miR-196a-5p 7:28 experimental	hsa-miR-196a-1-3p 45:65 not experimental

Table 3.1: Selected representative records from miRBase. For the last two columns, the first line shows the name, the second line shows its location in the original sequence, and the third line indicates whether its existence has experimental evidence. The selected one is highlighted in **bold**.

752 We used miRBase database [23]⁵. The database comprises miRNA data from
753 various organisms [24]. The database contains 38,589 miRNA records. Each record
754 refers to an miRNA sequence, along with other properties such as name, accession,
755 organism, and information on its derivative miRNA products. We are interested in
756 pri-miRNA in humans. The derivative miRNA products are the mature miRNAs.
757 The database also annotates the location of the mature miRNA within the original
758 sequence and indicates whether its existence has experimental evidence.

759 Table 3.1 shows its four representative records. We first selected the records
760 from humans (*Homo sapiens*). It resulted in 1,917 records. To identify the actual
761 locations of the two cleavage sites in the pri-miRNA sequence supported by ex-
762 perimental evidence, we selected records that have two mature miRNAs resulting
763 from cleavage at the 5p arm and the 3p arm, both of which have experimental
764 support. Hence, only “MI0000060” (“hsa-let-7a-1”) would be selected in the table.
765 It would serve as our running example. Its whole sequence is listed in Table 3.2.
766 After the selection process, we selected 827 experimental validated pre-miRNA
767 sequences, each with its two mature miRNA products. This formed our dataset.

768 **Augment the Dataset with Secondary Structure Information**

769 We leveraged the predicted secondary structure of these sequences to enhance the
770 accuracy of the classification. Recall that a specific three-dimensional (3D) struc-
771 ture is required for DNA, RNA, and protein to perform functions [25]. However,

⁵The website is www.mirbase.org, and the newest version of the database is Release 22.1 (Accessed on 2025-06-22).

Sequence	Secondary Structure (In Dot-bracket notation)
1 UGGGA UGAGGUAGUAGGUUGUAUAGUU 27 28 UUAGGGUCACACCCACCACUGGGAGAU 54 55 AA CUAUACAAUCUACUGUCUUCCUA 80	1 ((((((.((((((((((((27 28 UUAGGGUCACACCCACCACUGGGAGAU 54 55))))))))))))))))))))) 80
Base-pair probabilities sequence (the first 10 bases)	
1 (0.549, 0.946, 0.987, 0.987, 0.904) 5 6 (0.000 , 0.841, 0.974, 0.981, 0.890) 10	

Table 3.2: The whole sequence of “hsa-let-7a-1” and its predicted secondary structure by RNAfold. The corresponding positions of the two mature miRNAs and the probability of the unpaired “U” are highlighted in **bold**.

finding these 3D structures using experimental methods such as X-ray crystallography or nuclear magnetic resonance (NMR) is costly and time-consuming. Hence, prediction methods for such 3D structures are necessary and helpful for downstream analysis. However, predicting the 3D structures is challenging. One of the reasons is that there are some “nonconventional” base-pair interactions (e.g., noncanonical and rare A-G) that allow an RNA sequence to fold into a 3D structure, in addition to the (G, U) wobble pair, which is common and functionally important in RNA secondary structures. It makes the search space for prediction much larger than, in the 2D case, the secondary structure. The local structures of the 3D structures, the secondary structures, only focus on the conventional base-pair interactions [12]. Hence, predicting secondary structures is easier and faster. We employed RNAfold from the ViennaRNA Package⁶ to predict the secondary structure for a given pri-miRNA S [26]. RNAfold returns the secondary structure in the dot-bracket notation and a matrix of base-pair probabilities. The matrix is a square matrix with the side length $|S|$, where each entry m_{ij} is the probability of base s_i paired up with base s_j . Dot-bracket notation is a way of representing the secondary structure of S . Open parentheses “(“ (Close parentheses “)”) indicates that the base is paired with a complementary base further (earlier) along in S . Dot “.” indicates that the base is unpaired. Equipped with the matrix, we can construct the base-pair probability sequence of S . The predicted secondary structure and the base-pair probability sequence of our running example are shown in Table 3.2.

Extract Cleavage Patterns

The locations of the two mature miRNAs on the whole sequence indicate the probable locations of the two cleavage sites. The 5p cleavage site must be beyond

⁶The latest stable release is Version 2.7.0 (Accessed on 2025-06-22).

797 and near the ending location of the 5p mature miRNA. We deemed the immediate
 798 bond next to the 5p mature miRNA’s ending position the 5p cleavage site, with
 799 the knowledge that the actual cleavage site may not be this immediate bond but
 800 rather the nearby bonds after it. The same applies to the 3p cleavage site. It
 801 is located at the immediate bond before the starting position of the 3p mature
 802 miRNA.

803 For each arm of each whole sequence, we extracted a 14-string⁷ with the
 804 cleavage site located at the center of the string. The first 7 nt (nucleotide) be-
 805 fore the center are highlighted in **bold**. In our running example, it would be
 806 “**UUAUAGUUUUAGGU**” for the 5p cleavage site and “**GAGAUAA**CUAUACA”
 807 for the 3p cleavage site. We refer to these 14-strings as cleavage patterns. We
 808 also generate non-cleavage patterns by selecting a 14-string with the center 6 nt
 809 away from the corresponding cleavage sites towards the corresponding mature
 810 miRNA [19, 20] for each arm of each whole sequence. So, in our running exam-
 811 ple, the 5p non-cleavage pattern would be “**AGGUUGU**AUAGUUU”. The 3p
 812 non-cleavage pattern would be “**ACUAUAC**AAUCUAC”.

813 In conclusion, for a given pri-miRNA sequence, we can generate two cleavage
 814 patterns and two non-cleavage patterns. We call these four patterns simply the
 815 “four strings” of a given pri-miRNA. We also call each string a strand. The “four
 816 strings” of our running example are listed in Table 3.3.

	5p cleav	5p non-cleav	3p cleav	3p non-cleav
Input strand	UUAUAGUUUUAGGU	AGGUUGU AUAGUUU	GAGAUAA CUAUACA	ACUAUAC AAUCUAC
Complementary strand	AUAUCAA_____UA	UCUAACAUAAUCAA_	C_CUGUUGAUUAUGU	UGAUUAUGUUGGAUG

Table 3.3: The first row shows the “four strings” of “hsa-let-7a-1”. Their comple-
 mentary strands are shown in the second row. As a whole, they are referred to as
 the “eight strings”.

817 We can construct the complementary strand of each of the strands in the “four
 818 strings” by finding the corresponding paired base for each of the bases in the input
 819 strand by considering the secondary structure information. We use “_” to denote
 820 the unpaired base in the complementary strand. For example, in Figure 3.1,
 821 “UUAGG” in the 5p cleavage pattern is unpaired, while other bases pair with
 822 some bases, the resulting complementary strand is “AUAUCAA_____UA”. There
 823 is a loop/budge there. We refer to the “four strings” and the four complementary
 824 strands together as the “eight strings” of the input pre-miRNA. It is also shown
 825 in Table 3.3.

⁷String with length = 14.

3.2.2 Time Series Encoding

826

A *time series* $T = t_1, t_2, \dots, t_n$ is a sequence of real-valued numbers⁸. A short contiguous region of T is called a subsequence. A *subsequence* $T(i : j) = t_i, t_{i+1}, \dots, t_j$ of a time series T is a shorter time series that starts from position i and ends at position j , where $i < j$.

827

828

829

830

Strings and time series are temporal sequences. The difference between strings and time series lies in their behavioral attributes [27]. For strings, an entry is a letter from a predefined set called the *alphabet*. For example, the alphabet is $\{A, C, G, T\}$ in the DNA string, while $\{A, C, G, U\}$ in the RNA string. For time series, an entry is a real number. Unlike real numbers, there is no ordering in the alphabet unless some external domain knowledge is introduced.

831

832

833

834

835

836

The study of applying signal processing techniques to genomic data is called “Genomic Signal Processing” (GSP) [28, 29]. In the field of GSP, the time series representations of DNA strings are referred to as DNA numeric representations (DNR). Many DNRs have been proposed. We noted that DNA strings and RNA strings are equivalent from a computational standpoint. Many transformation methods designed for DNA can be applied to RNA by simply substituting T with U . We present nine encoding methods. The relationship among them is shown in Figure 3.3.

837

838

839

840

841

842

843

844

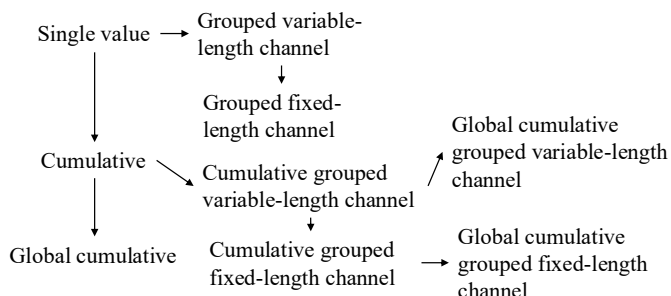


Figure 3.3: Relationship of the proposed encoding methods.

Single Value versus Cumulative

845

One of the simple, if not the simplest, encoding is to map the letters into numbers. Domain knowledge can be utilized. This approach is called the “Single value mapping” [30, 31, 32, 33, 28]. One single value is assigned to each of the letters. [34] employed the atomic number of each nucleotide as the transformed values,

846

847

848

849

⁸Unless otherwise specified, we denote entries of a time series (e.g., T) using the corresponding lowercase letter (e.g., t).

850 where $\{G = 78, A = 70, C = 58, T = 66\}$. [35] used electron-ion interaction po-
851 tential representation (EIIP) as such value, where $\{G = 0.0806, A = 0.1260, C =$
852 $0.1340, T = 0.1335\}$. Our goal is to transform the input strand and its comple-
853 mentary strand into time series, aiming to capture the information contained in
854 these sequences and the secondary structure implied by them. We employed the
855 following reasoning to assign the value:

- 856 1. We employ the complementary property [36, 32] during encoding. Recall
857 that in the base-pairing rules, G pairs with C to form three hydrogen bonds
858 while A pairs with U^9 to form two hydrogen bonds. $G-C$ pairs are more
859 stable than $A-U$ pairs. G (U) can be regarded as the “inverse” of C (A).
860 We can preserve these base-pairing rules in the encoding by assigning G (A)
861 and C (U) opposite values.
- 862 2. G and A have a two-ring structure. They are purines. C and U have a
863 single-ring structure. They are pyrimidines. Hence, we put G and A (C and
864 U) on the same side of the number line with zero in the middle.
- 865 3. The lower stability of $A-U$ pairs promotes strand separation, thereby facili-
866 tating the unwinding of the miRNA duplex during RISC loading. Regions
867 rich in A and U are thus more likely to undergo strand selection and cleavage
868 events. We assigned A (U) with a larger absolute value than G (C) to reflect
869 this functional relevance. It aims to highlight sequence regions with higher
870 cleavage potential.

871 It results in our baseline transformation method, namely “Single value mapping”
872 as shown in row 1 of Table 3.4. S is the input strand. When we encode S without
873 incorporating the corresponding base-pair probability sequence P , we set $p_i =$
874 1 for all the entries of P . We use the first ten nucleotides of the complementary
875 strand of the 3p cleav of “hsa-let-7a-1”, as shown in Table 3.3 as S in the examples
876 in Table 3.4.

877 With the assigned value to each nucleotide defined in single-value mapping, we
878 can compute a cumulative sum of those values over time. It captures the aggre-
879 gated signal by accumulating past events, allowing us to focus on the trend [37, 38].
880 We named this method as “Cumulative mapping”, shown in row 4 of Table 3.4.

⁹In DNA, A pairs with T .

	Encoding	Algorithm	Example
1	Single value mapping [30, 31, 32, 33, 28]	<p>for $i = 1$ to S:</p> $t_i = \begin{cases} 2 \cdot p_i & \text{if } s_i = A \\ 1 \cdot p_i & \text{if } s_i = G \\ -1 \cdot p_i & \text{if } s_i = C \\ -2 \cdot p_i & \text{if } s_i = U \\ 0 & \text{otherwise} \end{cases}$ <p>return T</p>	<p>$S = C, -, C, U, G, U, U, G, A, U$ $P = 0.843, 0.000, 0.807, 0.807, 0.793,$ $0.914, 0.982, 1.000, 0.999, 0.999$</p> <p>Without base-pair probability sequence: $T = -1, 0, -1, -2, 1, -2, -2, 1, 2, -2$</p> <p>With base-pair probability sequence: $T = -0.843, 0.000, -0.807, -1.614,$ $0.793, -1.829, -1.963,$ $1.000, 1.999, -1.998$</p>
2	Grouped variable-length channel mapping	<p>$j = 1, k = 1$</p> <p>for $i = 1$ to S:</p> $t_j^1 = \begin{cases} 1 \cdot p_i & \text{if } s_i = A \\ -1 \cdot p_i & \text{if } s_i = U \\ 0 & \text{otherwise} \end{cases}$ $t_k^2 = \begin{cases} 1 \cdot p_i & \text{if } s_i = G \\ -1 \cdot p_i & \text{if } s_i = C \\ \text{if } (s_i = G) \text{ or } (s_i = C): \\ \quad \text{increment } k \text{ by 1} \\ \text{else:} \\ \quad \text{increment } j \text{ by 1} \end{cases}$ <p>return T^1, T^2</p>	<p>Without base-pair probability sequence: $T^1 = 0, -1, -1, -1, 1, -1$ $T^2 = -1, -1, 1, 1$</p> <p>With base-pair probability sequence: $T^1 = 0.000, -0.807, -0.914, -0.982, 0.999, -0.999$ $T^2 = -0.843, -0.807, 0.793, 1.000$</p>
3	Grouped fixed-length channel mapping	<p>for $i = 1$ to S:</p> $t_i^1 = \begin{cases} 1 \cdot p_i & \text{if } s_i = A \\ -1 \cdot p_i & \text{if } s_i = U \\ 0 & \text{otherwise} \end{cases}$ $t_i^2 = \begin{cases} 1 \cdot p_i & \text{if } s_i = G \\ -1 \cdot p_i & \text{if } s_i = C \\ 0 & \text{otherwise} \end{cases}$ <p>return T^1, T^2</p>	<p>Without base-pair probability sequence: $T^1 = 0, 0, 0, -1, 0, -1, -1, 0, 1, -1$ $T^2 = -1, 0, -1, 0, 1, 0, 0, 1, 0, 0$</p> <p>With base-pair probability sequence: $T^1 = 0.000, 0.000, 0.000, -0.807,$ $0.000, -0.914, -0.982,$ $0.000, 0.999, -0.9999$ $T^2 = -0.843, 0.000, -0.807, 0.000,$ $0.793, 0.000, 0.000,$ $1.000, 0.000, 0.000$</p>
4	Cumulative mapping [37, 38]	<p>$t_1 = 0$</p> <p>for $i = 1$ to S:</p> $t_{i+1} = \begin{cases} t_i + 2 \cdot p_i & \text{if } s_i = A \\ t_i + 1 \cdot p_i & \text{if } s_i = G \\ t_i - 1 \cdot p_i & \text{if } s_i = C \\ t_i - 2 \cdot p_i & \text{if } s_i = U \\ t_i & \text{otherwise} \end{cases}$ <p>return $T // T = S + 1$</p>	<p>Without base-pair probability sequence: $T = 0, -1, -1, -2, -4, -3, -5, -7, -6, -4, -6$</p> <p>With base-pair probability sequence: $T = 0.000, -0.843, -0.843, -1.650,$ $-3.265, -2.471, -4.300, -6.263,$ $-5.264, -3.265, -5.263$</p>
5	Cumulative grouped variable-length channel mapping	<p>$t_1^1 = 0, t_1^2 = 0$</p> <p>$j = 1, k = 1$</p> <p>for $i = 1$ to S:</p> $t_{j+1}^1 = \begin{cases} t_j^1 + 1 \cdot p_i & \text{if } s_i = A \\ t_j^1 - 1 \cdot p_i & \text{if } s_i = U \\ t_j^1 & \text{if } s_i = - \end{cases}$ $t_{k+1}^2 = \begin{cases} t_k^2 + 1 \cdot p_i & \text{if } s_i = G \\ t_k^2 - 1 \cdot p_i & \text{if } s_i = C \\ t_k^2 & \text{if } (s_i = G) \text{ or } (s_i = C): \\ \quad \text{increment } k \text{ by 1} \\ \text{else:} \\ \quad \text{increment } j \text{ by 1} \end{cases}$ <p>return T^1, T^2</p>	<p>Without base-pair probability sequence: $T^1 = 0, -1, -2, -3, -2, -3$ $T^2 = 0, -1, -2, -1, 0$</p> <p>With base-pair probability sequence: $T^1 = 0.000, -0.807, -1.722,$ $-2.703, -1.704, -2.703$ $T^2 = 0.000, -0.843, -1.650,$ $-0.857, 0.143$</p>
6	Cumulative grouped fixed-length channel mapping	<p>$t_1^1 = 0, t_1^2 = 0$</p> <p>for $i = 1$ to S:</p> $t_{i+1}^1 = \begin{cases} t_i^1 + 1 \cdot p_i & \text{if } s_i = A \\ t_i^1 - 1 \cdot p_i & \text{if } s_i = U \\ t_i^1 & \text{otherwise} \end{cases}$ $t_{i+1}^2 = \begin{cases} t_i^2 + 1 \cdot p_i & \text{if } s_i = G \\ t_i^2 - 1 \cdot p_i & \text{if } s_i = C \\ t_i^2 & \text{otherwise} \end{cases}$ <p>return $T^1, T^2 // T^1 = T^2 = S + 1$</p>	<p>Without base-pair probability sequence: $T^1 = 0, 0, 0, -1, -1, -2, -3, -3, -2, -3$ $T^2 = 0, -1, -1, -2, -2, -1, -1, 0, 0, 0$</p> <p>With base-pair probability sequence: $T^1 = 0.000, 0.000, 0.000, 0.000,$ $-0.807, -0.807, -1.722, -2.703,$ $-2.703, -1.704, -2.703$ $T^2 = 0.000, -0.843, -0.843, -1.650,$ $-1.650, -0.857, -0.857, -0.857,$ $0.143, 0.143, 0.143$</p>

Table 3.4: Time series encoding. P is the corresponding base-pair probability sequence of S . $p_i = 1$ if we encode S without incorporating base-pair probability sequence.

881 **Grouped Variable-Length Channel versus Grouped Local-Length Chan-**
882 **nel**

883 We can transform the input strand into a multivariate time series with two chan-
884 nels using grouped binary encoding, where nucleotides are grouped into (A, U)
885 and (G, C). It releases our third assumption that A (U) has a larger absolute value
886 than G (C). We proposed two variations. The first one allows the output to be
887 variable-length sequences per channel, depending on group-specific occurrences.
888 The second one always returns two resulting sequences of a fixed length. Two
889 variations extended from single value mapping are shown in rows 2 and 3, while
890 those extended from cumulative mapping are shown in rows 5 and 6 in Table 3.4.

891 **Global Cumulative versus Local Cumulative**

892 In cumulative mapping and its variations, we can choose where to start the accu-
893 mulation. For a given subsequence S' of the whole sequence S , accumulation can
894 start from the beginning of S even if only S' is used downstream. It can also begin
895 just at the start of the S' . The first one preserves the global context. It can be
896 useful when previous nucleotides (those before S') influence later interpretation.
897 The second one focuses solely on local history in S' , ignoring global history. It is
898 helpful if the previous nucleotides do not affect the chemical property of S' .

899 Consider $T = 0, -1, \dots, -6$ of the input string S in “Cumulative mapping”
900 in Table 3.4, which accumulates from 0. S is the suffix with length = 10 of
901 the constructed complementary strand of $S(1 : 63)$ in Figure 3.1. If we start
902 the accumulation from the first entry of the constructed complementary strand
903 instead, it will yield a different result. Suppose that the last entry of the time series
904 encoded in the cumulative mapping of the constructed complementary strand
905 is -8, the time series encoded in the “Global cumulative mapping” for S would
906 accumulate from -8 instead of 0. The result is $T = -8, -9, \dots, -14$. Note that it
907 has the same trend as the original T . This “Global cumulative” concept can be
908 applied to every cumulative-based method, as shown in Figure 3.3.

909 **Incorporating Base-Pair Probabilities**

910 We can incorporate the base-pair probabilities P in the encoding by thinking of it
911 as the weight or confidence p_i in the value assignment of each nucleotide s_i . It is
912 implemented by multiplying the base-pair probability p_i of the nucleotide s_i with
913 the assigned value of the kind of nucleotide of s_i during encoding, as shown in
914 Table 3.4.

Transforming the Secondary Structure into a Time Series 915

We can transform the secondary structure in the dot-bracket notation into a time series by “Single value mapping”, where “(” maps to 1, “.” maps to 0, and “)” maps to -1. 916
917
918

3.2.3 Time Series Classification 919

In univariate time series classification, an instance in the dataset consists of a time series $x = x_1, x_2, \dots, x_m$ with m observations and a discrete class label y , which takes c possible values [39, 40]. If $c = 2$, we refer to binary classification. If $c > 2$, we refer to multi-class classification. In multivariate time series classification, the time series is not a single sequence but a list of sequences. Each sequence is called a channel. There are many classifiers defined for time series data, including distance-based, feature-based, interval-based, shapelet-based, dictionary-based, convolution-based, and deep learning-based classifiers. Additionally, two or more of the above approaches can be combined, resulting in hybrid approaches [1, 40, 39]. We employed convolution-based classifiers due to their simplicity and accuracy. 920
921
922
923
924
925
926
927
928
929
930

Convolution-Based Classifiers 931

Convolution-based classifiers first use randomly parameterized kernels to perform convolutions on the original time series T . A kernel is referred to as parameterized because its behavior is governed by a set of parameters, which will be discussed in detail later. Convolution is an operation to transform T to another time series M , where M is called the activation map. Its entry M_i is calculated by applying a kernel ω with length l to T at position i , defined as follows: 932
933
934
935
936
937

$$M_i = T(i : i + l - 1) * \omega = \sum_{j=0}^{l-1} t_{i+j} \cdot \omega_{1+j}$$

To note, $|T(i : i + l - 1)| = |\omega| = l$. Entries M_i 's are calculated by sliding ω across T and computing a dot product. Additionally, although the original paper [41] used the term “convolution” to refer to the above operation, “cross-correlation” may be a more suitable term for this operation. Recall T with length m has $(m - l + 1)$ sliding windows of length l , given that the increment is 1^{10} , which defines the length of M . 938
939
940
941
942
943

¹⁰One step to the right per time.

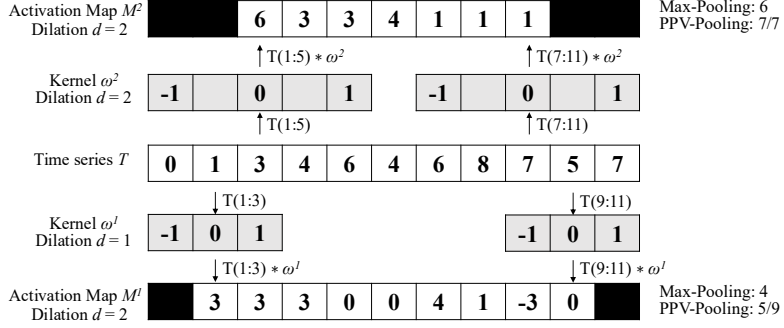


Figure 3.4: Features generation in the transformation

944 Figure 3.4 shows two kernels ω^1 and ω^2 with lengths 3 and 5, respectively. Each
945 of which performs a convolution with T and returns two activation maps, M^1 and
946 M^2 , respectively. For example, $M_1^1 = T(1 : 3) * \omega^1 = 3$. By sliding ω^1 one time
947 stamp at a time, an activation map M^1 with length = $(m-l+1) = 11-3+1 = 9$ is
948 obtained. Then, pooling operations, such as the maximum (MAX) and proportion
949 of positive values (PPV), are applied on M^1 to derive the summary features. In
950 Figure 3.4, MAX and PPV are applied on M^1 and M^2 . The summary features
951 of M^1 are 4 and 5/9, which correspond to MAX and PPV, respectively. Dilation
952 refers to a method that enables a kernel to cover a larger portion by creating empty
953 spaces between entries in the kernel. The dilation d of ω^2 is 2. It introduces a gap
954 of 1 in every two values of ω^2 .

955 The most popular convolution-based approach is the Random Convolutional
956 Kernel Transform (ROCKET) [41]. It generates a large number of randomly
957 parameterized kernels, ranging from thousands to tens of thousands. The kernel's
958 parameters include length, weights (the entries inside the kernel), bias (the value
959 added to the result of the convolution operation), and dilation. Additionally,
960 padding can be applied to T at the start and end, ensuring M has the same
961 length as the input. To note, T , M_1 , and M_2 in Figure 3.4 have different lengths.
962 The summary statistics of the activation map are obtained through two pooling
963 operations: MAX and PPV. Hence, for k kernels, the transformed data has $2k$
964 features. The default value of k is 10,000.

965 There are two extensions of ROCKET. They are MiniROCKET [42] and Mul-
966 tiROCKET [43]. MiniROCKET removes unnecessary operations and many of the
967 random components in the definition of kernels used by ROCKET. It speeds up
968 Rocket by over an order of magnitude with no significant difference in accuracy,
969 making the classifier almost deterministic. For example, the kernel length is fixed,
970 and only two weight values are used. Only PPV is used for the summary statis-

tics. MultiROCKET is extended from MiniROCKET. The main improvement of it is to extract features from first-order differences as defined in Table 3.5 and add three new pooling operations [43]. The three added operations are mean of positive values (MPV), mean of indices of positive values (MIPV) and longest stretch of positive values (LSPV). 971
972
973
974
975

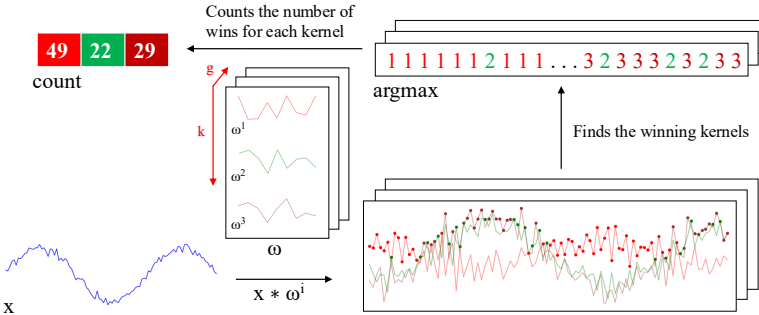


Figure 3.5: Convolutions of HYDRA for each input time series with a set of random kernels w , organized into g groups with k kernels each. 976

The HYbrid Dictionary-ROCKET Architecture (Hydra) combines dictionary-based and convolution-based models [44]. Similar to ROCKET-based classifiers, it uses random kernels to extract features from the input time series. But it groups the kernels into g groups of k kernels each, as shown in Figure 3.5. Each time series is passed through all the groups. For each group of kernels, we slide them across T and compute the dot product at each timestamp. Recall that the dot product of two input vectors (x and w_i) has the maximum value when the two vectors align in the same direction and the minimum value when they are oriented in opposite directions. We record the kernel that best matches the subsequence of T at each timestamp in each group (i.e., $argmax$). We refer to these kernels as the winning kernels. This results in a k -dimensional count vector for each of the g groups, where $k = 3$ in Figure 3.5. This results in a total of $g \times k$ features, with default values of $g = 64$ and $k = 8$. It uses a total of $k \times g = 512$ kernels per dilation. In addition to recording the kernel with the maximum response, we can also record the kernel with the minimum response, knowing that this kernel will be the best match with the “inverted” subsequence of T . Hydra is applied to both the original time series and its first-order differences. Hydra generated approximately 1000 features for each instance in our dataset. [44] found that it can improve the accuracy by concatenating features generated from Hydra with those from MultiRocket. This classifier is called MultiROCKET-Hydra. 976
977
978
979
980
981
982
983
984
985
986
987
988
989
990
991
992
993
994
995

These five classifiers share the same simple design pattern. It involves the over-production of features followed by a selection strategy. A large number of features 996
997

998 (1,000 ~ 50,000) are generated for each instance. The features are then fed into a
 999 simple linear classifier. It determines which features are most useful and returns
 1000 the final classification result. A ridge classifier is used in this study. It is a linear
 1001 classifier that extends ridge regression to classification tasks by applying a thresh-
 1002 old to the predicted values. It uses L2 regularization to prevent overfitting. The
 1003 regularization strength is selected by internal cross-validation. A Ridge classifier
 1004 is suggested for small datasets, as in our case, while a logistic regression classifier
 1005 is suggested for large datasets [1].

1006 While these five classifiers are often referred to as classifiers [1], they are tech-
 1007 nically time series transformation methods for generating features that are then
 1008 fed to a downstream classifier. The comparison of them is shown in Table 3.5. For
 1009 MiniROCKET and MultiROCKET, the bias is determined from the convolution
 1010 output, and the dilation depends on the length of the input time series [42, 43].
 1011 The main differences among ROCKET-based classifiers lie in how the summary
 1012 features are generated. The generation of the summary features depends on:

- 1013 1. Kernels, which are defined based on the parameters, which consist of kernel
 1014 length, kernel weights, bias, and dilation.
- 1015 2. The way that padding applies to T , which leads to activation maps with
 1016 different lengths.
- 1017 3. The pooling operations, which are used in extracting features on the activa-
 1018 tion map.

	ROCKET	MiniROCKET	MultiROCKET	Hydra
kernel length	{7, 9, 11}	9	9	9
kernel weights	$\mathcal{N}(0, 1)$	{-1, 2}	{-1, 2}	$\mathcal{N}(0, 1)$
bias	$\mathcal{U}(0, 1)$	from output	from output	none
dilation	random	fixed (input-relative)	fixed (input-relative)	random
padding	random	fixed	fixed	always
pooling operations	MAX, PPV	PPV	PPV, MPV, MIPV, LSPV	Response per Kernel/Group
1 st order difference	no	no	yes	yes
feature vector size	20k	10k	50k	relative to input

Table 3.5: Comparison of rocket-based classifiers [1]. $\mathcal{N}(0, 1)$: a standard normal distribution, $\mathcal{U}(0, 1)$: a uniform distribution between 0 and 1, 1st order difference: $\Delta T = t_2 - t_1, t_3 - t_2, \dots, t_n - t_{n-1}$.

1019 3.2.4 Evaluation Metrics

1020 To evaluate the performance of our time series-based classification (MTSC) model,
 1021 we adopted five standard classification metrics. They are Accuracy (Acc), Speci-

ficity (Sp), Sensitivity (Sn), F1 score (F1), and Matthews Correlation Coefficient (MCC) [45].

$$Acc = \frac{TP + TN}{TP + TN + FP + FN}$$

$$Sp = \frac{TN}{TN + FP}$$

$$Sn = \frac{TP}{TP + FN}$$

$$F1 = \frac{2 \times TP}{2 \times TP + FP + FN}$$

$$MCC = \frac{TP \times TN - FP \times FN}{\sqrt{(TP + FP)(TP + FN)(TN + FP)(TN + FN)}}$$

where TP, TN, FP, and FN are the number of true positives, true negatives, false positives, and false negatives, respectively.

To extend a binary metric to multi-class problems, we can treat the data as a collection of binary problems, one for each class. One class is treated as positive while the other classes are treated as negative. Then, the multi-class metrics can be obtained by averaging binary metric calculations across the set of classes. There are different ways of doing the averaging. Here, we adopted a macro-averaging approach. It treats each class equally and calculates the mean of the binary metrics. To use MCC in the multiclass case, it can be defined in terms of a confusion matrix C for K classes, where $C_{i,j}$ is the number of observations that are actually in class i and predicted to be in class j [46].

$$MCC_{multi} = \frac{c \times s - \sum_k^K p_k \times t_k}{\sqrt{(s^2 - \sum_k^K p_k^2) \times (s^2 - \sum_k^K t_k^2)}}$$

where $t_k = \sum_i^K C_{i,k}$ (denoting the number of times class k actually occurred), $p_k = \sum_i^K C_{k,i}$ (denoting the number of times class k was predicted), $c = \sum_k^K C_{k,k}$ (denoting the total number of samples correctly predicted) and $s = \sum_i^K \sum_j^K C_{i,j}$ (denoting the total number of samples).

3.3 Results

The code implementing our method is available at <https://github.com/colemanyu/time-series-classification-cleavage>. The dataset of this study is available at <https://www.mirbase.org>.

1043 In all experiments, the models were trained and tested using 5-fold cross-
1044 validation. We retrieved 827 empirically validated sequences of pre-miRNAs.
1045 There are 5p arm and 3p arm in each sequence. For each arm, we defined a
1046 cleavage pattern and a non-cleavage pattern. Three datasets, namely “5p arm”,
1047 “3p arm”, and “multi-class” were constructed by these patterns. We refer to the
1048 cleavage patterns as positive instances and the non-cleavage patterns as negative
1049 instances. The 5p arm dataset comprises 827 positive instances and an equal
1050 number of negative instances. The 5p arm and 3p arm datasets are binary-class
1051 datasets. The multi-class dataset comprises all patterns from both the 5p arm
1052 and the 3p arm. There are 827 “5p” instances¹¹, 827 “3p” instances, and 1,654
1053 negative instances.

1054 For every fold in 5-fold cross-validation, the dataset was divided into a training
1055 set and a test set with sizes of 80% and 20% of the whole dataset, respectively.
1056 We kept the class distribution approximately the same in each fold, since it is in
1057 the original dataset. In each fold derived from the 5p arm and 3p arm datasets,
1058 the training set has a size of 1,323, and the test set has a size of 331. In each
1059 fold derived from the multi-class dataset, the training set has a size of 2,262, and
1060 the test set has a size of 662. We reported the average of the five classification
1061 metrics.

1062 The ROCKET-based classifiers require all channels in the multivariate time
1063 series to have equal length. We applied padding to the shorter channels using the
1064 constant value 100, which does not appear in the original time series. It ensures
1065 the padding does not introduce ambiguity or interfere with the semantic meaning
1066 of the encoded nucleotide signals.

1067 3.3.1 Channel Ablation Study

1068 We utilized three types of data as the input features for each instance. They
1069 are (1) the RNA sequence, which consists of the primary strand and its comple-
1070 mentary strand, (2) the secondary structure information, and (3) the base-pair
1071 probability sequence. To input the data into our time series-based classifiers, we
1072 converted them into multivariate time series. The primary strand and its com-
1073 plementary strand are each encoded into one or two channels, using the encoding
1074 methods in Table 3.4. For example, single value mapping encodes a strand in
1075 one channel, while grouped variable-length channel mapping encodes in two chan-
1076 nels. The secondary structure information is converted into a univariate time

¹¹Cleavage patterns from the 5p arm.

series. The base-pair probability sequence is already in numerical form and does 1077
 not require further transformation. It can be used either as a standalone channel 1078
 or incorporated into the encoding of the complementary strand. We performed 1079
 a channel ablation study to determine the most informative combination of the 1080
 above channels. 1081

We referred to the multivariate time series that consists of the channels from 1082
 the RNA sequence only as the baseline setting. We added the other channels to 1083
 this baseline. It leads to the following configurations (cfgs): 1084

1. (cfg 1) Baseline: Time series derived only from the RNA sequence. 1085
2. (cfg 2) Baseline + Secondary structure: Baseline + time series representation 1086
 of the secondary structure. 1087
3. (cfg 3) Baseline + Base-pair probability (Standalone): Baseline + the base- 1088
 pair probability sequence as a standalone channel. 1089
4. (cfg 4) Baseline + Base-Pair probability (Incorporated): Baseline with the 1090
 base-pair probability sequence incorporated into the encoding of the com- 1091
 plementary strand. 1092

Classifier	5p arm					3p arm					multi-class					
	Acc	Sp	Sn	F1	MCC	Acc	Sp	Sn	F1	MCC	Acc	Sp	Sn	F1	MCC	
Baseline (cfg 1)	ROCKET	0.781	0.743	0.819	0.789	0.563	0.790	0.773	0.807	0.793	0.580	0.717	0.838	0.685	0.700	0.538
	MiniROCKET	0.755	0.728	0.782	0.762	0.512	0.788	0.781	0.794	0.789	0.576	0.685	0.823	0.653	0.662	0.486
	MultiROCKET	0.784	0.767	0.801	0.787	0.569	0.803	0.792	0.814	0.805	0.606	0.691	0.830	0.667	0.672	0.501
	Hydra	0.830	0.800	0.860	0.835	0.663	0.808	0.797	0.820	0.810	0.617	0.731	0.844	0.696	0.712	0.560
	MultiROCKET-Hydra	0.796	0.778	0.815	0.800	0.594	0.807	0.767	0.816	0.808	0.614	0.701	0.836	0.681	0.686	0.520
Baseline + Secondary Structure (cfg 2)	ROCKET	0.847	0.832	0.862	0.849	0.695	0.855	0.842	0.868	0.857	0.711	0.836	0.907	0.828	0.833	0.736
	MiniROCKET	0.825	0.807	0.843	0.827	0.652	0.822	0.802	0.843	0.826	0.646	0.823	0.900	0.812	0.818	0.715
	MultiROCKET	0.812	0.803	0.822	0.814	0.626	0.824	0.809	0.839	0.826	0.649	0.796	0.888	0.791	0.792	0.673
	Hydra	0.845	0.816	0.873	0.849	0.691	0.846	0.817	0.874	0.850	0.693	0.830	0.901	0.814	0.826	0.724
	MultiROCKET-Hydra	0.817	0.809	0.826	0.819	0.635	0.825	0.816	0.834	0.826	0.652	0.803	0.891	0.798	0.800	0.684
Baseline + Base-pair probability (Standalone) (cfg 3)	ROCKET	0.842	0.828	0.855	0.844	0.684	0.855	0.856	0.854	0.855	0.710	0.795	0.885	0.783	0.789	0.670
	MiniROCKET	0.817	0.820	0.814	0.816	0.634	0.836	0.834	0.838	0.836	0.673	0.772	0.872	0.757	0.764	0.632
	MultiROCKET	0.822	0.813	0.832	0.824	0.645	0.825	0.831	0.820	0.824	0.651	0.758	0.866	0.747	0.750	0.612
	Hydra	0.846	0.827	0.865	0.849	0.693	0.851	0.840	0.861	0.852	0.702	0.789	0.879	0.769	0.780	0.658
	MultiROCKET-Hydra	0.822	0.809	0.834	0.824	0.644	0.835	0.840	0.830	0.834	0.670	0.759	0.866	0.746	0.750	0.611
Baseline + Base-pair probability (Incorporated) (cfg 4)	ROCKET	0.799	0.771	0.827	0.805	0.600	0.809	0.786	0.832	0.813	0.619	0.737	0.850	0.712	0.724	0.573
	MiniROCKET	0.776	0.756	0.797	0.781	0.554	0.801	0.808	0.794	0.799	0.603	0.705	0.835	0.675	0.684	0.521
	MultiROCKET	0.814	0.801	0.828	0.817	0.630	0.816	0.812	0.820	0.816	0.634	0.726	0.848	0.706	0.712	0.556
	Hydra	0.822	0.787	0.857	0.828	0.647	0.834	0.828	0.840	0.835	0.669	0.759	0.862	0.734	0.746	0.608
	MultiROCKET-Hydra	0.814	0.802	0.820	0.817	0.629	0.820	0.825	0.816	0.819	0.642	0.736	0.853	0.717	0.723	0.874

Table 3.6: Channel ablation study. The best results are highlighted in **bold**.

We used single value mapping as the encoding method. Table 3.6 shows the 1093
 result. From the table, we can see that the addition of secondary structure, base- 1094
 pair probability as a standalone channel, and base-pair probability incorporated 1095
 in the encoding of the complementary strand can improve the performance. We 1096
 plotted the critical difference (CD) diagram as shown in Figure 3.6 to visualize 1097
 Table 3.6 to make the performances of different combinations more obvious. In 1098

1099 CD diagrams, lower-ranked methods (toward the right) are better. A horizontal
1100 bar connecting combinations indicates no statistically significant difference.

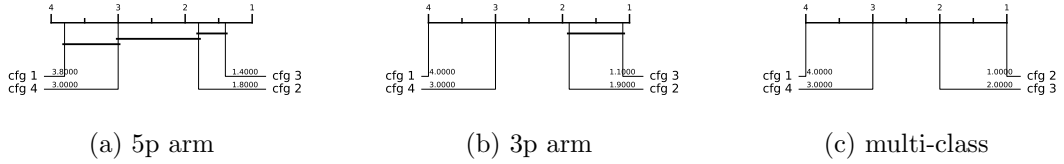


Figure 3.6: CD diagrams of channel ablation study.

1101 From Figure 3.6, we can see that including time series derived from secondary
1102 structure information and base-pair probability as a separate channel can signif-
1103 icantly improve the performance of the classifiers. Incorporating the base-pair
1104 probability sequence in the time series encoding of the complementary strand can
1105 also improve the classifier, but to a minor degree compared to serving as a stan-
1106 dalone channel. In our downstream analysis, we adopted the combination of RNA
1107 sequence time series, secondary structure time series, and base-pair probability
1108 time series as our multivariate time series input, with 4 to 6 channels, depending
1109 on the encoding used.

1110 3.3.2 Predictive Performance

1111 The experiment was conducted on three datasets: the 5p arm, the 3p arm, and
1112 the multi-class datasets. Recall that we have nine encoding methods and five
1113 ROCKET-based classifiers. It results in 45 combinations of encoding methods
1114 and classifiers.

1115 The result is shown in Table 3.7. The best combination of encoding method
1116 and classifier is shown in Table 3.8. For the 5p arm dataset, the best combination
1117 is “Global Cumulative grouped fixed-length channel mapping + ROCKET”. For
1118 all five classification metrics, it outperforms the state-of-the-art (SOTA) method,
1119 DiCleave. For the 3p arm dataset, the best combination is “Global Cumulative
1120 grouped fixed-length channel mapping + ROCKET”. Out of the five classification
1121 metrics, it outperforms DiCleave, except in specificity. For the multi-class dataset,
1122 the best combination is “Global Cumulative grouped fixed-length channel mapping
1123 + ROCKET”. For all five classification metrics, it outperforms DiCleave. Note
1124 that for the 3p arm and the multi-class datasets, the combination of “Cumulative
1125 grouped fixed-length channel mapping + ROKCET” also attains the best result.

1126 To summarize Table 3.7, we plot the CD diagrams for finding the best classifier,
1127 as shown in Figure 3.7, and the best encoding method, as shown in Figure 3.8.

	Classifier	5p arm					3p arm					multi-class				
		Acc	Sp	Sn	F1	MCC	Acc	Sp	Sn	F1	MCC	Acc	Sp	Sn	F1	MCC
Single value mapping (enc 1)	ROCKET	0.849	0.842	0.857	0.851	0.699	0.863	0.854	0.873	0.865	0.727	0.853	0.917	0.847	0.851	0.764
	MiniROCKET	0.823	0.809	0.837	0.825	0.647	0.823	0.828	0.817	0.822	0.647	0.835	0.906	0.828	0.833	0.735
	MultiROCKET	0.821	0.802	0.840	0.824	0.643	0.839	0.826	0.852	0.841	0.679	0.811	0.894	0.806	0.809	0.697
	Hydra	0.843	0.820	0.867	0.847	0.688	0.838	0.819	0.857	0.841	0.677	0.831	0.901	0.815	0.827	0.727
	MultiROCKET-Hydra	0.820	0.803	0.837	0.823	0.640	0.840	0.830	0.850	0.841	0.680	0.816	0.896	0.810	0.814	0.704
Grouped variable-length channel mapping (enc 2)	ROCKET	0.835	0.826	0.844	0.836	0.670	0.855	0.849	0.861	0.856	0.710	0.846	0.913	0.839	0.844	0.752
	MiniROCKET	0.843	0.833	0.853	0.844	0.686	0.831	0.821	0.842	0.833	0.663	0.837	0.907	0.828	0.834	0.737
	MultiROCKET	0.819	0.809	0.828	0.820	0.638	0.817	0.814	0.820	0.818	0.634	0.890	0.894	0.806	0.808	0.695
	Hydra	0.825	0.780	0.869	0.832	0.653	0.811	0.769	0.854	0.819	0.626	0.818	0.892	0.765	0.812	0.705
	MultiROCKET-Hydra	0.818	0.814	0.822	0.819	0.636	0.831	0.825	0.837	0.832	0.662	0.820	0.900	0.815	0.818	0.710
Grouped fixed-length channel mapping (enc 3)	ROCKET	0.851	0.843	0.859	0.852	0.702	0.863	0.850	0.875	0.864	0.726	0.849	0.915	0.843	0.847	0.757
	MiniROCKET	0.844	0.836	0.853	0.845	0.689	0.840	0.826	0.855	0.843	0.682	0.851	0.915	0.844	0.849	0.760
	MultiROCKET	0.831	0.815	0.848	0.834	0.663	0.824	0.813	0.836	0.826	0.649	0.811	0.896	0.808	0.808	0.698
	Hydra	0.848	0.816	0.880	0.853	0.699	0.862	0.829	0.884	0.864	0.724	0.843	0.908	0.837	0.839	0.746
	MultiROCKET-Hydra	0.836	0.813	0.859	0.839	0.672	0.833	0.820	0.845	0.835	0.665	0.828	0.905	0.824	0.826	0.725
Cumulative mapping (enc 4)	ROCKET	0.850	0.834	0.866	0.852	0.701	0.863	0.855	0.871	0.864	0.726	0.852	0.915	0.842	0.850	0.762
	MiniROCKET	0.840	0.821	0.860	0.843	0.682	0.840	0.837	0.844	0.841	0.682	0.843	0.911	0.835	0.840	0.747
	MultiROCKET	0.822	0.809	0.834	0.824	0.644	0.832	0.830	0.834	0.832	0.665	0.820	0.898	0.810	0.816	0.709
	Hydra	0.848	0.819	0.878	0.853	0.698	0.853	0.856	0.869	0.855	0.705	0.845	0.910	0.830	0.841	0.749
	MultiROCKET-Hydra	0.824	0.811	0.856	0.825	0.647	0.838	0.833	0.843	0.839	0.677	0.821	0.898	0.810	0.817	0.711
Cumulative grouped variable-length channel mapping (enc 5)	ROCKET	0.843	0.821	0.866	0.847	0.688	0.856	0.840	0.871	0.857	0.712	0.855	0.916	0.843	0.851	0.766
	MiniROCKET	0.845	0.826	0.865	0.848	0.691	0.836	0.833	0.838	0.836	0.672	0.840	0.909	0.833	0.838	0.742
	MultiROCKET	0.826	0.814	0.838	0.828	0.653	0.815	0.820	0.810	0.814	0.631	0.826	0.902	0.820	0.824	0.721
	Hydra	0.850	0.819	0.880	0.854	0.701	0.834	0.807	0.861	0.838	0.669	0.833	0.903	0.818	0.829	0.731
	MultiROCKET-Hydra	0.824	0.810	0.838	0.826	0.649	0.833	0.833	0.833	0.833	0.666	0.830	0.903	0.821	0.827	0.726
Cumulative grouped fixed-length channel mapping (enc 6)	ROCKET	0.856	0.836	0.876	0.858	0.712	0.870	0.861	0.879	0.871	0.741	0.863	0.921	0.852	0.860	0.780
	MiniROCKET	0.856	0.837	0.874	0.858	0.712	0.842	0.839	0.845	0.843	0.685	0.845	0.912	0.837	0.843	0.751
	MultiROCKET	0.820	0.802	0.839	0.824	0.642	0.798	0.798	0.798	0.798	0.597	0.809	0.894	0.806	0.807	0.694
	Hydra	0.850	0.814	0.885	0.855	0.701	0.855	0.840	0.869	0.857	0.711	0.847	0.910	0.831	0.843	0.752
	MultiROCKET-Hydra	0.820	0.801	0.839	0.823	0.641	0.807	0.813	0.802	0.806	0.615	0.821	0.900	0.817	0.819	0.713
Global Cumulative mapping (enc 7)	ROCKET	0.850	0.834	0.866	0.852	0.701	0.863	0.855	0.871	0.864	0.726	0.852	0.915	0.842	0.850	0.762
	MiniROCKET	0.847	0.832	0.862	0.849	0.695	0.848	0.839	0.857	0.850	0.697	0.845	0.911	0.836	0.843	0.750
	MultiROCKET	0.827	0.819	0.834	0.828	0.653	0.847	0.842	0.853	0.848	0.695	0.825	0.901	0.817	0.822	0.718
	Hydra	0.851	0.821	0.880	0.855	0.703	0.861	0.848	0.874	0.863	0.722	0.847	0.911	0.834	0.844	0.753
	MultiROCKET-Hydra	0.829	0.823	0.834	0.830	0.658	0.843	0.838	0.849	0.844	0.688	0.832	0.905	0.823	0.829	0.730
Global Cumulative grouped variable-length channel mapping (enc 8)	ROCKET	0.840	0.814	0.867	0.844	0.682	0.853	0.838	0.867	0.854	0.706	0.856	0.917	0.845	0.853	0.768
	MiniROCKET	0.848	0.834	0.862	0.850	0.697	0.841	0.824	0.859	0.844	0.683	0.844	0.911	0.856	0.842	0.748
	MultiROCKET	0.834	0.826	0.839	0.834	0.668	0.831	0.821	0.842	0.833	0.663	0.828	0.904	0.823	0.826	0.724
	Hydra	0.857	0.821	0.894	0.862	0.717	0.822	0.786	0.857	0.828	0.645	0.826	0.898	0.806	0.820	0.717
	MultiROCKET-Hydra	0.837	0.834	0.839	0.837	0.674	0.834	0.827	0.840	0.835	0.668	0.835	0.907	0.828	0.832	0.734
Global Cumulative grouped fixed-length channel mapping (enc 9)	ROCKET	0.856	0.836	0.876	0.858	0.712	0.870	0.861	0.879	0.871	0.741	0.863	0.921	0.852	0.860	0.780
	MiniROCKET	0.857	0.845	0.870	0.859	0.715	0.840	0.821	0.859	0.843	0.681	0.844	0.911	0.837	0.842	0.749
	MultiROCKET	0.829	0.825	0.833	0.830	0.658	0.820	0.816	0.823	0.820	0.640	0.819	0.900	0.816	0.817	0.710
	Hydra	0.856	0.817	0.894	0.861	0.713	0.859	0.838	0.880	0.862	0.719	0.846	0.911	0.832	0.843	0.752
	MultiROCKET-Hydra	0.829	0.824	0.834	0.830	0.658	0.822	0.825	0.819	0.821	0.644	0.827	0.904	0.823	0.824	0.722

Table 3.7: Performance on the 45 combinations between encoding methods and the ROCKET-based classifiers. The best results are highlighted in **bold**.

Dataset	Methods	Acc	Sp	Sn	F1	MCC	Time (s)
5p arm	enc 9 + MiniROCKET	0.857	0.845	0.870	0.859	0.715	0.787
	DiCleave	0.818	0.790	0.846	0.822	0.653	21.249
3p arm	enc 9 + ROCKET	0.870	0.861	0.879	0.871	0.741	4.311
	enc 7 + MiniROCKET	0.848	0.839	0.857	0.850	0.697	0.989
	DiCleave	0.854	0.891	0.817	0.847	0.715	15.919
multi-class	enc 9 + ROCKET	0.863	0.921	0.852	0.860	0.780	12.208
	enc 3 + MiniROCKET	0.851	0.915	0.844	0.849	0.760	4.550
	DiCleave	0.820	0.895	0.804	0.815	0.710	131.151

Table 3.8: Comparative analysis between MTSCCleav with the best combination of the encoding method and classifier, with the SOTA, DiCleave, on the three datasets. The best results of using MiniROCKET have also been shown to compare the computational efficiency. The best results are highlighted in **bold**.

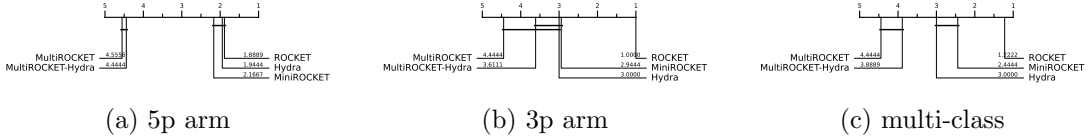


Figure 3.7: CD diagrams to compare different classifiers.

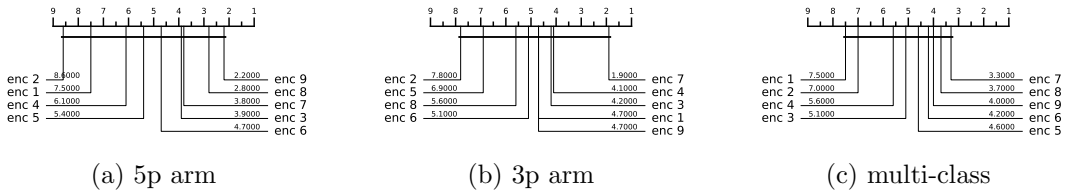


Figure 3.8: CD diagrams to compare different encoding methods.

1128 3.3.3 Running Time Analysis

1129 To compare the computational efficiency of MTSCCleav and DiCleave, we con-
 1130 ducted a comparative analysis of their running times. For DiCleave, we employed
 1131 the code from its supporting website¹², without any modifications. All exper-
 1132 iments were conducted on the same machine (a personal laptop equipped with
 1133 an Apple M1 Pro chip and 16 GB of memory) and using the same splits of the
 1134 training and test datasets under 5-fold cross-validation to ensure fairness. The
 1135 reported running times are the averages of the five runs. The timing results were
 1136 measured from the training phase to the return of the five classification metrics.
 1137 The result is shown in Table 3.8. MiniROCKET is the most computationally ef-
 1138 ficient of the five rocket-based classifiers. We also included its best result, along
 1139 with the corresponding encoding method, even though this combination may not
 1140 be the best overall.

1141 MTSCCleav demonstrated a significant advantage in computational efficiency,
 1142 achieving an average 27.0X, 3.7X, and 10.7X speedup over DiCleave, for the 5p
 1143 arm, 3p arm, and multi-class datasets, respectively. If we consider using the
 1144 MiniROCKET in the case of 3p arm and multi-class datasets, it achieves 16.1X
 1145 and 28.8X speedup. To note, in the case of the 3p arm dataset, the performance of
 1146 MiniROCKET is only slightly worse than DiCleave. In the case of the multi-class
 1147 dataset, even the performance of MiniROCKET is better than DiCleave. DiCleave
 1148 is a deep learning-based method that requires substantial time for model inference,
 1149 while MTSCCleav leverages efficient ROCKET-based classifiers. This significant

¹²

<https://github.com/MGuard0303/DiCleave> (Accessed on: 2025-07-13).

reduction in runtime makes MTSCCleav more suitable for large-scale data and 1150
real-time applications. 1151

3.3.4 Subsequence Importance 1152

To evaluate the sensitivity of MTSCCleav to subsequences of the input, we conducted a perturbation experiment to evaluate the importance of subsequences 1153 based on masking windows. The goal of this experiment is to identify which subsequences 1154 of the entire time series are critical for classification. We examine how 1155 various modifications to the original input impact model performance. It suggests 1156 which features are essential for classification. 1157

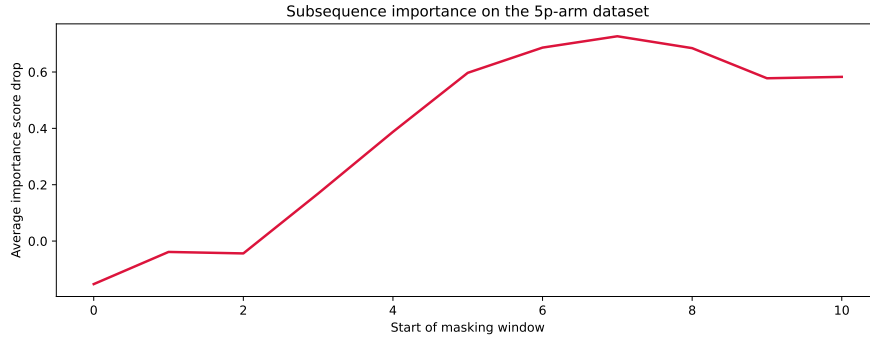
The model was trained on the original training dataset. For each instance in 1159 the test dataset, we measure its original score and the masked score. We slid 1160 a masking window w with a fixed length over the input time series T . $|w|$ was 1161 set to 4. For each window position $i \in \{1, 2, \dots, |T| - |w| + 1\}$, we masked all 1162 entries across all the channels of T within the window. Hence, we removed or 1163 hid that portion of information from the model during inference. The changes in 1164 classification performance in terms of accuracy relative to the unmasked original 1165 score of each i are recorded. Intuitively, if the information of a subsequence is 1166 critical for the classification, the masking of this subsequence would lead to a 1167 great drop in classification performance. We aggregated the importance score 1168 across the test dataset. 1169

The result is shown in Figure 3.9. For the encoding methods, we cannot 1170 use the methods derived from the cumulative mapping because the accumulation 1171 would leak information from the masked region. We adopted “Grouped fixed- 1172 length channel mapping” as the encoding method and ROCKET as the classifier. 1173 “Grouped fixed-length channel mapping” is the best encoding, other than the 1174 methods derived from the cumulative mapping, in all datasets, as shown in Fig- 1175 ure 3.8. ROCKET is the best classifier, as shown in Figure 3.7.. 1176

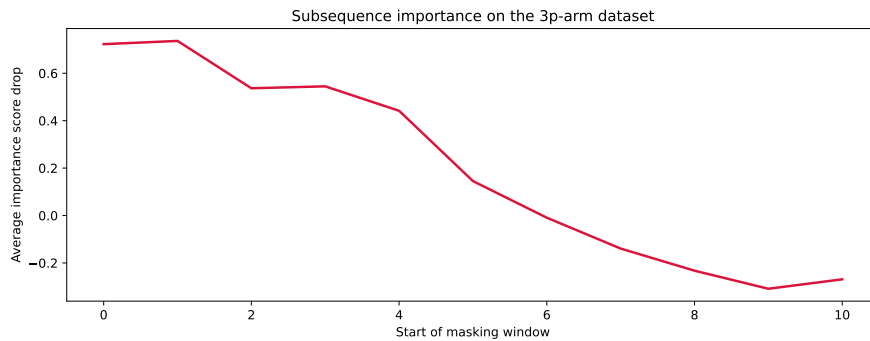
In the 5p arm dataset, we found that masking subsequences at the tailing part 1177 caused a significant drop in the importance score, as shown in Figure 3.9 (a). 1178 In the 3p arm dataset, we found that masking subsequences at the leading part 1179 caused a significant drop in the importance score, as shown in Figure 3.9 (b). 1180

3.3.5 Summary 1181

Our method achieves better or comparable predictive results and a 3.7X to 28.8X 1182 speedup compared to the state-of-the-art (SOTA). 1183



(a) 5p arm



(b) 3p arm

Figure 3.9: Results of the perturbation experiment.

1184 3.4 Discussion

1185 The channel ablation study reveals that the involvement of the time series derived
 1186 from the secondary structure can improve accuracy. It suggests the importance
 1187 of RNA folding in dicer processing. Furthermore, we found that the base-pair
 1188 probability sequence of the secondary structure can also enhance accuracy. To
 1189 the best of our knowledge, it is a novel application of the base-pair probability
 1190 sequence. Experiments show that using the probability sequence as an additional
 1191 channel can enhance accuracy more than incorporating it in the encoding. It is
 1192 likely because keeping it as an additional channel can preserve more information,
 1193 of both the probability sequence itself and the complementary strand.

1194 Out of the three datasets, the best classifier is ROCKET. The ranking of the
 1195 five classifiers by performance, starting from the best, is as follows: ROCKET, Hy-
 1196 dra, MiniROCKET, MultiROCKET-Hydra, and MultiROCKET. It indicates that
 1197 the features created from the pooling operations that are only in MultiROCKET
 1198 but not in MiniROCKET, confuse the final classifier. They are mean of positive
 1199 values (MPV), mean of indices of positive values (MIPV) and longest stretch of

positive values (LSPV) [43]. In contrast, the pooling operator that is only present in ROCKET but not in MiniROCKET, enhances the classification performance. It is maximum (MAX).

For the encoding methods, we have the following observations. Fixed-length grouped channel mappings outperform variable-length counterparts with one exception in the multi-class dataset, likely because fixed-length schemes better preserve the original positional information of nucleotides within the sequence. Global cumulative methods consistently yield better performance than local cumulative methods. It suggests that the upstream information of the cleavage pattern plays a critical role in identifying cleavage sites. Cumulative-based encodings perform better than single-value mappings, with one exception in the 3p dataset, suggesting that the accumulated nucleotide signal is more informative for cleavage site prediction than the local or isolated presence of nucleotides. In the 5p arm dataset, encoding RNA sequence in two channels appears to worsen the result. This suggests that the 5p arm dataset and the 3p arm dataset need different nucleotide grouping methods for the encoding.

One limitation of DiCleave is overfitting during training because of the relatively small size of the dataset [21]. DiCleave is a deep learning-based method. Deep learning models typically require a large amount of training data to generalize effectively. They are data-hungry. In contrast, MTSCCleav leverages ROCKET-based methods for the classification. They rely on random convolutional feature extraction followed by a simple linear classifier. The Ridge classifier used in this study is less data-hungry compared to deep learning methods due to its use of L2 regularization and the simplicity of its linear model nature. It allows ROCKET-based classifiers, and hence MTSCCleav, to maintain strong predictive performance even in settings with a relatively small dataset size.

The subsequence importance reveals some connections between RNA secondary structure and human dicer cleavage site prediction. The perturbation experiment shows that the leading part of 5p arm and the tailing part of 3p arm are important for the classification. These parts are close to the center of the RNA secondary structure of pre-miRNA. It indicates that the center region is more crucial for human dicer cleavage site prediction. It is consistent with the previous study [20].

3.5 Concluding Remarks

We proposed an accurate, fast, and simple multivariate time series classification (MTSC)-based method, termed MTSCCleav, for predicting human dicer cleavage

1235 sites. Base-pair probability sequences of the secondary structures have also been
1236 leveraged in the classification. MTSCCleav consists of three parts: time series en-
1237 coding, time series transformation, and classification. ROCKET-based methods
1238 were used for time series transformation. Ridge Classifier was used for classifica-
1239 tion. For the computational experiments, we evaluated nine time series encoding
1240 methods in conjunction with five time series transformation methods. MTSCCleav
1241 outperformed the SOTA method in all five evaluation metrics for the 5p-arm and
1242 multi-class datasets, and four of the metrics for the 3p-arm dataset. In terms of
1243 computational efficiency, MTSCCleav with the optimal setting achieved an aver-
1244 age 3.7X to 27.0X speedup over the SOTA method on the three datasets. With
1245 the use of a less accurate but faster time series classification method, MTSCCleav
1246 achieved an average speedup of 16.1X to 28.8X, respectively. We analyzed the
1247 subsequence importance of the input multivariate time series. The results show
1248 that subsequences near the center of the pre-miRNA sequences are more impor-
1249 tant. This aligns with the findings from previous work. This study demonstrates
1250 that time series analysis provides a powerful alternative to conventional modeling
1251 in the context of RNA processing. This framework may be extended to other
1252 RNA-processing tasks. Notably, the encoding of RNA sequence into time series
1253 enables us to utilize any well-established tools from the time series community.

Chapter 4

1254

Scaling with Multiple Scaling

1255

Factors in Time Series Searching

1256

Time series data are ubiquitous across many different fields. Many data mining 1257 tasks, such as classification, clustering, and motif finding, have been defined for 1258 time series data. They utilize similarity search as a core subroutine, making it 1259 crucial to design similarity measures that align with our intuitions. To facilitate 1260 efficient computation, speedup techniques are essential. Dynamic Time Warping 1261 (DTW) is arguably the most prevailing distance measure for time series data. 1262 However, studies have shown that for certain data, another distance measure, 1263 namely Uniform Scaling (US), is equally crucial as DTW. DTW handles the local 1264 distortion, while US handles the global scaling. In addition, studies have demon- 1265 strated that combining DTW and US is necessary to obtain meaningful results 1266 in some cases. Surprisingly, all existing studies employ only a single scaling fac- 1267 tor for the entire time series. A time series could consist of phases. Since each 1268 phase of a time series expresses at its own rate, using a single scaling factor is 1269 insufficient when comparing two time series that share similar phases but differ in 1270 their expression rates. We introduce the first framework that accounts for multi- 1271 ple scaling factors, Piecewise Scaling Distance (PSD). PSD employs other existing 1272 distance measures as subroutines. Because the naive implementation of PSD is 1273 slow, we propose a constrained version of PSD that enforces constraints based 1274 on the allowed segment lengths derived from the given scaling factor bound. It 1275 also prevents pathological results. In addition, two other speedup techniques have 1276 been proposed, which achieve 10.10X to 191.46X speedup. We also demonstrate 1277 the usage of a lower bound when DTW is used as the subroutine of PSD. More- 1278

1279 over, we show that the segmentation results returned by PSD can improve the
1280 accuracy of other distance measures.

1281 4.1 Background

1282 To study the mechanism of a process, we take measurements. Measurements are
1283 usually taken continuously by the sensors. Measurements of processes always yield
1284 continuous values at discrete timestamps. They are time series data. For example,
1285 smartphones collect users' GPS data. ECG monitors measure patients' heart rate.
1286 The continuous measurements compose a time series. It is not hard to see why
1287 time series data are ubiquitous across many different fields. In GPS data, each
1288 time series data point consists of the user's latitude and longitude information.
1289 They are multivariate time series. In ECG data, each data point represents the
1290 amplitude of the patient's cardiac electrical activity. They are univariate time
1291 series. In this study, we focus on univariate time series.

1292 Many data mining tasks can be defined on time series data. For example, given
1293 a time series database, we can perform clustering based on the pairwise similarity
1294 of the time series instances. A classifier can be trained when categorical labels
1295 are available. Alternatively, given a long time series, for motif finding, we iden-
1296 tify recurring patterns. In contrast, for anomaly detection, we identify abnormal
1297 subsequences. Almost all time series data mining tasks can be reduced to arguing
1298 the similarity between two time series. A good distance measure, also known as
1299 a similarity measure, can determine the success or failure of the algorithms built
1300 on it. The choice of an appropriate distance measure is particularly evident in
1301 classification. Studies show that simple nearest-neighbor classification (1-NN) is
1302 difficult to beat and can compete with more complex methods [39].

1303 A time series is treated as a whole rather than as a collection of individual val-
1304 ues. The relationships between values are important. They constitute trends and
1305 shapes. Hence, similarity search in time series data is approximate-based rather
1306 than exact match-based [47]. Besides, different invariances should be allowed dur-
1307 ing the comparison.

1308 Dynamic Time Warping (DTW) is one of, if not the most common, similarity
1309 measures. DTW provides invariance to time distortion by aligning and measuring
1310 the similarity between two series that may be misaligned in time. However, it
1311 assumes that the time series are expressed on a similar global expression rate.
1312 This assumption limits its performance when comparing two time series expressed
1313 at different global expression rates. We often see this behavior in domains such as

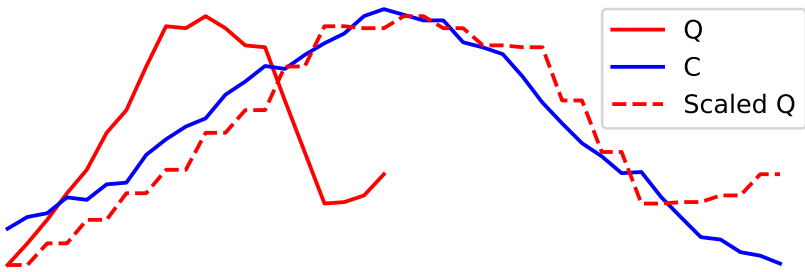


Figure 4.1: Applying nearest neighbor interpolation on Q , which result in Scaled Q , that can better reflect its similarity with C .

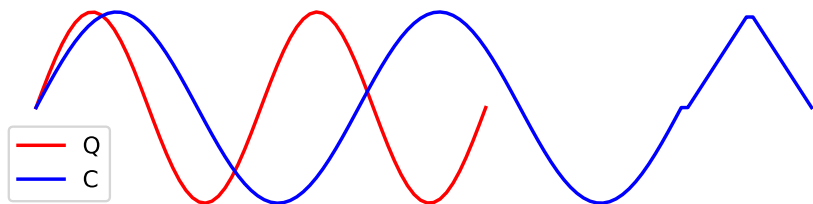


Figure 4.2: Q and C are in different rates. A stretching version of Q is similar to a prefix of C , but not the whole C .

speech recognition, motion analysis, patient biomedical signals, and sensor data ₁₃₁₄
in the manufacturing industry. ₁₃₁₅

Uniform Scaling (US) can achieve global scaling invariance by scaling the two ₁₃₁₆
time series to the same length via interpolation, such as nearest-neighbor inter- ₁₃₁₇
polation, before comparison, as shown in Figures 4.1. It is reported that in some ₁₃₁₈
domains, such as gestures [48, 49] and music performance [50], the scaling is about ₁₃₁₉
10-15% (i.e., scaling factors: 1.1 to 1.15). The scaling factors are relatively small, ₁₃₂₀
since the nature of the music and the gait will change with significant scaling ₁₃₂₁
factors. However, in some other domains, we may encounter larger scaling fac- ₁₃₂₂
tors. In bioinformatics, gene expression time series data could differ by a factor of ₁₃₂₃
1.41 [51, 52]. In Figure 4.2, Q and a prefix of C are similar, but at different rates. ₁₃₂₄
In searching, we typically have a query Q and a longer candidate C . We seek a ₁₃₂₅
prefix of C that is close to Q . For better comparison, we need to eliminate the ₁₃₂₆
scaling effect. These observations demonstrate the necessity of uniform scaling. ₁₃₂₇

DTW and US are used to achieve different kinds of invariance. DTW han- ₁₃₂₈
dles local distortion, while US handles global scaling. Furthermore, some studies ₁₃₂₉
show that the combination of US and DTW, namely USDTW, better reflects sim- ₁₃₃₀
ilarity [53, 54, 55]. US is first applied to transform the two time series into the ₁₃₃₁
same length to eliminate the effect resulting from the different rates. Then, DTW, ₁₃₃₂

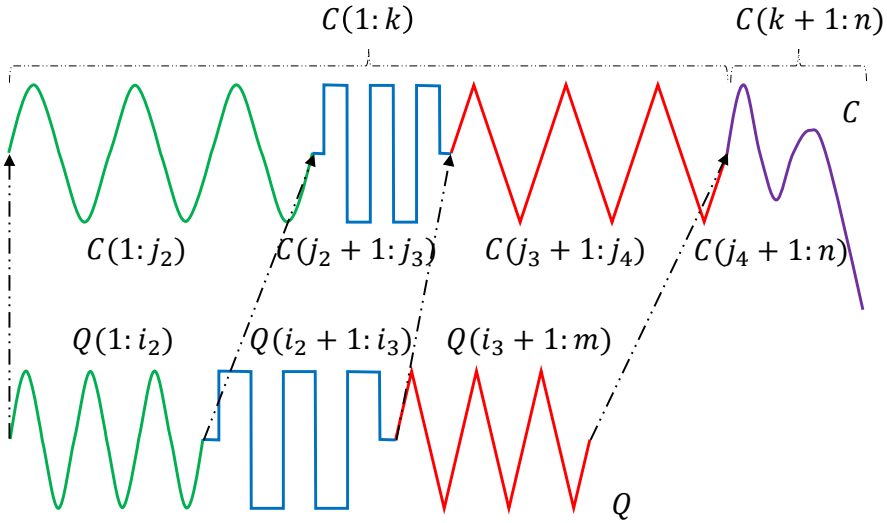


Figure 4.3: Intuition of piecewise scaling (PS).

rather than ED, is applied to address local misalignment. USDTW is computationally more expensive than DTW because it involves the calculation of the DTW between Q and different lengths of each prefix of C . The different lengths of the prefixes correspond to different scaling factors.

It is not uncommon for the data sampling strategy to change over time [56]. There are different phases, each with its own rate. To achieve invariance for this kind of scaling effect resulting from multiple rates, rather than using a single scaling factor, it is beneficial to identify these different phases and use the appropriate scaling factors for these segments, also known as pieces. We refer to this as piecewise scaling (PS). Figure 4.3 shows the intuition of PS. The prefix of C (i.e., $C(1 : k)$) and Q share the same set of segments, but each has a different scaling. Multiple scaling factors must be used. It motivates us to design a new distance measure or framework that considers applying a scaling factor on each of the phases as defined by dashed lines in Figure 4.3, during the comparison of two time series.

Our contributions are as follows:

- We propose the first framework to achieve piecewise scaling (PS) invariance. In particular, we focus on two instantiations of PSD, namely PSED (i.e., ED with PS invariance) and PSDTW (i.e., DTW with PS invariance).
- We design a dynamic programming method to compute PSD.
- We propose a constrained version of PSD (cPSD) based on the allowed segment lengths. Besides, two other speedup techniques have been proposed.

For a particular instantiation of PSD, PDTW, we demonstrate the usage of 1355
a lower bound to further speed it up. 1356

- We demonstrate that the segmentation results returned by PSD can improve 1357
the accuracy of other distance measures. 1358

The rest of this study is structured as follows. We present related work in Sec- 1359
tion 5.2 and preliminaries in Section 4.3. Section 5.3 introduces our new distance 1360
measure framework, its constrained version, and speedup techniques. It is experi- 1361
mentally demonstrated in Section 4.5 for the problem of querying. In Section 5.5, 1362
we conclude this study with some future work. 1363

4.2 Related Work

1364

This study focuses on distance measures of time series. For the overall review of 1365
time series, we direct the readers to [47, 57] for a more comprehensive understand- 1366
ing of this field. 1367

For many tasks, having appropriate distance measures that align with our 1368
intuition for the domains we work with is essential. One well-known distance 1369
measure is Dynamic Time Warping (DTW). It is initially designed for speech 1370
analysis [3]. However, DTW is computationally expensive. Lower bounds are used 1371
to speed up time series similarity search by admissibly pruning the unpromising 1372
candidates. One of the popular exact lower bounds of DTW is LB_{Keogh} . [58] 1373
improves the scalability of DTW by introducing a subsequence search suite of 1374
their four novel ideas, namely the UCR suite. For an overall review of lower 1375
bounds, we refer readers to [59, 60]. There is an approximate algorithm that 1376
approximates DTW with high accuracy while drastically cutting down the time 1377
and space requirements [61]. 1378

While ED is sensitive to distortions in the time axis, uniform scaling (US) has 1379
been shown to be a critical invariance in domains such as motion capture. [62] 1380
demonstrated that DTW is insufficient for handling global scaling effects, and that 1381
identifying DTW is not the solution to achieve this kind of invariance. There is 1382
a need for US. [63] extends the importance of uniform scaling to motif discovery. 1383
The authors show that meaningful motifs often suffer from a global scaling effect, 1384
causing standard motif finding algorithms to miss them completely. 1385

To the best of our knowledge, three studies analyze the combination of US 1386
and DTW, namely USDTW. It was first proposed by [53]. It extended LB_{Keogh} 1387
to bound the USDTW. However, the extended LB_{Keogh} is still too loose with 1388

1389 invariance to large amounts of uniform scaling. [54] and its follow-up study [55]
1390 proposed a new lower bound ¹, namely LB_{Shen}, which has been shown to be tighter
1391 than LB_{Keogh} on USDTW.

1392 To our surprise, despite a fruitful discussion of DTW, US, and USDTW, no
1393 study has proposed a distance measure capable of handling scaling effects across
1394 multiple scaling factors. This is precisely what we will address in this study.

1395 4.3 Preliminaries

1396 We refer to time as the contextual attribute because it provides the context for
1397 the measurements to be made. We refer to the measurements as the behavioral
1398 attributes. Time series are multivariate when more than one behavioral attribute
1399 is present. Otherwise, it is called univariate. We focus on the univariate case.

1400 **Definition 1** (Time Series). A time series $T = t_1, t_2, \dots, t_n$ is a sequence of real-
1401 valued numbers with length = n .

1402 When two time series are involved in the discussion, we denote them as Q
1403 (Query) and C (Candidate), with lengths m and n , respectively. Since Q is the
1404 query sequence, it is not longer than C (i.e., $m \leq n$). The requirement of " $m \leq n$ "
1405 is a natural setting. In "Query by Content", a user is going to search for a
1406 candidate in the database from a user-input query in which the query may only
1407 contain partial information of the target candidate. For example, a user often
1408 wants to find a song or tune that is lingering in their head by humming a part but
1409 not whole of the tune [64]. We are also interested in a segment or subsequence of
1410 a time series.

1411 **Definition 2** (Subsequence). A subsequence $T(i : j)$ of a time series T is a shorter
1412 time series that starts from position i and ends at position j with length = $j - i + 1$.
1413 Both ends are inclusive. Formally, $T(i : j) = t_i, t_{i+1}, \dots, t_j$, $1 \leq i \leq j \leq n$.

1414 We call $T(1 : j)$ the prefix of T of length j .

1415 Before comparison, we need to standardize or normalize them. A common way
1416 is Z-Normalization, which is $T = (T - \text{mean}(T)) / \text{std}(T)$, as shown in Figure 4.4.
1417 The most fundamental distance measure is the Euclidean Distance (ED).

¹It is denoted as LB_{New} in the original study. We rename it to prevent any confusion.

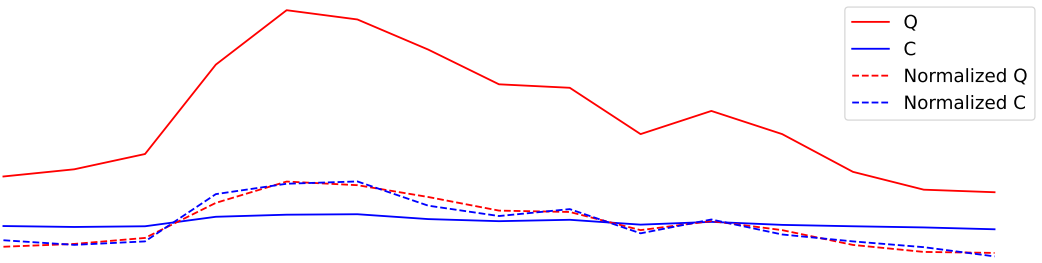


Figure 4.4: Z-normalization. Resulting time series have mean = 0 and std = 1.

4.3.1 Euclidean Distance (ED)

1418

Given two points on a plane, it is intuitive to define the distance between them 1419 as the length of the line segment between them. This idea extends to the case of 1420 n -dimensions in time series with length n . 1421

Definition 3 (Euclidean Distance (ED)). Given two series Q and C both with 1422 length n , the Euclidean Distance between them is defined as: 1423

$$\text{ED}(Q, C) = \sqrt{\sum_{i=1}^n (q_i - c_i)^2} \quad (4.1)$$

A square root is usually involved in the computation of distance measures. It is 1424 a monotonic function. Since it does not change the relative ranking of the results, 1425 we can omit the square root operation for simplicity and optimization. ED aligns 1426 the entries between two series in a one-to-one manner. Two similar series will 1427 have a large distance under ED if they are not aligned well in the time dimension. 1428 ED cannot handle local distortion along the time axis because warping in the 1429 alignment is not allowed. A standard distance measure that provides warping 1430 invariance is called Dynamic Time Warping (DTW). 1431

4.3.2 Dynamic Time Warping (DTW)

1432

Dynamic Time Warping (DTW) is an algorithm that measures similarity between 1433 two time series while accounting for local distortions. DTW aligns the two series 1434 by nonlinearly warping the time axis to minimize the final cumulative distance. 1435

Given two time series, Q and C , we first construct an m by n distance matrix 1436 M . The origin $(1, 1)$ is set at the bottom-left element of M . The (i, j) element 1437 of M contains the distance $d(q_i, c_j)$ between points q_i and c_j . This local distance 1438

1439 $d(\cdot, \cdot)$ is usually calculated by $(q_i - c_j)^2$. Each (i, j) element refers to an alignment
 1440 or mapping of the two points. A contiguous set of such elements forms a warping
 1441 path W . W represents the non-linear alignment of Q and C . $W = w_1, w_2, \dots, w_K$
 1442 in which $w_k = (i, j)_k$ represents the mapping between q_i in Q and c_j in C , where
 1443 $\max(m, n) \leq K \leq m+n-1$. “ $\max(m, n) \leq K$ ” because the alignment of two series
 1444 must include every point in both Q and C . “ $K \leq m+n-1$ ” because the longest
 1445 warping path is either the “concatenation of the bottom row and the rightmost
 1446 column” (with the bottom-right cell being overlapped) or the “concatenation of
 1447 the leftmost column and the top row” (with the top-left cell being overlapped).

1448 The warping path W is typically subject to the following three constraints.

- 1449 • Boundary conditions: $w_1 = (1, 1)$ and $w_K = (m, n)$. The first (last) point of
 1450 Q must map to that of C .
- 1451 • Continuity: Given $w_k = (i, j)$ and $w_{k-1} = (i', j')$, $i - i' \leq 1$ and $j - j' \leq 1$.
 1452 An entry in the warping path W is adjacent to its one-step previous entry.
- 1453 • Monotonicity: Given $w_k = (i, j)$ and $w_{k-1} = (i', j')$, $i - i' \geq 0$ and $j - j' \geq 0$.
 1454 The warping path W does not go back.

1455 We denote W^* as a set of all allowed possible paths.

1456 **Definition 4** (Dynamic Time Warping (DTW) [3]). DTW returns the minimum
 1457 warping cost:

$$\text{DTW}(Q, C) = \min_{W \in W^*} \sum_{k=1}^{|W|} w_k \quad (4.2)$$

1458 To find the minimum warping cost and its corresponding warping path, we can
 1459 use dynamic programming (DP) to evaluate the following recurrence.

$$\begin{aligned}
 D(i, j) &= d(q_i, c_j) \\
 &+ \min \begin{cases} D(i-1, j-1), \\ D(i-1, j), \\ D(i, j-1) \end{cases}
 \end{aligned} \quad (4.3)$$

1460 It can be solved by building the accumulated cost matrix D , where the y-
 1461 axis refers to Q , and the x-axis refers to C . The base cases, which are the first
 1462 row and the first column, are defined as $D(1, j) = \sum_{k=1}^j d(q_1, c_k), j \in [1, n]$ and
 1463 $D(i, 1) = \sum_{k=1}^i d(q_k, c_1), i \in [1, m]$. After we have initialized the base cases, we

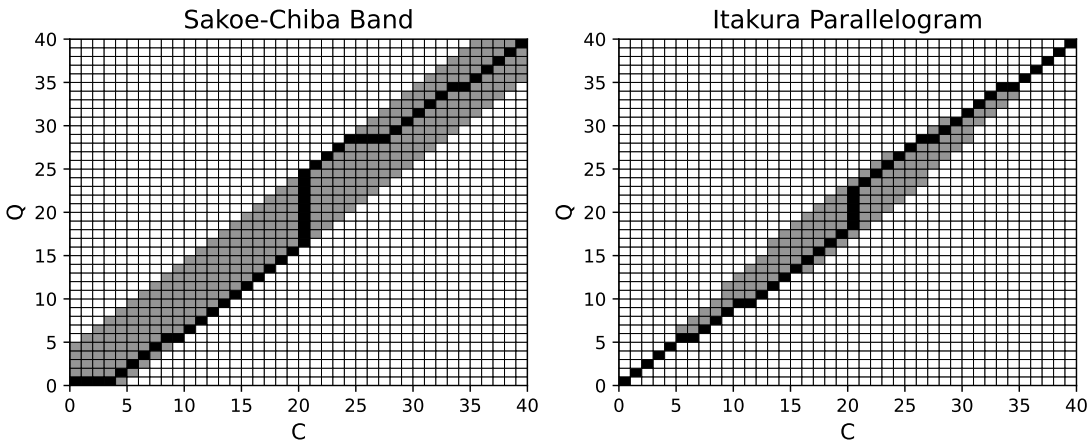


Figure 4.5: Visualization of D with local constraints. The black cells form the warping path.

can fill up D starting from the bottom up. There are $m \times n$ entries in D . It takes ¹⁴⁶⁴
 $\mathcal{O}(mn)$ to fill it up. Once D is built, we can find the path corresponding to this ¹⁴⁶⁵
minimum cost by simple backtracking from the end cell $D(m, n)$ to the origin cell ¹⁴⁶⁶
 $D(1, 1)$. ¹⁴⁶⁷

Some constraints have been proposed to prevent pathological warping paths ¹⁴⁶⁸
with the aim of accuracy and efficiency. Two of the most popular are Sakoe-Chiba ¹⁴⁶⁹
Band [3] and Itakura Parallelogram [65]. They only allow the warping paths to ¹⁴⁷⁰
pass through the allowed region, as shown in Figure 4.5, by setting the cells outside ¹⁴⁷¹
this region in D to have ∞ accumulated distance cost. [66] suggested that these ¹⁴⁷²
constraints can be viewed as constraints on the warping path entry $w_k = (i, j)_k$. It ¹⁴⁷³
represents these constraints as inequalities applying to the indices i and j locally, ¹⁴⁷⁴
without depending on the main diagonal in D . In the Sakoe-Chiba Band, the ¹⁴⁷⁵
constraints can be represented as $j - r \leq i \leq j + r$, where r is an integer. It is ¹⁴⁷⁶
sometimes specified as a fraction (or percentage) of the longer time series length ¹⁴⁷⁷
to ensure length invariance. For clarity, we assume r is an integer unless specified ¹⁴⁷⁸
otherwise. This means that q_i can only align with c_j if their indices differ by at ¹⁴⁷⁹
most r . Since r defines the maximum allowed difference between the mapping ¹⁴⁸⁰
indices, $|n - m| \leq r$, to ensure that the end points of Q and C can map. In the ¹⁴⁸¹
Itakura Parallelogram, r is a function of i rather than a constant value. ED can ¹⁴⁸²
be seen as a special case of DTW where the warping path is fixed to be diagonal. ¹⁴⁸³
 q_i aligns to c_i for every i (i.e., $r = 0$). DTW minimizes over all possible warping ¹⁴⁸⁴
paths, and the warping path of ED is one of them. Because of the band, we only ¹⁴⁸⁵
need to fill up the cells within the band. The complexity is $\mathcal{O}(\#_{_of_cells_inside})$. ¹⁴⁸⁶

1487 In the case of the Sakoe-Chiba Band, the band has a constant width $w = 2r + 1$.
1488 The complexity becomes $\mathcal{O}(w \times \text{length_of_diagonal}) = \mathcal{O}(rn)$. The constrained
1489 DTW is denoted as DTW_r .

1490 4.3.3 Uniform Scaling (US)

1491 In US, we compare the whole sequence of Q to a prefix of C , as shown in Figure 4.2.
1492 The two compared sequences are scaled to the same length via interpolation before
1493 ED is applied. A common interpolation method is nearest neighbor interpolation.

1494 **Definition 5** (Nearest Neighbor Interpolation). Given a time series T of length
1495 n and an integer L , Nearest Neighbor Interpolation scales T into T^L as follows:

$$T_j^L = T_{\lceil n(j/L) \rceil} \quad \text{where } 1 \leq j \leq L \quad (4.4)$$

1496 We can scale up or down a given series using Equation 4.4, as shown in Exam-
1497 ple 1.

1498 **Example 1.** Given a series $T = 1, 2, \dots, 6$ with length $n = 6$. Let $T(1 : 4)$ be
1499 the prefix of T of length $k = 4$ (i.e., $T(1 : 4) = 1, 2, 3, 4$). Given an integer $L = 8$,
1500 we compute $T(1 : 4)^8$ as follows.

$$\begin{aligned} T(1 : 4)^8 &= T_{\lceil 4(1/8) \rceil}, T_{\lceil 4(2/8) \rceil}, T_{\lceil 4(3/8) \rceil}, \dots, T_{\lceil 4(8/8) \rceil} \\ &= T_1, T_1, T_2, \dots, T_4 \\ &= 1, 1, 2, \dots, 4. \end{aligned}$$

1501 When $L > k$, T is said to be stretched. When $L < k$, T is said to be shrunk.

1502 **Definition 6** (Uniform Scaling (US) [62]). Given two series Q and C , of length m
1503 and n respectively, and a scaling factor bound l , where $l \geq 1$. Let $C(1 : k)$ be the
1504 prefix of C , where $\lceil m/l \rceil \leq k \leq \min(\lfloor lm \rfloor, n)$, and $C(1 : k)^L$ be a rescaled version
1505 of $C(1 : k)$ with length L , where $L = \min(\lfloor lm \rfloor, n)$. L is called the alignment
1506 factor. $\min(\lfloor lm \rfloor, n)$ is the largest alignment factor.

$$\text{US}(Q, C, l, L) = \min_{k=\lceil m/l \rceil}^{\min(\lfloor lm \rfloor, n)} \text{ED}(Q^L, C(1 : k)^L) \quad (4.5)$$

1507 L is set as the largest alignment factor [55] to ensure all the points in Q
1508 and $C(1 : k)$ are preserved during interpolation because of up-sampling, and the
1509 scaled version of all the prefixes is going to have the same length (i.e., L), for fair

comparison, since comparison between two longer time series generally results in 1510
 a larger distance measure. Through Equation 4.5, we find the minimum value 1511
 and the corresponding argument (i.e., k) by checking the minimum value of the 1512
 ED function from $\lceil m/l \rceil$ to $\min(\lfloor lm \rfloor, n)$. The scaling factor is defined by the 1513
 argument minimum value of k . The smaller k is, the more we need to “stretch” 1514
 C for Q to compare with $C(1 : k)$, which is m/k times. 1515

Consider a time series database D comprising a set of candidate instances, and 1516
 a single query series Q . The search task aims to retrieve the most similar instance 1517
 (or top- k instances) from D to Q . We maintain Q as a fixed reference and extract 1518
 only the prefixes from each instance in D for comparison. Furthermore, to simplify 1519
 notation, we apply scaling exclusively to the instances in D , leaving Q unscaled. 1520

4.3.4 Uniform Scaling & Dynamic Time Warping (US- 1521 DTW) 1522

Uniform Scaling & Dynamic Time Warping (USDTW) measures the similarity by 1523
 applying scaling with an appropriate scaling factor on C and then applying DTW. 1524
 The tail part of C can be ignored, as shown in Figure 4.2. 1525

Definition 7 (Uniform Scaling & Dynamic Time Warping (USDTW) [55]). With 1526
 the same notations defined in Definition 6, 1527

$$\text{USDTW}_r(Q, C, l, L) = \min_{k=\lceil m/l \rceil}^{\min(\lfloor lm \rfloor, n)} \text{DTW}_r(Q^L, C(1 : k)^L) \quad (4.6)$$

where r is the DTW constraint parameter. 1528

We replace the ED function in Equation 4.5 by DTW function to form Equa- 1529
 tion 4.6. 1530

As mentioned in Section 5.1, there may exist more than one scaling factor. 1531
 Hence, both the existing distance measures, US and USDTW, which are designed 1532
 to handle only one scaling factor, are insufficient. This motivates us to design a 1533
 new framework of distance measures. 1534

4.3.5 Lower Bounds for DTW and USDTW 1535

We first introduce the concept of lower bounds and explain how they can benefit 1536
 search. DTW is computationally more expensive than ED. They compute an 1537

1538 accumulated cost matrix of size $m \times n$, where m and n denote the lengths of
 1539 the two time series. It results in quadratic complexity. This complexity poses a
 1540 challenge for similarity search. The most common approach is to compute a lower
 1541 bound of the real value, which is computationally cheap and tight. We can use
 1542 this lower bound to filter out unpromising candidates and perform the expensive
 1543 distance computation only on the small set of promising candidates. In searching,
 1544 we would keep track of the best_so_far distance bsf between the query Q and
 1545 the testing candidates. When testing a new candidate C , we first compute the
 1546 $\text{LB}(Q, C)$. We only compute the actual DTW when $\text{LB}(Q, C) \leq \text{bsf}$.

1547 We then introduce some common lower bounds.

1548 **Kim Lower Bound [67]:** LB_{Kim} is a simple and fast lower bound of DTW.
 1549 The complexity is $O(1)$. It uses the four features in Q and C . We denote t_{-1} as
 1550 the last point and t_{\max} (t_{\min}) as the maximum (minimum) point in time series T .

$$\text{LB}_{\text{Kim}} = \max \begin{cases} d(q_1, c_1) \\ d(q_{-1}, c_{-1}) \\ d(q_{\max}, c_{\max}) \\ d(q_{\min}, c_{\min}) \end{cases} \quad (4.7)$$

1551 $d(\cdot, \cdot)$ refers to the local distance used in the point alignment. The first two
 1552 lines come from the boundary condition in DTW. The alignment between the first
 1553 pair of points and the last pair of points must contribute to the accumulated sum
 1554 of DTW. Each point in Q must align with some point in C , and vice versa. Each
 1555 alignment contributes a local distance to the final sum. The minimum possible
 1556 local distance for the alignment of q_{\max} would be the one aligned with c_{\max} . The
 1557 same applies to the last line in the equation.

1558 There is a simplification of LB_{Kim} . Only the first and last pair are used in
 1559 the lower bound computation. In the normalized time series, the third and fourth
 1560 rows in Equation 4.7 should have small values [58]. Ignoring them can improve
 1561 the complexity from $\mathcal{O}(n)$ to $\mathcal{O}(1)$. The simplified lower bound is $\text{LB}_{\text{KimFL}} =$
 1562 $d(q_1, c_1) + d(q_{-1}, c_{-1})$.

1563 **Keogh Lower Bound [66]:** LB_{Keogh} builds the upper U and lower envelopes L
 1564 of one of the time series out of the two compared sequences. Usually, the envelopes
 1565 are constructed for Q instead of C as we will compare one Q against many C 's.
 1566 Otherwise, we need to build the envelopes for each candidate instead [58].

1567 To the best of our knowledge, they are the first to interpret the constraint as
 1568 a restriction on the indices of the warping path $w_k = (i, j)_k$ such that $j - r \leq i \leq$

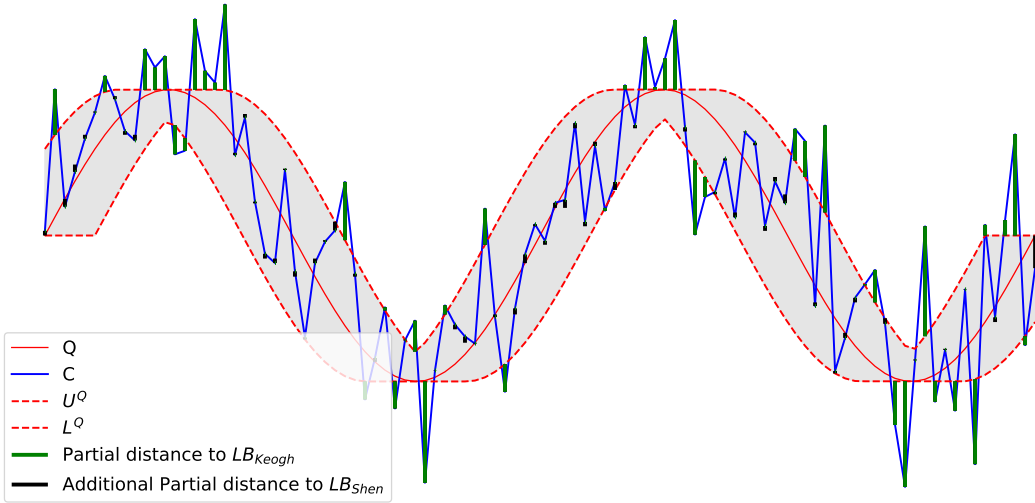


Figure 4.6: Visualization of LB_{Keogh} and LB_{Shen}

$j + r$, where r defines the allowable deviation of alignment between q_i and c_j . For 1569 ease of exposition, we focus on the most used constraint in the literature, which 1570 is the Sakoe-Chiba Band [68]. Two sequences are constructed for Q , namely the 1571 upper U^Q and lower envelopes L^Q of Q as shown in Figure 4.6. For each q_i , we 1572 would assign a window of q_i based on its index i as follows. 1573

$$\begin{aligned} U_i^Q &= \max(q_{\max(1, i-r)} : q_{\min(i+r, m)}) \\ L_i^Q &= \min(q_{\max(1, i-r)} : q_{\min(i+r, m)}) \end{aligned} \quad (4.8)$$

$\max(1, \cdot)$ and $\min(\cdot, m)$ are used for handling the boundary cases. U^Q and 1574 L^Q together form a bounding envelope that encloses the original Q , it is the grey 1575 region in the figure. For each c_j , either (c_j, U_j^Q) or (c_j, L_j^Q) corresponds to the 1576 possible alignment that contributes the minimum distances if c_j falls outside the 1577 envelope. Herein, the lower bound is the sum of these distances, as shown in the 1578 following equation. 1579

$$LB_{Keogh}(Q, C) = \sum_{j=1}^n \begin{cases} d(c_j, U_j^Q) & \text{if } c_j > U_j^Q \\ d(c_j, L_j^Q) & \text{if } c_j < L_j^Q \\ 0 & \text{otherwise} \end{cases} \quad (4.9)$$

Visually, these distances are the distances between c_j outside the envelope and 1580 the vertically corresponding points on the envelope. The distances are the green 1581 bars in the figure. Equation 4.9 returns the sum of the green bars. 1582

1583 **Shen Lower Bound [54, 55]:** It leverages the boundary and continuity conditions
 1584 to create a lower bound of DTW. It can be used to lower-bound the USDTW
 1585 with slight modification. The intuition is to find the minimum possible alignment
 1586 of each c_j with points in Q , subject to the local constraint r from DTW and the
 1587 global constraint l from US.

1588 We will first introduce LB_{Shen} for DTW. Given the candidate sequence C with
 1589 length n , for each c_j , we create its possible reach q_j in Q under DTW as in Equa-
 1590 tion 4.10. The elements q_j form an indexed collection $\mathbb{Q} = (q_1, q_2, \dots, q_{\min(\lfloor lm \rfloor, n)})$.

$$q_j = (q_{\max(1, j-r)}, \dots, q_{\min(j+r, m)}) \quad (4.10)$$

1591 We define $\delta(x, Y) = \min_{y \in Y} d(x, y)$. The possible minimum cost contributed
 1592 by the alignment of c_j and some point in Q to the accumulated sum would be
 1593 $\delta(c_j, q_j)$. The lower bound LB_{Shen} is defined as:

$$\text{LB}_{\text{Shen}}(Q, C) = d(c_1, q_1) + \sum_{j=2}^{n-1} \delta(c_j, q_j) + d(c_n, q_m) \quad (4.11)$$

1594 We direct the reader to [54] for the formal proof, while an intuition of the
 1595 proof is presented here. There are three items on the right-hand side of Equation
 1596 4.11. The continuity requirement ensures that each c_i is involved in at least one
 1597 alignment. The first and the last items are from the boundary condition. The
 1598 middle item returns the possible minimum distances contributed by each c_j 's,
 1599 where $2 \leq j \leq n - 1$. It is obvious that LB_{Shen} in Equation 4.11 is tighter when we
 1600 use the first pair of points and the last pair of points instead of doing the middle
 1601 summation all from $j = 1$ to n . It is because the distance contributed by the first
 1602 pair (last pair) must be greater than $\delta(c_1, q_1)$ ($\delta(c_n, q_n)$).

1603 It is proven that it is tighter than LB_{Keogh} [54]. It is shown in Figure 4.6 visually.
 1604 The black bars refer to the additional lower bound distance sum on top of LB_{Keogh} .
 1605 We will give an intuitive proof here. Both LB_{Keogh} and LB_{Shen} compute the lower
 1606 bounds by summing the local distance resulting from the alignment of each c_j
 1607 with some points in Q , which is guaranteed to be not greater than the partial
 1608 distance contributed by the real alignment, which we only know until we compute
 1609 the exact distance measure. In LB_{Keogh} , if this c_j falls outside the envelope, this
 1610 local distance is the vertical distance between c_j and the envelope. If c_j falls inside,
 1611 this local distance would be 0. For those points outside the envelope, the local
 1612 distances for c_j of LB_{Keogh} and LB_{Shen} are the same. But LB_{Shen} aims to return the

minimum possible partial distance for each c_j , even within the envelope. Hence, 1613
 $\text{LB}_{\text{Keogh}} \leq \text{LB}_{\text{Shen}}$. 1614

In order to compute Equation 4.11 efficiently, we first sort sequences \mathbf{q}_j and 1615
the resulting sorted sequences are denoted as $\tilde{\mathbf{q}}_j$. The sorted sequences allow us 1616
to do a binary search when we are calculating $\delta(c_j, \tilde{\mathbf{q}}_j)$ in contrast to $\delta(c_j, \mathbf{q}_j)$. 1617
The sorting only needs to be done once because we are testing the same Q with 1618
different candidates. 1619

It can be extended to the USDTW case [54, 55]. The possible reach now is not 1620
only defined by r , but also by the scaling factor bound l . 1621

$$\mathbf{q}_j = (q_{\max(1, \lceil j/l \rceil - r)}, \dots, q_{\min(\lfloor jl \rfloor + r, m)}) \quad (4.12)$$

[54] proves the following theorem to allow us to consider the lower bound 1622
between each prefix of C and Q without the scaling up of each prefix of C (i.e., 1623
 $C(1 : k)^L$) and the scaling up of Q (i.e., Q^L). 1624

Theorem 8. *For any $\lceil m/l \rceil \leq k \leq \min(\lfloor lm \rfloor, n)$, $\text{DTW}_r(Q^{\min(\lfloor lm \rfloor, n)}, C(1 : k)^{\min(\lfloor lm \rfloor, n)})$ is always lower bounded by $\sum_{j=1}^k \delta(c_j, \mathbf{q}_j)$.* 1625
1626

Recall that USDTW calculates DTW distances between each rescaled prefix 1627
of C to the rescaled Q , and outputs the minimum DTW distance, as in Equa- 1628
tion 4.6. The incremental nature of the lower bound frees us to calculate the 1629
lower bound of each DTW distance from scratch. This theorem allows us to first 1630
calculate the lower bound of the shortest prefix $C(1 : \lceil m/l \rceil)$ of C and Q , and 1631
then incrementally calculate the lower bound of the longer prefix with length from 1632
 $\lceil m/l \rceil + 1$ to $\min(\lfloor lm \rfloor, n)$ by adding on each $\delta(c_j, \mathbf{q}_j)$. To note, it also means 1633
that if $\text{LB}_{\text{Shen}}(Q, C(1 : k))$ is larger than a value, namely bsf , $\text{LB}_{\text{Shen}}(Q, C(1 : k'))$, 1634
where $k' > k$, would also be larger than bsf . To note, we can tighten LB_{Shen} by 1635
using $d(c_1, q_1)$ instead of $\delta(c_1, \mathbf{q}_1)$. 1636

The above analysis can also apply to the case of US distance. We only need 1637
to define the corresponding reaches as follows: 1638

$$\mathbf{q}_j = (q_{\max(1, \lceil j/l \rceil)}, \dots, q_{\min(\lfloor jl \rfloor, m)}) \quad (4.13)$$

4.4 Piecewise Scaling Distance

1639

The motivation stems from the limitations of US and USDTW. They assume that 1640
the relationship between Q and C is governed by only a single, global scaling 1641

1642 factor. This assumption fails when applied to multi-rate data, where different
1643 phases of the time series express at different rates.

1644 Note that existing studies [62, 58] can find all scaling factors, defined by the
1645 chosen prefix of C , ranging from $\lceil m/l \rceil$ to $\min(\lfloor lm \rfloor, n)$. However, they can use
1646 only one of them in the scaling. Consider the following illustrative example in
1647 ASCII text [58], where character repetition represents the duration of spoken
1648 phonemes, and space indicates a pause:

- 1649 • “time series 20 25” and “time series 20 25”. Here, the Hamming dis-
1650 tance (the discrete analogue of ED) fails due to misalignment in the under-
1651 lined locations, but the string edit distance (the discrete analogue of DTW)
1652 can resolve it.
- 1653 • “time sseerriiss 222000222555”. This sequence exhibits three distinct phases
1654 with scaling factors of 1, 2, and 3, respectively. The corresponding invariance
1655 cannot be achieved by DTW or US (which is restricted to a single global
1656 scalar). US would enforce a single compromised global scale instead.

1657 In Query-by-Content scenarios, such as query-by-humming or gesture retrieval,
1658 the query is generated by a human. Humans do not maintain a consistent rate
1659 for each phase. For example, humans rush through a familiar sequence but slow
1660 down for a new or complex sequence. It is commonly observed in a piece of music
1661 performed by a beginner. The piece’s tempo is not uniform.

1662 We introduce a novel distance measure framework, termed Piecewise Scaling
1663 Distance (PSD). It addresses the local scaling effect within each phase by employ-
1664 ing a scaling factor to each phase, instead of using a single scaling factor for the
1665 whole time series. It releases the basic constraint or assumption made in US and
1666 USDTW. PSD employs an existing distance metric, such as ED or DTW, to quan-
1667 tify the similarity of aligned segment pairs. While the PSD framework is agnostic
1668 to the underlying metric, this study focuses on its two fundamental instantiations:

- 1669 • PSED, which employs ED to compute the similarity of aligned segment pairs.
- 1670 • PSDTW, which employs DTW to compute the similarity of aligned segment
1671 pairs.

1672 In the formulation that follows, we utilize PSDTW as the running example.
1673 PSDTW generalizes PSED. The PSED formulation can be trivially derived from
1674 it.

4.4.1 Piecewise Scaling & Dynamic Time Warping (PS-DTW) 1675 1676

Problem formulation: To simplify the discussion, we focus on the comparison between Q and the entire sequence C , rather than a prefix of C . Note that this formulation can be generalized to prefix matching as in Definition 6 and Definition 7. 1677
1678
1679
1680

Given two sequences Q and C , where Q is not longer than C , $|Q| = m \leq |C| = n$, and the number of segments or pieces P allowed, our goal is to segmentalize both Q and C into P contiguous segments automatically in a way that minimize the total sum of DTW distance of aligned segment pairs with interpolation. 1681
1682
1683
1684

Definition 9 (Piecewise Scaling & Dynamic Time Warping (PSDTW)). With the same notations defined in Definition 7, 1685
1686

$$\begin{aligned} \text{PSDTW}_r(Q, C, l, L, P) = \\ \min_{\substack{i_1 < i_2 < \dots < i_{P+1} \\ j_1 < j_2 < \dots < j_{P+1}}} \sum_{p=1}^P \text{DTW}_r(Q(i_p + 1 : i_{p+1})^L, \\ C(j_p + 1 : j_{p+1})^L) \end{aligned} \quad (4.14)$$

, where $i_1 = 0$, $i_{P+1} = m$, $j_1 = 0$, $j_{P+1} = n$ and the setting of L will be discussed later. 1687
1688

Essentially, L needs to be at least the length of all segments to preserve all the points by up-sampling. 1689
1690

We refer to Figure 4.3 to clarify Equation 4.14. Given two sequences Q and C , with the aid of different colors and the dashed lines, we observe that Q consists of three segments while C consists of four segments, with the first three segments of C similar to those of Q . They form three segment pairs. The scaling factor used in each segment pair is determined from the length of the two subsequences involved, i.e., $(i_{p+1} - i_p)/(j_{p+1} - j_p)$. These three parts have different scaling factors. For example, the first part in C is the stretched version of that in Q . The second part in C is the compressed version of that in Q . 1691
1692
1693
1694
1695
1696
1697
1698

Equation 4.14 can be formulated in a recurrence relation as follows. Let $D[i, j, p]$ be the minimum cost to align the first i points in Q (i.e, $Q(1 : i)$) with the first j points in C (i.e., $C(1 : j)$) using exactly p segments: 1699
1700
1701

Algorithm 1 Naive PSDTW

Input: Query series Q , Candidate series C , DTW constraint parameter r (in fraction), Number of pieces P , Scaling parameter L

Output: Distance Matrix D of size $(m + 1) \times (n + 1) \times (P + 1)$

```
1: Initialize  $D$  with  $\infty$ 
2:  $D[0, 0, 0] \leftarrow 0$ 
3: for  $p \leftarrow 1$  to  $P$  do
4:   for  $i \leftarrow 1$  to  $m$  do
5:     for  $j \leftarrow 1$  to  $n$  do
6:        $D[i, j, p] \leftarrow \min_{i' < i, j' < j} \{ D[i', j', p - 1]$ 
           $+ \text{DTW}_r(Q(i' + 1 : i)^L, C(j' + 1 : j)^L) \}$ 
7: return  $D[m, n, P]$ 
```

Algorithm 2 Line 6 in Algorithm 1

```
1: for  $i' \leftarrow 0$  to  $i - 1$  do
2:   for  $j' \leftarrow 0$  to  $j - 1$  do
3:      $dist_{\text{prev}} \leftarrow D[i', j', p - 1]$ 
4:      $dist_{\text{seg}} \leftarrow \text{DTW}_r(Q(i' + 1 : i)^L, C(j' + 1 : j)^L)$ 
5:      $D[i, j, p] \leftarrow \min(D[i, j, p], dist_{\text{prev}} + dist_{\text{seg}})$ 
```

$$D[i, j, p] = \min_{\substack{i' < i \\ j' < j}} \left\{ D[i', j', p - 1] + \text{DTW}_r(Q(i' + 1 : i)^L, C(j' + 1 : j)^L) \right\} \quad (4.15)$$

1702 **Naive PSDTW:**

1703 Our goal is $D[m, n, P]$. Equation 4.15 can be solved exactly by dynamic pro-
1704 gramming (DP). The base case is $D[0, 0, 0] = 0$. It refers to the zero cost to align
1705 the first 0 point (i.e., the empty prefix) of Q with that of C . Other cells in D
1706 are first initialized with ∞ . They are calculated using a bottom-up approach via
1707 Equation 4.15. A straightforward implementation in DP is shown in Algorithm 1.
1708 Line 6 is achieved by looping all the previous indices of the current i and j as in
1709 Algorithm 2.

1710 We explain the lines in Algorithm 2. Line 3 retrieves the accumulated distance
1711 cost from the beginning up to the endpoints (i', j') , and saves it as $dist_{\text{prev}}$. Line
1712 4 considers the current aligned segment pair, which consists of $Q(i' + 1 : i)$ and
1713 $C(j' + 1, j)$, and they are interpolated to the length L . The DTW distance of this
1714 pair is calculated and saved as $dist_{\text{seg}}$.

Algorithm 3 Initialization of PSDTW

- 1: $L_{\text{gmin}}^Q \leftarrow \lceil (m/P)/\sqrt{l} \rceil, L_{\text{gmax}}^Q \leftarrow \lfloor (m/P)\sqrt{l} \rfloor$ ▷ “g” refers to “global”.
 - 2: $L_{\text{gmin}}^C \leftarrow \lceil (n/P)/\sqrt{l} \rceil, L_{\text{gmin}}^C \leftarrow \lfloor (n/P)\sqrt{l} \rfloor$
 - 3: $L = \max(L_{\text{gmax}}^Q, L_{\text{gmin}}^C)$
 - 4: Initialize D of size $(m+1) \times (n+1) \times (P+1)$ with ∞
 - 5: $D[0, 0, 0] \leftarrow 0$
-

We now analyze the time complexity of Algorithm 1. There are Pmn entries 1715 in D . The \min operator in line 6 takes $\mathcal{O}(mn)$. Hence, the time complexity 1716 of Algorithm 1 is $\mathcal{O}(Pm^2n^2) = \mathcal{O}(Pn^4)$, multiplied by the running time of the 1717 DTW. It is slow, which prevents us from using it in practice. To note, we use r 1718 in a fraction instead of a fixed integer here. This allows the deviation tolerance to 1719 scale adaptively with pieces of varying lengths. 1720

4.4.2 Speedup Techniques

1721

Length constraints of the segment: A way to reduce complexity and to 1722 prevent pathological segment pairs is to limit the possible segment lengths that are 1723 considered by constraining the minimum and maximum lengths of segments. It is 1724 similar to constrained DTW, in which we limit the search space of the warping path 1725 as in Figure 4.5. The version of PSDTW that considers the segment constraint 1726 is termed constrained PSDTW (cPSDTW). It is shown in Algorithm 4. The 1727 uncolored part shows the main logic, while the colored part shows the speedup 1728 techniques, which will be explained later. 1729

We initialize in Algorithm 3. For a given number of segments P , the expected 1730 length of each segment in Q and C would be m/P and n/P , respectively. For 1731 Q , we set the minimum possible segment length L_{gmin}^Q to be $\lceil (m/P)/\sqrt{l} \rceil$ and the 1732 maximum possible length L_{gmax}^Q to be $\lfloor (m/P)\sqrt{l} \rfloor$ in line 1 such that the scaling 1733 ratio of any two segments in Q would be bounded by l . It allows some deviation 1734 in the length of the segments from their expected length. Similarly, we compute 1735 the segment constraints for C in line 2. We set the maximum segment length be 1736 the alignment factor L in line 3. We set the base case in line 5. 1737

We fill the table D in Algorithm 4. In line 3, given p pieces in Q , the ending 1738 index of the last piece (i.e., the p^{th} piece) will range from $(p \cdot L_{\text{gmin}}^Q)$, given all the 1739 p pieces are in minimum length L_{gmin}^Q , to $\min(p \cdot L_{\text{gmax}}^Q, m)$, given all the p pieces 1740 are in maximum length L_{gmax}^Q . 1741

In line 4, we enumerate for all the allowed lengths L^Q . For the segment with 1742 length L^Q in Q , the length L^C of the corresponding aligned segment in C will 1743

Algorithm 4 Constrained PSDTW (cPSDTW) with early abandoning and lower bounding

Input: Query series Q , Candidate series C , DTW constraint parameter r (in fraction), Number of pieces P , best_so_far bsf

Output: The final distance $D[m, n, P]$ if $D[m, n, P] \leq \text{bsf}$, otherwise ∞

1: Execute Algorithm 3 for initialization

2: for $p \leftarrow 1$ to P do

```

3:   for  $i \leftarrow (p \cdot L_{\text{gmin}}^Q)$  to  $\min(p \cdot L_{\text{gmax}}^Q, m)$  do           ▷ The iterations can be parallelized.
4:     for  $L^Q \leftarrow L_{\text{gmin}}^Q$  to  $L_{\text{gmax}}^Q$  do
5:        $i' \leftarrow i - L^Q$                                 ▷  $i'$ : End point of previous segment on  $Q$ .
6:        $Q' \leftarrow \text{rev}(Q(i'+1 : i))$                   ▷  $\text{rev}(T)$ : Reverse the input series  $T$ .
7:        $L_{\text{min}}^C \leftarrow \max(L_{\text{gmin}}^C, \lceil L^Q/l \rceil)$ 
8:        $L_{\text{max}}^C \leftarrow \min(\lfloor L^Q/l \rfloor, L_{\text{gmax}}^C)$ 
9:        $r' \leftarrow r \times \max(L^Q, L_{\text{max}}^C)$           ▷ Compute the integer value of  $r$ .
10:      for  $k \leftarrow 1$  to  $L_{\text{max}}^C$  do
11:         $\mathbb{Q}_k \leftarrow (q'_{\max(1, \lceil k/l \rceil - r')}, \dots, q'_{\min(\lfloor kl \rfloor + r', L^Q)})$  ▷ Construct indexed collection  $\mathbb{Q}$ .
12:         $\tilde{\mathbb{Q}}_k \leftarrow \text{sort}(\mathbb{Q}_k)$ 
13:        for  $j \leftarrow (p \cdot L_{\text{gmin}}^C)$  to  $\min(p \cdot L_{\text{gmax}}^C, n)$  do
14:          for  $L^C \leftarrow L_{\text{min}}^C$  to  $L_{\text{max}}^C$  do
15:             $j' \leftarrow j - L^C$ 
16:             $C' \leftarrow \text{rev}(C(j'+1 : j))$ 
17:             $dist_{\text{prev}} \leftarrow D[i', j', p-1]$ 
18:            if  $dist_{\text{prev}} = \infty$  then
19:              continue
20:            if  $dist_{\text{prev}} > \text{bsf}$  then
21:              continue
22:            if  $dist_{\text{prev}} > D[i, j, p]$  then           ▷  $D[i, j, p]$  stores the best so far.
23:              continue
24:            if  $L^C = L_{\text{min}}^C$  then           ▷ Compute the lower bound from sketch.
25:               $lb = (c'_1 - q'_1)^2$  ▷ Partial distance contributed by the first alignment.
26:              for  $k \leftarrow 2$  to  $L^C$  do
27:                 $lb = lb + \delta(c'_k, \tilde{\mathbb{Q}}_k)$ 
28:            else
29:               $lb = lb + \delta(c'_{L^C}, \tilde{\mathbb{Q}}_{L^C})$  ▷ Compute the lower bound incrementally.
30:               $lb_{\text{check}} = lb - \delta(c'_{L^C}, \tilde{\mathbb{Q}}_{L^C}) + (c'_{-1} - q'_{-1})^2$  ▷ Tighten the lower bound
31:              by using the last alignment.
32:              if  $dist_{\text{prev}} + lb_{\text{check}} > D[i, j, p]$  then
33:                continue
34:                 $dist_{\text{seg}} \leftarrow \text{DTW}_r(Q'^L, C'^L)$ 
35:                if  $dist_{\text{prev}} + dist_{\text{seg}} < D[i, j, p]$  then
36:                   $D[i, j, p] \leftarrow dist_{\text{prev}} + dist_{\text{seg}}$  ▷ Also save pointer  $(i', j')$  for the cut.
37:   return  $D[m, n, P]$ 

```

have a range from L_{\min}^C to L_{\max}^C , as defined in lines 7–8, such that the ratio of L^Q and L^C would be bounded by l . Because L^Q and L^C increase in line 4 and line 14, and the i and j are fixed by the outer loop, in line 3 and line 13, respectively, the i' and j' decrease correspondingly. It is visualized in Figure 4.7. A segment in Q with ending index i and starting index $i' + 1$ would be compared to a set of segments in C , all of which have a fixed end at j and a decreasing starting index,

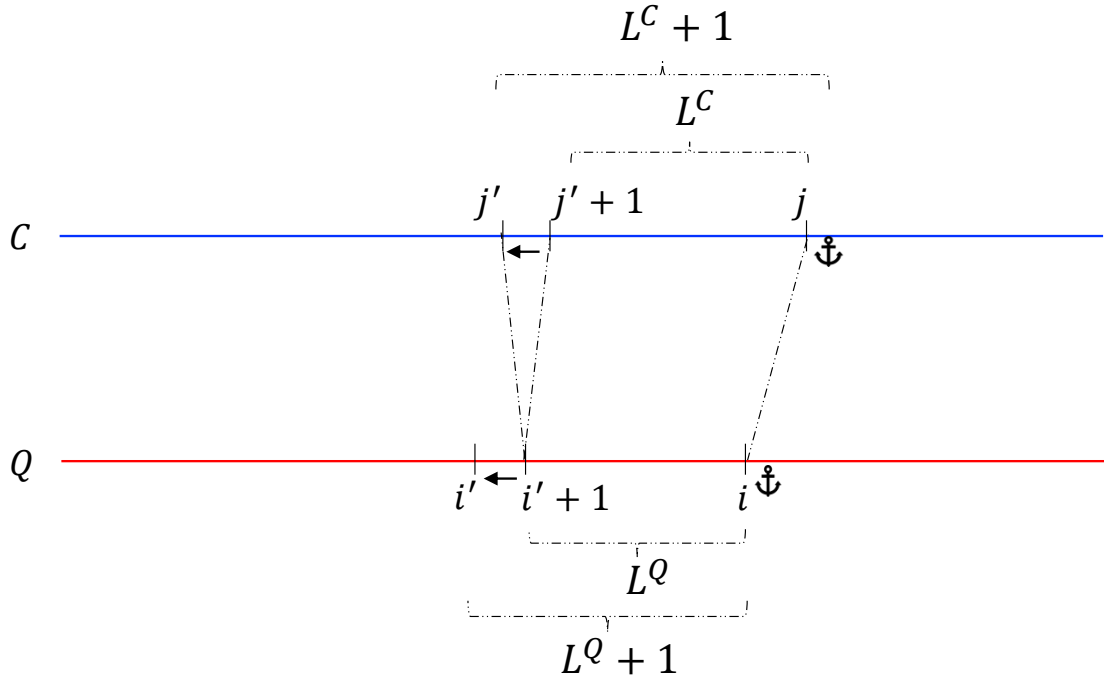


Figure 4.7: Relationship of L_Q and L_C .

starting at $j' + 1$. For example, the starting index of the first segment with being compared is $j' + 1$, which has length L^C , and that of the second segment is j' , which has length $L^C + 1$, as in Figure 4.7.

In line 18, we terminate the current iteration if there are no previously valid segment pairs (i.e., $dist_{prev} = \infty$).

In line 22, if the accumulated cost $dist_{prev}$ exceeds the current best so far, we stop the current iteration as the resulting $(dist_{prev} + dist_{seg})$ is guaranteed to be greater than the current best so far, which is stored in $D[i, j, p]$.

To be consistent with the result of using the lower bound speedup technique, which will be introduced later, we compute the DTW in the reverse manner in line 33. Due to the nearest neighbor interpolation, $DTW_r(Q^L, C'^L)$ may not equal to $DTW_r(\text{rev}(Q')^L, \text{rev}(C')^L)$.

In line 35, we also save the pairs (i', j') that serve as cutting points between segments to obtain the segmentation result.

Parallel computing: We observe that the recurrence relation for the state $D[i, j, p]$ at stage p depends exclusively on the states computed at stage $p - 1$, as shown in Equation 4.15. There are no stage dependencies over indices i and j . It allows us to parallelize the loops over indices i and j on lines 3 and 13. In the following experimental section, we distribute the i-loop iterations (i.e., line 3 in

1769 Algorithm 4, which is colored in blue) across available threads only because there
1770 are already sufficient iterations from the i-loop to fill the available threads. There
1771 are $(\min(p \cdot L_{g\max}^Q, m) - (p \cdot L_{g\min}^Q) + 1)$ iterations from the i-loop. The parallel
1772 execution of the *i*-loop is implemented by `prange` in Numba in Python.

1773 **Early Abandoning in nearest neighbor search:** To accelerate the nearest
1774 neighbor search (or top- k search) for a query Q on a candidate set, we employ an
1775 early abandoning strategy. It prunes the search branch within the PSD compu-
1776 tation of a specific candidate C as soon as the result corresponding to this search
1777 branch is determined to be suboptimal. We maintain a variable, bsf (best-so-far),
1778 which represents the minimum final distance among the candidates processed with
1779 Q so far. bsf serves as an upper-bound threshold. During the evaluation of a new
1780 candidate C , we monitor the accumulated partial distance, $\text{dist}_{\text{prev}}$. If $\text{dist}_{\text{prev}}$
1781 exceeds bsf , the corresponding final distance is guaranteed to exceed bsf . In such
1782 cases, the current search branch is immediately terminated. The implementation
1783 of this pruning mechanism is detailed in lines 20–21 in Algorithm 4, which are
1784 colored in orange. In the case of top- k search, we must maintain the top- k final
1785 distances and use the k -th distance as the threshold.

1786 **Lower bound:**

1787 When we use DTW as a routine in PSD, the computation of the DTW of the
1788 interpolated segment can be sped up by computing LB_{Shen} for the lower bound.
1789 From Figure 4.7, we observe that a segment of Q , with length L^Q , is compared
1790 to a set of growing segments of C , with a fixed end at j . The length of these
1791 segments is from L_{\min}^C to L_{\max}^C , as indicated in line 14 in Algorithm 4. They
1792 share the same suffix with length L_{\min}^C . It encourages us to view both Q and C
1793 reversely. The reversed segments are denoted as Q' and C' , as in lines 6 and 16 in
1794 Algorithm 4. In this reversed view, they share the same prefix with length L_{\min}^C .
1795 Hence, we construct an indexed collection $\tilde{\mathbb{Q}}$ for Q' with the maximum length of
1796 the segments being compared in C , which is L_{\max}^C , as in lines 10–12.

1797 In lines 24–27, we first compute the lower bound between Q' and the shortest
1798 segment of C . We add the minimum possible contribution of each c' to the distance
1799 contributed by the first alignment, which is $lb = (c'_1 - q'_1)$. For the lower bound of
1800 the subsequent segments, we compute them incrementally in line 29. Because the
1801 last point of segment C' must map to the last point of Q' , we further tighten the
1802 lower bound by using the last alignment in line 30 instead.

1803 Furthermore, we can reduce the computational overhead of constructing the
1804 sorted reaches $\tilde{\mathbb{q}}_k$ (lines 9–12). As illustrated in Figure 4.7, the segment of Q in-
1805 volved in the comparison grows incrementally. Since the reversed versions of these

Algorithm 5 Replace lines 3 to 9 in Algorithm 5 to reuse the computed sorted reaches \tilde{q}_k .

```

1:  $r'_{\text{cache}} \leftarrow -1$ 
2: for  $i \leftarrow (p \cdot L_{\text{gmin}}^Q)$  to  $\min(p \cdot L_{\text{gmax}}^Q, m)$  do
3:   for  $L^Q \leftarrow L_{\text{gmin}}^Q$  to  $L_{\text{gmax}}^Q$  do
4:      $i' \leftarrow i - L^Q$ 
5:      $Q' \leftarrow \text{rev}(Q(i' + 1 : i))$ 
6:      $L_{\text{min}}^C \leftarrow \max(L_{\text{gmin}}^C, \lceil L^Q/l \rceil)$ 
7:      $L_{\text{max}}^C \leftarrow \min(\lfloor L^Q/l \rfloor, L_{\text{gmax}}^C)$ 
8:      $r' \leftarrow r \times \max(L^Q, L_{\text{max}}^C)$ 
9:     if  $r'_{\text{cache}} = r'$  then
10:    for  $k \leftarrow 1$  to  $L_{\text{max}}^C$  do
11:      if  $k \leq |Q'|$  then
12:         $e_{\text{prev}} \leftarrow \min(\lfloor kl \rfloor + r', L^Q - 1)$ 
13:         $e_{\text{new}} \leftarrow \min(\lfloor kl \rfloor + r', L^Q)$ 
14:        if  $e_{\text{new}} > e_{\text{prev}}$  then
15:           $\tilde{q}_k \leftarrow \tilde{q}_k \cup q'_{e_{\text{new}}}$ 
16:        else
17:           $q_k \leftarrow (q'_{\max(1, \lceil k/l \rceil - r')}, \dots, q'_{\min(\lfloor kl \rfloor + r', L^Q)})$   $\triangleright L^Q$  equals to  $|Q'|$ .
18:           $\tilde{q}_k \leftarrow \text{sort}(q_k)$ 
19:        else
20:          for  $k \leftarrow 1$  to  $L_{\text{max}}^C$  do
21:             $q_k \leftarrow (q'_{\max(1, \lceil k/l \rceil - r')}, \dots, q'_{\min(\lfloor kl \rfloor + r', L^Q)})$ 
22:             $\tilde{q}_k \leftarrow \text{sort}(q_k)$ 
23:           $r_{\text{cache}} \leftarrow r'$ 

```

segments share a common prefix, the sorted reaches \tilde{q}_k computed for a segment Q' of length L^Q can be reused to compute those for the subsequent segments. This optimization is detailed in Algorithm 5, with the new components highlighted in blue. It is important to note that because r' is a function of L^Q , and the construction of \tilde{q}_k depends on r , reuse is limited to cases where r' remains constant. We construct reaches \tilde{q}_k from the sketch in lines 20–22 and keep track of the r' used for construction in line 23. If r' remains constant, we can use previously computed reaches \tilde{q}_k to compute the new set of reaches \tilde{q}_k . Since the ending index of reaches depends on $\min(\lfloor kl \rfloor + r', L^Q)$, we need to check whether we have a new ending index when L^Q increases. If the ending index has been changed, we need to add the new data points $q'_{e_{\text{new}}}$ to the sorted sequence \tilde{q}_k , as in line 15.

L_{max}^C depends of L^Q . If L_{max}^C increase because L^Q increase, we construct the new reach \tilde{q}_k and sort it in lines 16–18.

1819 **4.4.3 Guided Distance**

1820 For faster computation, one would want to use a distance measure with linear
1821 complexity, such as ED, as the base measure for PSD. While PSED is effective
1822 for identifying phase-scaling changes, certain applications require capturing com-
1823 plex properties within those segments that ED cannot handle. There are two
1824 ways to address it. One approach is to use an alternative distance measure that
1825 captures these complex properties as the base distance for computing the PSD,
1826 such as DTW. But PSDTW is slower than PSED. The other approach is to use
1827 the segmentation result returned by PSED. To address this, we propose a two-
1828 stage framework in which PSED-derived segmentation guides the application of
1829 advanced distance metrics M . Let $\mathcal{P}^* = \{(i_1, j_1), (i_2, j_2), \dots, (i_{P+1}, j_{P+1})\}$ be the
1830 set of optimal cut points on Q and C obtained by minimizing the PSED. We utilize
1831 \mathcal{P}^* to partition both series into P aligned pairs of segments. The final distance,
1832 denoted as M^{PSED} , is calculated by summing the distances of these pairs using a
1833 target metric M :

$$M^{\text{PSED}}(Q, C) = \sum_{p=1}^P M(Q_p^L, C_p^L) \quad (4.16)$$

1834 , where $Q_p = Q(i_p + 1 : i_{p+1})$ and $C_p = C(j_p + 1 : j_{p+1})$.

1835 **4.5 Experiments**

1836 We evaluate the performance of our proposed distance measure framework, PSD,
1837 via its two instantiations: PSED and PSDTW. Specifically, we focus on a query
1838 retrieval task in which the query exhibits piecewise-scaled distortion, that is, dis-
1839 tinct phases of the query exhibit different expression rates relative to the target
1840 in the candidate dataset. Our objective is to verify whether PSD achieves invari-
1841 ance to these multiple scaling distortions, thereby allowing it to correctly retrieve
1842 the most similar candidate. We detail the experimental setup in Section 4.5.1
1843 and present the results in Section 4.5.2. The code and data are available at
1844 <https://github.com/colemanyu/k-scaling-factor-dtw>.

1845 **4.5.1 Experimental Setup**

1846 We utilize the GunPoint dataset, originally released in 2003 [69], as the running
1847 example. Widely regarded as the “iris” dataset of the time series community [70],

it has appeared in over one thousand publications. Beyond its ubiquity, the dataset addresses a critical distinction: misinterpreting the act of aiming a gun as merely pointing a finger could have life-threatening consequences.

1848
1849
1850

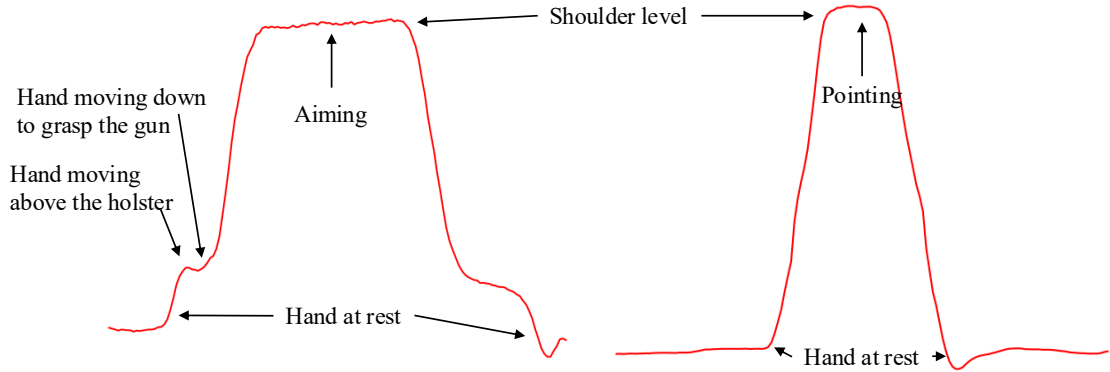


Figure 4.8: Visualization of the GunPoint dataset. Left (Right): A time series of the “Gun” (“Point”) scenario. Critical periods, such as “Aiming”, are annotated.

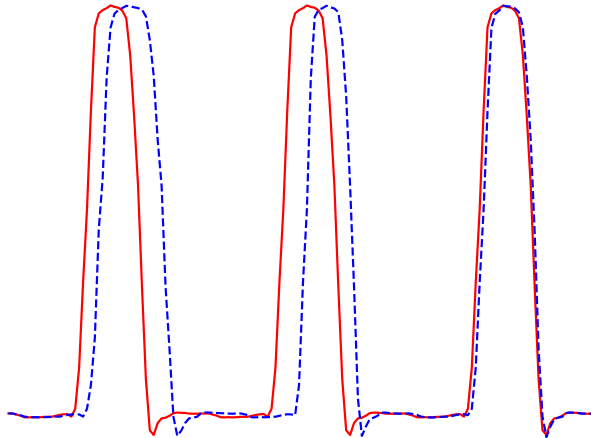


Figure 4.9: The red solid time series shows an instant in the target set. The blue dashed time series shows an instant in the query set.

The dataset contains two classes: “Gun” and Point”. Actors aim at an eye-level target using either a replica gun or their index finger, as illustrated in Figure 4.8. The resulting time series represent the X-axis centroid of the actor’s right hand. Each action lasts for 5 seconds, with the pointing/aiming phase occurring for approximately one second. Recorded at 30 fps, each sample consists of 150 data points. The dataset comprises 50 training and 150 test series, all of length 150.

A key limitation of the original dataset is the assumption that every action lasts exactly 5 seconds. In reality, actors perform actions at varying speeds. If an

1859 actor is asked to perform the action three times continuously in a row, we are likely
1860 to observe a time series containing three phases, each with a unique rate. The
1861 first phase should take longer than subsequent phases because it is the first time
1862 the action is performed. This phenomenon is depicted in Figure 4.9, where the
1863 red curve represents an ideal case that consists of three identical phases (i.e., iden-
1864 tical rate), while the blue curve represents a realistic scenario with varying rates.
1865 The first action is slower than the second action. Consequently, retrieving such
1866 patterns requires assigning different scaling factors to each phase to accommodate
1867 the phase-specific rates.

1868 We now describe the procedure for generating the target and query sets for
1869 the retrieval task. To construct the target set, we concatenate P repetitions of
1870 each time series instance from the source dataset. To ensure a fair comparison, we
1871 constrain the resulting time series to match the original length n . This is achieved
1872 by rescaling each phase to a length of n/P prior to concatenation. Note that we
1873 must handle remainders to ensure that the final time series length is exactly n .
1874 An example of such a target (where $P = 3$) is depicted by the red solid line in
1875 Figure 4.9.

1876 To construct the query set, we first determine the specific lengths for the P
1877 segments. Starting with an expected mean length of n/P , we define the minimum
1878 segment length as $L_{\min} = (n/P)\sqrt{l}$ and the maximum as $L_{\max} = (n/P)\sqrt{l}$. This
1879 formulation ensures that the ratio of the lengths of any two segments is bounded
1880 by l . We then generate P random integers within $[L_{\min}, L_{\max}]$ subject to the con-
1881 straint that their sum is exactly n . Finally, we construct the query by rescaling P
1882 copies of the source time series to these generated random lengths and concatena-
1883 ting them. The resulting time series maintains the original length n . An example
1884 of such a query (where $P = 3$) is depicted by the blue dashed line in Figure 4.9.

1885 Both the query and target sets are derived from the same source dataset.
1886 Consequently, the ground truth target for a given query is defined as the instance
1887 in the target set that is generated from the same underlying source time series.

1888 Table 4.1 details the additional datasets used in this study. The column labeled
1889 “Train/Test?” specifies which split was employed as the source dataset.

1890 In our experiments, we set the warping window parameter $r = 0.1$, as suggested
1891 in the literature. The algorithms were implemented in Python. We utilized the
1892 `aeon` [71] library to obtain the baseline distance measures. All experiments were
1893 conducted on a workstation equipped with an Intel Xeon Gold 6326 CPU and
1894 256GB of RAM.

Table 4.1: Details of the ten datasets for the experiments

Name	Type	Train/Test?	Size	Class	Length
SonyAIBORobotSurface1	Sensor	Test	601	2	70
ECG200	ECG	Train	100	2	96
MedicalImages	Image	Train	381	10	99
CBF	Simulated	Train	30	3	128
SwedishLeaf	HAR	Train	500	15	128
Plane	Sensor	Train	105	7	144
PowerCons	Device	Train	180	2	144
GunPoint	HAR	Train	50	2	150
Adiac	Image	Train	390	37	176
Epilepsy	HAR	Train	137	4	207

4.5.2 Experimental Results

We employ Top- k Accuracy (often referred to as Precision@ k [72]) as the primary evaluation metric. For a single query Q , this metric indicates whether the correct match is successfully retrieved within the top k candidates:

$$P@k(Q) = \begin{cases} 1 & \text{if the ground truth is in the top-}k \text{ results} \\ 0 & \text{otherwise} \end{cases} \quad (4.17)$$

To determine the top- k results, we compute the distance between Q and every time series in the target set, generating a distance profile of length equal to the dataset size. The top- k results correspond to the k instances with the smallest distances in this profile. Finally, we evaluate the overall performance by computing the mean Top- k Accuracy across the entire query set \mathcal{D} :

$$\overline{P@k} = \frac{\sum_{Q \in \mathcal{D}} P@k(Q)}{|\mathcal{D}|} \quad (4.18)$$

We choose $k \in \{1, 3\}$. $k = 1$ refers to the exact retrieval. $k = 3$ give some tolerance for the retrieval.

Results of GunPoint dataset: We utilize the GunPoint dataset to evaluate how the parameters P and l affect the ability of PSD to achieve invariance under piecewise scaling. The results are presented in Table 4.2, where the best performance of $\overline{P@1}$ is highlighted in bold, and the second-best is underlined. We benchmark our method against several state-of-the-art distance measures, including ADTW [10], DDTW [4], shapeDTW [6], WDDTW [5], and WDTW [5]., PSED

Table 4.2: The accuracy comparison for eight distance measures of the GunPoint dataset

P	l	ED		DTW [3]		ADTW [10]		DDTW [4]		shapeDTW [6]		WDDTW [5]		WDTW [5]		PSED		PSDTW	
		$P@1$	$P@3$	$P@1$	$P@3$	$P@1$	$P@3$	$P@1$	$P@3$	$P@1$	$P@3$	$P@1$	$P@3$	$P@1$	$P@3$	$P@1$	$P@3$	$P@1$	$P@3$
2	1.25	0.30	0.56	0.82	1.00	0.54	0.84	0.84	0.92	<u>0.96</u>	1.00	0.88	0.96	0.82	0.98	0.98	1.00	0.86	1.00
	1.50	0.14	0.36	0.88	1.00	0.38	0.64	0.78	0.94	1.00	1.00	0.80	0.92	0.88	0.96	1.00	1.00	<u>0.96</u>	1.00
	1.75	0.16	0.34	0.82	1.00	0.38	0.66	0.64	0.80	0.90	1.00	0.66	0.80	0.82	0.96	1.00	1.00	<u>0.94</u>	1.00
	2.00	0.12	0.24	0.84	0.98	0.34	0.66	0.72	0.88	<u>0.96</u>	1.00	0.68	0.86	0.82	0.98	1.00	1.00	<u>0.96</u>	1.00
	1.25	0.30	0.50	0.84	0.92	0.70	0.88	0.80	0.92	0.96	0.98	0.84	0.94	0.86	0.98	<u>0.94</u>	1.00	0.88	0.96
3	1.50	0.10	0.28	0.84	0.96	0.60	0.78	0.66	0.86	<u>0.90</u>	1.00	0.72	0.86	0.84	0.98	0.96	1.00	0.86	0.96
	1.75	0.10	0.28	<u>0.88</u>	1.00	0.42	0.78	0.72	0.88	0.76	0.94	0.74	0.88	<u>0.88</u>	1.00	1.00	1.00	<u>0.88</u>	0.98
	2.00	0.02	0.12	<u>0.86</u>	0.94	0.38	0.52	0.60	0.78	0.70	0.94	0.60	0.80	0.82	0.92	0.98	1.00	<u>0.86</u>	0.98
	1.25	0.34	0.50	0.70	0.86	0.68	0.88	0.60	0.78	0.70	0.90	0.64	0.80	0.70	0.86	0.86	0.94	<u>0.72</u>	0.88
4	1.50	0.22	0.38	0.64	0.80	0.60	0.92	0.52	0.64	0.68	0.90	0.52	0.66	0.64	0.82	0.86	0.98	<u>0.72</u>	0.82
	1.75	0.16	0.30	0.72	0.92	0.56	0.80	0.60	0.78	0.56	0.80	0.56	0.80	0.70	0.88	0.92	1.00	<u>0.80</u>	0.94
	2.00	0.06	0.12	0.58	0.78	0.50	0.72	0.46	0.64	0.50	0.82	0.50	0.64	0.56	0.82	0.88	0.98	<u>0.64</u>	0.88

achieves the highest accuracy, followed closely by PSDTW. We attribute PSED’s superior performance over PSDTW to the specific nature of the distortions in the query set, that is, the “pure” piecewise scaling distortions. Since the query set exhibits only piecewise scaling distortions, the corresponding segments of the query and target time series differ solely in length (scale). Consequently, the additional flexibility provided by DTW in PSDTW is unnecessary and may inadvertently increase the similarity of incorrect matches, thereby reducing discriminative power relative to the stricter PSED measure. However, PSDTW remains theoretically essential for handling local distortions within the phase. PSDTW applies DTW within the scaled segment, enabling robust alignment across local nonlinearities.

Table 4.3: The accuracy comparison for six PSED-guided distance measures of the GunPoint dataset

P	l	DTW ^{PSED}		ADTW ^{PSED}		DDTW ^{PSED}		shapeDTW ^{PSED}		WDDTW ^{PSED}		WDTW ^{PSED}	
		$P@1$	$P@3$	$P@1$	$P@3$	$P@1$	$P@3$	$P@1$	$P@3$	$P@1$	$P@3$	$P@1$	$P@3$
2	1.25	0.86	1.00	0.98	1.00	0.72	0.92	0.98	1.00	0.74	0.96	0.86	1.00
	1.50	0.88	1.00	1.00	1.00	0.60	0.90	0.98	1.00	0.64	0.90	0.92	1.00
	1.75	0.94	1.00	1.00	1.00	0.84	0.94	1.00	1.00	0.86	0.96	0.94	1.00
	2.00	0.98	1.00	1.00	1.00	0.60	0.78	0.98	1.00	0.66	0.80	0.98	1.00
	1.25	0.82	0.96	0.94	1.00	0.74	0.90	0.92	0.98	0.76	0.90	0.90	0.82
3	1.50	0.86	1.00	0.96	1.00	0.72	0.90	0.94	1.00	0.80	0.90	0.88	1.00
	1.75	0.88	1.00	1.00	1.00	0.68	0.90	1.00	1.00	0.70	0.94	0.90	1.00
	2.00	0.86	0.96	0.98	1.00	0.54	0.86	0.96	1.00	0.62	0.86	0.88	0.96
	1.25	0.74	0.88	0.86	0.94	0.78	0.80	0.80	0.92	0.78	0.82	0.74	0.88
4	1.50	0.72	0.84	0.86	0.98	0.68	0.84	0.84	0.96	0.66	0.84	0.72	0.86
	1.75	0.74	0.96	0.92	1.00	0.54	0.90	0.90	1.00	0.56	0.88	0.74	0.96
	2.00	0.66	0.90	0.88	0.98	0.58	0.82	0.88	0.98	0.62	0.80	0.66	0.90

We further investigate whether the segmentation results returned by PSED can serve as a guide to enhance other distance measures. As shown in Table 4.3, this approach generally improves accuracy. The exceptions are highlighted in bold,

indicating cases where the segmentation led to worse performance. Notably, in most cases, only DDTW and WDDTW failed to benefit from PSED-guided segmentation. We argue that the performance degradation of DDTW and WDDTW stems from their derivative-based nature. They rely on matching slope or shape features. Consequently, they are highly sensitive to segmentation boundaries. A non-perfect cut that falls within a shape feature segmentize it, and these features are then destroyed. When the algorithm subsequently attempts to map these features, it fails to find correct correspondences, resulting in high distances.

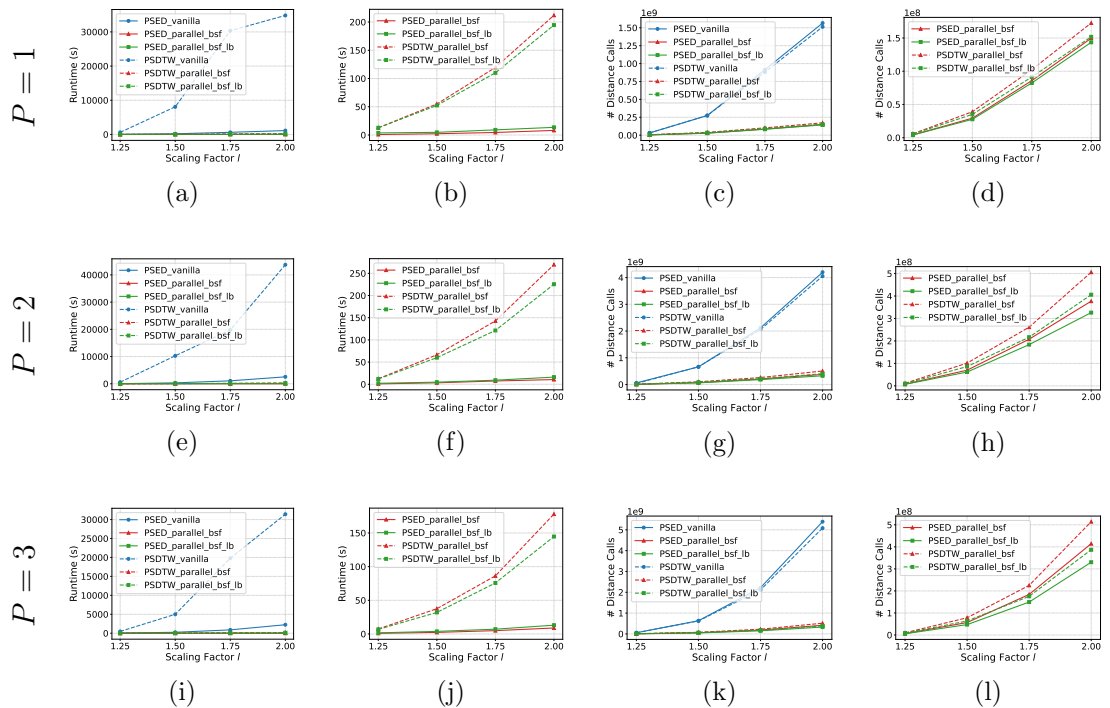


Figure 4.10: Runtime and number of distance calls comparison of GunPoint dataset. (a)-(d) $P = 1$, (e)-(h) $P = 2$, (i)-(l) $P = 3$.

Figure 4.10 illustrates the runtime performance across varying parameters P and l . We evaluate two variants of PSD, PSED and PSDTW, each implemented with three levels of

1. **vanilla** (i.e., Basic implementation)
2. **parallel_bsfc** (i.e., With parallelization with Best-So-Far early abandoning)
3. **parallel_bsfc_lb** (i.e., Incorporating lower bound pruning)

This yields a total of six methods. The figure is organized into four columns plotted against the scaling factor l . The rows refer to the number of pieces P .

1941 The first and third columns display the running time and the number of distance
 1942 calculations, respectively, for all six methods. To better visualize the performance
 1943 differences among the efficient implementations, the second and fourth columns
 1944 omit the **vanilla** baselines and focus exclusively on the four optimized variants.

1945 The results indicate that **vanilla_PSDTW** is orders of magnitude slower than
 1946 the other approaches, whereas the optimized methods operate within a similar per-
 1947 formance range. As anticipated, the computation time for all methods increases
 1948 with the scaling factor l . The fourth column confirms that the lower bounding
 1949 strategy effectively reduces the number of distance calculations (pruning power).
 1950 However, the second column reveals a critical trade-off in actual runtime. While
 1951 the lower bound successfully accelerates PSDTW, it actually slows down PSED.
 1952 This suggests that for the computationally lighter ED, the overhead of calculat-
 1953 ing the lower bound outweighs the time saved by pruning. Overall, the results
 1954 demonstrate that PSED is significantly faster than PSDTW.

Results of the ten datasets:

Table 4.4: The accuracy comparison for eight distance measures of the ten datasets

Dataset	ED		DTW		ADTW		DDTW		shapeDTW		WDDTW		WDTW		PSED	
	$P@1$	$P@3$	$P@1$	$P@3$	$P@1$	$P@3$	$P@1$	$P@3$	$P@1$	$P@3$	$P@1$	$P@3$	$P@1$	$P@3$	$P@1$	$P@3$
SonyAIBORobotSurface1	0.04	0.08	0.51	0.63	0.60	0.74	0.45	0.57	0.20	0.29	0.45	0.58	0.51	0.64	0.67	0.77
ECG200	0.12	0.20	0.70	0.81	0.78	0.83	0.60	0.74	0.59	0.76	0.59	0.73	0.70	0.80	0.81	0.88
MedicalImages	0.08	0.19	0.63	0.78	0.69	0.85	0.52	0.68	0.57	0.75	0.51	0.68	0.62	0.78	0.76	0.88
CBF	0.53	0.67	0.83	1.00	0.90	1.00	0.73	0.87	0.73	0.90	0.77	0.90	0.90	1.00	1.00	1.00
SwedishLeaf	0.07	0.12	0.82	0.92	0.84	0.93	0.70	0.83	0.78	0.91	0.69	0.83	0.83	0.92	0.97	0.99
Plane	0.09	0.14	0.50	0.74	0.59	0.78	0.38	0.64	0.53	0.79	0.37	0.61	0.49	0.75	0.75	0.93
PowerCons	0.26	0.43	0.77	0.98	0.80	1.00	0.77	0.98	0.77	0.99	0.77	0.99	0.77	0.99	0.80	1.00
GunPoint	0.10	0.28	0.84	0.96	0.60	0.78	0.66	0.86	0.90	1.00	0.72	0.86	0.84	0.98	0.96	1.00
Adiac	0.01	0.02	0.37	0.50	0.12	0.21	0.32	0.42	0.27	0.41	0.31	0.41	0.36	0.50	0.57	0.71
Epilepsy	0.18	0.26	0.74	0.88	0.80	0.91	0.65	0.82	0.38	0.47	0.58	0.79	0.70	0.83	0.83	0.91

Table 4.5: The accuracy comparison for six PSED-guided distance measures of the ten datasets

Dataset	DTW ^{PSED}				ADTW ^{PSED}				DDTW ^{PSED}				shapeDTW ^{PSED}		WDDTW ^{PSED}		WDTW ^{PSED}	
	$P@1$	$P@3$	$P@1$	$P@3$	$P@1$	$P@3$	$P@1$	$P@3$	$P@1$	$P@3$	$P@1$	$P@3$	$P@1$	$P@3$	$P@1$	$P@3$	$P@1$	$P@3$
SonyAIBORobotSurface1	0.53	0.64	0.64	0.76	0.37	0.53	0.65	0.76	0.38	0.53	0.53	0.65						
ECG200	0.73	0.84	0.80	0.88	0.54	0.68	0.81	0.88	0.53	0.69	0.73	0.84						
MedicalImages	0.66	0.78	0.76	0.88	0.51	0.69	0.74	0.88	0.51	0.70	0.66	0.79						
CBF	0.90	1.00	0.93	1.00	0.73	0.93	0.93	0.97	0.97	0.70	0.93	0.90	1.00					
SwedishLeaf	0.82	0.92	0.97	0.99	0.72	0.87	0.97	0.99	0.73	0.88	0.73	0.88	0.82	0.92				
Plane	0.60	0.80	0.75	0.94	0.50	0.67	0.74	0.90	0.50	0.69	0.59	0.80						
GunPoint	0.86	1.00	0.96	1.00	0.72	0.90	0.94	1.00	0.80	0.90	0.88	1.00						
PowerCons	0.78	0.99	0.79	1.00	0.79	1.00	0.79	1.00	0.79	1.00	0.79	1.00	0.78	1.00				
Adiac	0.33	0.45	0.57	0.71	0.21	0.34	0.53	0.70	0.20	0.33	0.34	0.45						
Epilepsy	0.77	0.88	0.78	0.88	0.66	0.79	0.74	0.89	0.66	0.82	0.80	0.89						

1955

1956 For the remaining nine datasets, we fix the parameters at $P = 3$ and $l = 1.5$.
 1957 We have the following findings from the previous experiment:

Table 4.6: The number of distance calls and runtime on PSED_vanilla and PSED_parallel_bsf of the ten datasets

Name	Size	Length	PSED_vanilla	PSED_parallel_bsf	% distance calls pruned	Speed Up
			Time (s)	Time (s)		
SonyAIBORobotSurface1	601	70	697	69	90.40%	10.10X
ECG200	100	96	91	3	91.08%	30.33X
MedicalImages	381	99	2082	40	96.03%	52.05X
CBF	30	128	43	2	75.31%	21.50X
SwedishLeaf	500	128	16601	107	96.24%	155.15X
Plane	105	144	621	6	96.05%	103.50X
PowerCons	180	144	3629	49	82.32%	74.06X
GunPoint	50	150	159	3	89.42%	53.00X
Adiac	390	175	23550	123	96.71%	191.46X
Epilepsy	137	206	13131	336	39.88%	39.08X

- From Table 4.3, PSED outperformed PSDTW in handling piecewise scaling distortions. 1958
1959
- From Figure 4.10, the lower bound offered no efficiency gain for PSED. 1960

Hence, we select PSED_parallel_bsf as the representative method for this evaluation. The accuracy results are presented in Table 4.4, while the results for the PSED-guided distance measures are detailed in Table 4.5. Finally, the runtime efficiency for all datasets is summarized in Table 4.6. It shows a significant speedup, ranging from 10.10X to 191.46X. 1961
1962
1963
1964
1965

4.6 Concluding Remarks

In this study, we proposed a novel distance measure framework, Piecewise Scaling Distance (PSD), which relaxes the strict assumption of a single uniform scaling factor across the entire time series. We presented an exact dynamic programming (DP) algorithm to solve this problem. To enhance efficiency and prevent pathological segment alignments, we introduced a constraint version, which limits the search space of segment lengths based on given scaling factors. To enhance computational efficiency, we integrated two optimization techniques for the general PSD framework. In addition, we propose incorporating a lower-bounding strategy to accelerate PSDTW. Our experimental results demonstrate the necessity and effectiveness of PSD when identifying matches between a query Q and a candidate C under piecewise scaling distortions. 1966
1967
1968
1969
1970
1971
1972
1973
1974
1975
1976
1977

We outline several directions for future research. First, we aim to develop a lower bound specifically optimized for PSED that can improve actual runtime. Second, while the current PSDTW algorithm requires the number of segments P 1978
1979
1980

1981 to be specified as a hyperparameter, it is preferable for the algorithm to determine
1982 this value adaptively. A simple heuristic is to test a range of P values and select
1983 the configuration that yields the minimum distance Finally, we plan to investigate
1984 efficiency improvements for PSDTW. Currently, PSDTW computes dynamic time
1985 warping on two growing subsequences after scaling. While techniques for Incre-
1986 mental DTW [73] allow for the reuse of the accumulating cost matrix D to avoid
1987 redundant calculations, applying this to PSDTW is non-trivial. The interpolation
1988 performed before DTW fundamentally alters the subsequence structure, prevent-
1989 ing the straightforward extension of D (e.g., by appending rows or columns) to
1990 reuse the computed D that is possible in standard DTW.

Chapter 5

1991

Leveraging Nearest Neighbors for Time Series Forecasting with Matrix Profile

1992

1993

1994

5.1 Background

1995

Humans have made predictions since ancient times. In ancient societies, accurate predictions were important to the success of subsistence activities such as hunting, planting, and harvesting. There was a need to predict weather dynamics, such as rainfall and temperature. For example, it is crucial to plant during the period with sufficient rainfall and appropriate temperatures. Our ancestors used divination tools such as turtle shells, wooden blocks (moon blocks), or bones to make predictions. Without doubt, the accuracy was not guaranteed. Even in modern societies, prediction is still essential. Predicting traffic-jam patterns only a few hours ahead can save time by enabling the selection of an alternative route [74]. A wealth could be created by forecasting stock market trends. Predicting the future, also known as time series forecasting, is crucial.

With advances in hardware technologies, we collect enormous amounts of data from diverse sources, such as smart sensors and social media platforms, continuously in the form of time series data. A time series is an ordered sequence of measures, represented in real-valued numbers, at discrete equal-interval timestamps [75]. The vast data collections have created the era of “Big Data”, which provides a wealth of datasets for developing and deploying reliable, robust, data-driven forecasting techniques to discover patterns and extract valuable information [76]. Applications can be found in the financial sector, such as predicting

2015 business cycles and stock market movements [77, 74, 78, 79] and the medical field,
 2016 such as the status of critical patients according to their vital signs [80, 81] and the
 2017 propagation of diseases such as influenza [79, 82] and COVID-19 [80, 83].

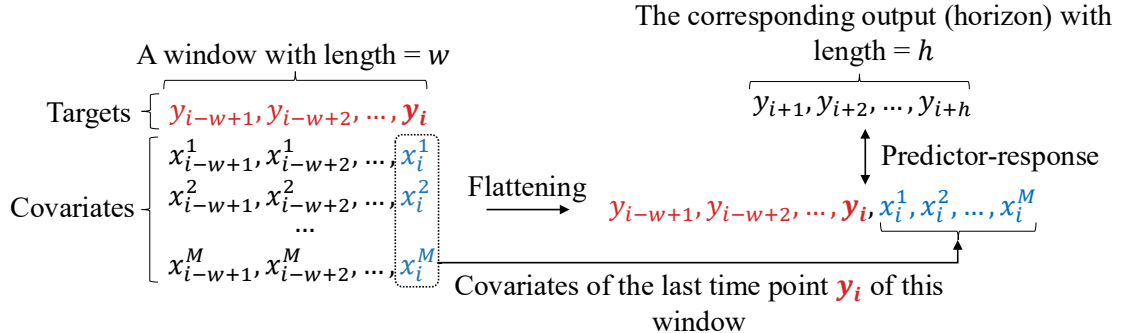


Figure 5.1: Flattening a 2D window of size $(1 + M) \times w$ to a 1D vector of length $w + M$. The resulting vector serves as the *predictor* for the regressor. Its expected *response* is the vector of length h . The regressor learns from this predictor-response pair.

2018 A recent study [1] shows that, in time series classification, a non-parametric,
 2019 instance-based method, namely nearest-neighbor classifiers (1-NN) and its gen-
 2020 eralized form k -NN, with appropriate distance measures, such as Dynamic Time
 2021 Warping (DTW), despite their simplicity, perform well and are therefore com-
 2022 monly used as benchmarks. In detail, when a new instance is to be classified,
 2023 k -NN finds its k nearest neighbors in the training set and returns their majority
 2024 label among them. k -NN is considered a lazy learner because the training steps
 2025 involve only memorizing all the instances verbatim; no higher-level concepts have
 2026 been learned. In addition, in time series forecasting, a recent study demonstrates
 2027 that a well-known machine learning baseline, Gradient Boosting Regression Tree
 2028 (GBRT), such as XGBoost, equipped with an appropriate data engineering of the
 2029 data, can achieve competitive or even superior performance than the deep learning
 2030 method. In detail, they transform the time series forecasting task into a window-
 2031 based regression problem, as shown in Figure 5.1. For each training window of
 2032 length w with the last time point \mathbf{y}_i , and its lagged values $\mathbf{y}_{i-1}, \mathbf{y}_{i-2}, \dots, \mathbf{y}_{i-w+1}$ are
 2033 concatenated with covariates $x_i^1, x_i^2, \dots, x_i^M$ to form a *predictor* for a multi-output
 2034 GBRT. This transformation is called flattening. The corresponding response is the
 2035 following h points of \mathbf{y}_i . It provides a simple, more efficient yet accurate method
 2036 for time series forecasting.

2037 Moreover, k -NN has also shown to be a promising method for time series fore-
 2038 casting [84]. The k -NN uses the lagged values of the last time point to form a
 2039 query Q . It identifies the k previous similar subsequences to Q and uses their

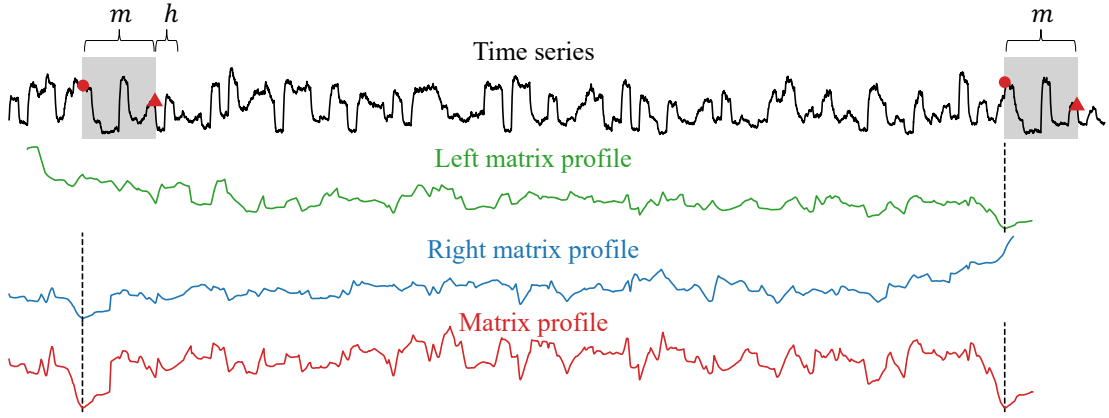


Figure 5.2: The **left** (**right**) matrix profile and the **matrix profile** of a time series. The **matrix profile** shows the distances between each m -subsequence and its nearest neighbor, where m is a user-given value. The **left** (**right**) matrix profile shows the same information but is limited to its left (right) nearest neighbor. For a particular m -subsequence shown by the right gray box, its nearest neighbor is the left gray box, as indicated by the dashed line in the **left matrix profile** and the **matrix profile**. Similarly, the nearest neighbor of the left gray box is the right gray box, as indicated by the dashed line in the **right matrix profile** and the **matrix profile**. The first (last) point in each box is denoted by a red circle (triangle). h denotes the length of the immediate subsequence of the nearest neighbor. Intuitively, this subsequence should be similar to the immediate subsequence (i.e., future) of the right gray box. To note, the **left** (**right**) matrix profile starts (ends) at a later (earlier) index because the corresponding nearest neighbor with length m does not exist.

Algorithm 6 The brute force approach to compute Matrix Profile

```

1: for  $i \leftarrow 1$  to  $n - m + 1$  do
2:   for  $j \leftarrow 1$  to  $n - m + 1$  do
3:     Compute the z-normalized Euclidean distance between  $t_{i,m}$  and  $t_{j,m}$ .

```

immediate subsequences to predict the immediate subsequence, which is the forecasting window, of Q . The intuition is that history repeats itself. The previous (historical) subsequences that are similar to Q can provide a hint about the future of Q . They are similar, and so are their immediate subsequences. Figure 5.2 depicts this idea. Observe that the immediate subsequence of the right gray box is similar to that of the left gray box. The left gray box is the nearest neighbor of the right gray in the “past”. 2040
2041
2042
2043
2044
2045
2046

Based on these findings, this study proposes a method to improve the performance of existing forecasters by leveraging information from the nearest neighbors of each subsequence in the target variable. For each time point y_i of the target variable Y , a window of length w is constructed with y_i as the last point, then 2047
2048
2049
2050

2051 we retrieve the window’s historical nearest neighbors and use their information to
2052 create new covariates for the window. The information includes the similarities
2053 between the window and its nearest neighbors, as well as the immediate subse-
2054 quences of them. The similarity can be interpreted as a measure of confidence
2055 or weight in using the information from the corresponding nearest neighbor. The
2056 intuition is that, if the similarity of the window and a neighbor is high, then the
2057 future (i.e., immediate subsequence) of the neighbor should also be similar to the
2058 future of the window. The fundamental difference between this study and pre-
2059 vious approaches [85, 84, 86] is that they directly use the subsequent points for
2060 prediction, whereas we use the nearest neighbor information for each subsequence
2061 as covariates, which are used as primitives for other forecasters. We explain this
2062 subtle difference by Figure 5.2. The previous approaches simply use the informa-
2063 tion of the nearest neighbors of the last look-back window, which consisted of the
2064 last time point and its lagged values (i.e., the right gray box), for prediction. In
2065 contrast, we use the information of the nearest neighbors of **all** of the windows.

2066 We use the Matrix Profile [87, 88] to annotate the nearest neighbor for each
2067 m -subsequence of a time series T of length n . The distance is the z-normalized
2068 Euclidean distance. It may seem computationally expensive to perform this an-
2069 notation at first glance. Algorithm 6 shows the brute force approach to compute
2070 the matrix profile. The two for-loops and the computation of z-normalized Eu-
2071 clidean distance, which takes $\mathcal{O}(m)$, indicate that the computational complexity
2072 is $\mathcal{O}(n^2m)$. The space complexity is $\mathcal{O}(n^2)$ because of the pairwise distance of
2073 each subsequence with the other subsequence. However, the matrix profile can be
2074 computed in $\mathcal{O}(n^2)$ using an exact method, namely STOMP [87] or its community-
2075 open-sourced version, STUMP [89]. Besides, the running time can be further sped
2076 up by parallelization for a single machine with multiple computation units, such as
2077 CPUs or GPUs. The tool also allows us to compute the left matrix profile to find
2078 the left nearest neighbor of each window. To note, the matrix profile annotates
2079 a time series with information about the nearest neighbor of each subsequence,
2080 including the similarity with its nearest neighbor and its location, as shown in
2081 Figure 5.2.

2082 In this study, we make the following contributions:

- 2083 • We are the first to propose leveraging the matrix profile to create meaningful
2084 covariates that improve forecaster performance.

- We have proposed two methods namely, GBRT-NN, which uses the immediate subsequence as the covariates, and GBRT-NN-S, which also involves the similarity on top of GBRT-NN, as the covariates. 2085
2086
2087
- Experimental results show that our approach can improve the GBRT fore- 2088
caster in most cases, with a very small cost to compute the matrix profile. 2089

The rest of this study is organized as follows. Section 5.2 presents the related- 2090
work. In Section 5.3, we introduce the necessary background knowledge, then 2091
introduce our method. Section 5.4 contains an empirical evaluation. Finally, we 2092
conclude this study and provide future work in Section 5.5. 2093

5.2 Related Work

Many methods have been developed for time series forecasting. Traditional meth- 2095
ods include rolling averages (RA), vector auto-regression (VAR) [74, 90], and auto- 2096
regressive integrated moving averages (ARIMA) [2, 91, 90]. Because of their rigor- 2097
ous statistical properties, they have long been the standard. The shortcomings of 2098
ARIMA and its variants include their high computational cost [74]. In contrast, 2099
VAR is arguably the most widely used method, particularly in multivariate time 2100
series analysis, owing to its simplicity. However, most of these traditional ap- 2101
proaches have certain limitations. They perform well when the data meet specific 2102
statistical assumptions, such as stationarity [92], which means that the mean and 2103
variance of the time series remain constant over time. It motivates the commu- 2104
nity to develop machine learning methods, particularly deep learning methods for 2105
time series forecasting. Many deep learning models have been proposed, including 2106
RNN-based models, CNN-based models, GNN-based models, Transformer-based 2107
models, and compound models that incorporate different base models mentioned 2108
before [79]. The compound models are promising. For example, RNNs are well 2109
suited to capturing long-term dependencies, whereas CNNs are well suited to 2110
capturing short-term dependencies. A good way to improve performance is to 2111
compound them. For example, LSTnet [74] integrates CNN, RNN, and autore- 2112
gressive [93] techniques to extract both short-term and long-term patterns. Using 2113
the occupancy rate of a freeway as an example [74] to explain these two patterns, 2114
the “short-term” patterns refer to the morning peaks against evening peaks, while 2115
the “long-term” patterns refer to the workday patterns against weekend patterns. 2116
Clearly, a good forecaster needs to capture and distinguish both kinds of patterns. 2117
Despite the superior performance deep learning methods have achieved, they tend 2118

2119 to be overly complex, opaque, and incur high computational costs compared to
2120 traditional techniques.

2121 5.3 Method

2122 In this section, we first formulate the time series forecasting problem, followed
2123 by the evaluation method. We then explain how to use a Gradient Boosting Re-
2124 gression Tree (GBRT) for forecasting. Subsequently, we discuss how to leverage
2125 the nearest neighbors' information of each subsequence to improve GBRT's per-
2126 formance. Finally, we discuss how to compute those nearest neighbors using the
2127 Matrix Profile.

2128 To begin, we define the data type of interest: time series.

2129 **Definition 10** (Time series). A *time series* $T = t_1, t_2, \dots, t_n$ is a sequence of
2130 real-valued numbers with length $= n$.

2131 In Definition 10, T is a univariate time series where each entry is a scalar
2132 number. If each entry is a vector consisting of scalar numbers with size > 1 , T is a
2133 multivariate time series. A multivariate time series can be regarded as a sequence
2134 of vectors. It can also be represented as a vector of univariate time series, where
2135 each univariate time series is referred to as a channel. In a dataset with more than
2136 one time series, we use T_i to denote a time series in a dataset with N time series,
2137 where $1 \leq i \leq N$.

2138 The local properties of T can be analyzed through its subsequences.

2139 **Definition 11** (Subsequence). A *subsequence* $T_{i,m} = t_i, t_{i+1}, \dots, t_{i+m-1} = t_{i:i+m-1}$
2140 of a T is a sequence that consists of a continuous subset of the entries from T of
2141 length m starting from i .

2142 5.3.1 Problem Formulation

2143 Time series forecasting is the task of predicting h -future values $y_{t+1}, y_{t+2}, \dots, y_{t+h}$
2144 of a target Y at the current time point t . In this study, there is only one target
2145 variable Y . h is the number of steps we want to predict in the future. The simplest
2146 case is one-step-ahead forecasting, where $h = 1$. The predicted value is denoted
2147 as \hat{y}_{t+1} where the actual value is y_{t+1} . It is preferable to predict multiple points in
2148 the future. It is called multi-horizon (multi-step) forecasting, where $h > 1$. The
2149 task of forecasting is encoded in Equation 5.1.

$$\hat{y}_{t+\tau} = f(y_{t-w+1:t}, x_{t-w+1:t}, u_{t-w+1:t+\tau}, \tau) \quad (5.1)$$

where

2150

- $\hat{y}_{t+\tau}$ is a prediction of the target value at $t + \tau$, where $\tau \in \{1, 2, \dots, h\}$.
2151
- $y_{t-w+1:t}$ are the actual values consisting of the current value y_t and the lag
2152 values before it. y_{t-i} is called the lag of i or i -lag.
2153
- x_t are inputs that can only be known historically at time t . x_{t+1} is not known
2154 at t .
2155
- u_t are known inputs for all time. For example, the date information such
2156 as the day of the week or month [92]. Even at t , u_{t+i} where $1 \leq i \leq \infty$ are
2157 known.
2158

x_t and u_t are called covariates of y_t . The input of Equation 5.1 is a look-back
2159 window w .
2160

We explain the task of forecasting in terms of Equation 5.1. The forecasting
2161 process estimates the value of $y_{t+\tau}$, denoted by $\hat{y}_{t+\tau}$ with the aim to minimize
2162 the error function, typically represented as a function of $y_{t+\tau} - \hat{y}_{t+\tau}$ for each τ .
2163 It is obvious that date information is useful when the target variable depends
2164 on when the measurement is taken. For example, if the target variable is the
2165 electricity consumption rate, there is a clear pattern by month: consumption is
2166 higher during the winter and summer months, when air conditioners and heaters
2167 are used. x_t provides additional information about the state of y_t . For example,
2168 if the target variable is the body temperature, and x_t tells us the severity of the
2169 sore throat, we may guess the body temperature will raise tomorrow.
2170

5.3.2 Evaluation Method

2171

Given a dataset D of N time series T_i , where $1 \leq i \leq N$, we explain how to
2172 evaluate the performance of a forecaster on T_i . The error made by the forecaster
2173 on D is simply the summation of errors made by the forecaster on each T_i . We
2174 now focus on a single time series; hence, we drop the index i . T is divided into
2175 two subsequences, namely training subsequence T_{train} and test subsequence T_{test} .
2176

In our study, the forecaster is only allowed to train on T_{train} . Recall that we
2177 are predicting the h future values from the w values just before them. Hence, we
2178 use a sliding window of length $w + h$ to generate the w -predictor- h -response pairs
2179 in T_{train} , enabling the forecaster to train on them. During the test (evaluation)
2180 phase, we do rolling forecasts. We predict based on the ground truth, not results
2181 generated from the model. It is used to prevent the accumulation of errors.
2182

2183 This concept is called “Teacher forcing” [94] because the teacher’s values are
 2184 “force fed” into the forecaster when we “roll” the forecaster on the T_{test} [95]. The
 2185 intuition is that, suppose each question (except the first one) in an exam depends
 2186 on the answers to the previous questions, rather than simply grading every answer
 2187 in the end, a teacher would grade (evaluate) the answer once it is given by the
 2188 student, and provide the correct answer to the student so he can answer the next
 2189 question based on the correct answer.

2190 To evaluate the forecaster, we used the following three evaluation metrics de-
 2191 fined as:

- 2192 • Root Mean Square Error (RMSE)

$$\text{RMSE} = \sqrt{\frac{1}{n} \sum_{i=1}^n (y_i - \hat{y}_i)^2} \quad (5.2)$$

- 2193 • Weighted Absolute Percentage Error (WAPE)

$$\text{WAPE} = \frac{\sum_{i=1}^n |y_i - \hat{y}_i|}{\sum_{i=1}^n |y_i|} \quad (5.3)$$

- 2194 • Mean Absolute Error (MAE)

$$\text{MAE} = \frac{1}{n} \sum_{i=1}^n |y_i - \hat{y}_i| \quad (5.4)$$

2195 where n is the length of the time series, y_i , \hat{y}_i is ground true value and predicted
 2196 value, respectively. RMSE and MAE are widely used metrics. MAE can better
 2197 reflect the actual error situation than RMSE [77]. WAPE was introduced by [96].
 2198 By rewriting Equation 5.3 to Equation 5.5, it is more obvious that it is a weighted
 2199 absolute percentage error.

$$\text{WAPE} = \sum_{i=1}^n w_i \frac{|y_i - \hat{y}_i|}{|y_i|} \quad (5.5)$$

2200 where the weights are given by

$$w_i = \frac{|y_i|}{\sum_{i=1}^n |y_i|} \quad (5.6)$$

2201 For all of them, a lower value is better.

5.3.3 Gradient Boosting Regression Tree (GBRT)

2202

Gradient boosting [97] is a boosting algorithm that ensembles a group of weak 2203 learners (usually decision trees) to make predictions. It sequentially adds learners 2204 to an ensemble, with each learner connecting its predecessor. It constructs weak 2205 learners in a way that each learner strategically corrects the predecessor’s mistakes 2206 by fitting the new learner to the residual errors made by the predecessor [98, 99]. 2207 It can be used in classification and regression. In this study, we focus on its use 2208 in regression. For the usage in regression, the model is called “Gradient Boosting 2209 Regression Tree (GBRT)”. Some popular optimized implementations of gradient 2210 boosting are XGBoost [100], CatBoost [101], and LightGBM [102]. In this study, 2211 we use XGBoost. 2212

In order to apply GBRT into time series forecasting problem, we need to cast 2213 the input into an appropriate format to input into GBRT. The casting approach 2214 is similar to successful time-series forecasting models, which reconfigure the time 2215 series into windowed inputs [2]. Figure 5.1 presents the reconfiguration. For each 2216 entry of the target variable y_i , we retrieve its u_i , such as the day information from 2217 the calendar. Hence, for each y_i , it is associated with x_i and u_i . To simplify 2218 the notation, we absorb u_i into x_i , and it is called the covariates of y_i . The 2D 2219 window, as shown on the left-hand side in Figure 5.1, with size $w \times M$, where M 2220 is the total number of covariates, is flattened into a 1D array on the right-hand 2221 side with length $w + M$. To note, as suggested in the literature [2], only the 2222 covariates of the last time-point i are kept and appended to the final vector. By 2223 reconfiguration, we obtain the predictor-response pairs for training. In detail, the 2224 predictor is $\textcolor{red}{y_{i-w+1}, y_{i-w+2}, \dots, y_i}$, $\textcolor{blue}{x_i^1, x_i^2, \dots, x_i^M}$ where the red part refers to the 2225 current target value $\textcolor{red}{y_i}$ and its lag values, and the blue part refers to the covari- 2226 ates of $\textcolor{red}{y_i}$. The corresponding output is $y_{i+1}, y_{i+2}, \dots, y_{i+h}$, with length = h . We 2227 predict the h -horizon from the w -look back window (i.e., $w + M$ -flattened predic- 2228 tor). With this predictor-response formulation, the forecasting problem becomes 2229 a multi-output regression problem. Standard XGBoost cannot return a sequence 2230 of predicted values; it only returns a single number [2]. To note, a multi-output re- 2231 gression problem is simply a group of single-output regression problems. In other 2232 words, XGBoost internally simply treats the prediction of h -steps as h individual 2233 problems. Hence, the final output is produced by the h regressors rather than 2234 by a single model. One may argue that the h regressors operate individually and 2235 hence the temporal relationship in the output sequence is lost. However, as the 2236

2237 individual regressors are trained on the same flattened input, the prediction would
2238 still preserve the temporal relationship [2].

2239 5.3.4 Matrix Profile

2240 Our proposed method has a simple intuition. We would like to create covariates for
2241 each time point in the time series, as in the case of using the date information to
2242 create the covariates. For example, given the timepoint date (2026-02-01, 14:38),
2243 we can deduce the minute (38), hour (14), day (1), month (2), and year (2026).
2244 Besides, by reading the calendar, the day of the week (Sunday), the day of the year
2245 ($31+1=32$), the week of the year (the firth week in 2026) can also be obtained.
2246 Given a time point t_p in T , and a user-given m , we want to use the m -subsequence
2247 with t_p as the ending point as a query Q , and to find its left m -subsequence that
2248 is the nearest neighbor of Q . Hence, the immediate subsequence of the nearest
2249 neighbor informs us of the dynamics of the immediate subsequence of Q . In
2250 Figure 5.2, the red triangle in the right gray box is t_p and the right gray box is
2251 Q . We seek its leftmost nearest neighbor, which turns out to be the left gray box.
2252 Note that we would like to perform this operation for each point t_p in the time
2253 series T , $m \leq t_p \leq |T|$.

2254 We discuss how to use a data primitive called Matrix Profile [87, 88] for this
2255 operation. In brief, a matrix profile P is a time series that annotates an input time
2256 series T , storing the z-normalized Euclidean distance between each m -subsequence
2257 and its nearest neighbor in T . Besides, another supplementary time series, namely
2258 the Matrix Profile Index I , stores the location of the corresponding nearest neigh-
2259 bor. To begin with, we first define the distance profile of T .

2260 **Definition 12** (Distance profile). A *distance profile* $D_i = d_{i,1}, d_{i,2}, \dots, d_{i,n-m+1}$
2261 of a T is a vector of the Euclidean distances between a given subsequence $T_{i,m}$
2262 and each subsequences in T , where $d_{i,j}$ is the distance between $T_{i,m}$ and $T_{j,m}$,
2263 $1 \leq i, j \leq n - m + 1$.

2264 The distances are measured between z-normalized time series. Equipped with
2265 the distance profile, we know all the Euclidean distances between a given subse-
2266 quence $T_{i,m}$ and each subsequences in T . From this, we define the matrix profile
2267 P and its supplementary matrix profile index I as follows.

2268 **Definition 13** (Matrix profile). A *matrix profile* $P = \min(D_1), \min(D_2), \dots,$
2269 $\min(D_{n-m+1})$ of T is a vector of Euclidean distances between every subsequence
2270 $T_{i,m}$ of T and its nearest neighbor in T .

Definition 14 (Matrix profile index). A *matrix profile index* $I = I_1, I_2, \dots, I_{n-m+1}$ of T is a vector of integers, where $I_i = j$ if $d_{i,j} = \min D_i$.

In this study, instead of the general matrix profile (index), we are interested in the left version of it. The left version of the matrix profile informs us of the information about the left nearest neighbor of any m -subsequences in T . It is shown in Figure 5.2. The left matrix profile has high values in the beginning because they can only find the left neighbor, and there are few left subsequences. In contrast, right matrix profile has low values in the beginning because there are many right subsequences. To note, each entry i in Matrix Profile P_i is simply the min of P_i^L and P_i^R (i.e., $P_i = \min(P_i^L, P_i^R)$).

Definition 15 (Left distance profile). A *left distance profile* $D_i^L = d_{i,1}, d_{i,2}, \dots, d_{i,i-\lceil m/4 \rceil - 1}$ of T is a vector of Euclidean distances between a given subsequence $T_{i,m}$ and each subsequence that appears before $T_{i,m}$. To note, $i - \lceil m/4 \rceil - 1$ is the index location of the last eligible subsequence before $T_{i,m}$ because of the exclusion zone.

We discuss the idea of an exclusion zone. For a given m -subsequence Q , the distance profile is zero at the location of Q (because Q must be a nearest neighbor of Q) and close to zero just before and after it. But the corresponding m -subsequences are trivial matches of Q . We need to define a zone, namely an exclusion zone, for this region. It is defined as $m/2$ before and after the location of Q [87]. The community implementation uses $m/4$ instead [89].

Definition 16 (Left matrix profile). A *left matrix profile* $P^L = \min(D_1^L), \min(D_2^L), \dots, \min(D_{n-m+1}^L)$ of T is a vector of Euclidean distances between every subsequence $T_{i,m}$ of T and its nearest neighbor in T before it.

Definition 17 (Left matrix profile index). A *left matrix profile index* I^L is a vector of integers $I_1^L, I_2^L, \dots, I_{n-m+1}^L$ of T , where $I_i^L = j$ if $d_{i,j} = \min D_i^L$.

Note that the original indexing system in Matrix Profile uses the start point rather than the end point to define the subsequence. In Figure 5.2, the matrix profile is shown in the original definition. The gray boxes are associated with the start point. Hence, the red Matrix Profile starts at $t = 1$ rather than $t = m$. To facilitate our discussion, from now on, we refer to Matrix Profile and its variants using the index defined on the end point instead of the start point. Formally, we use the entries of Matrix Profile at $i - m + 1$ to be the matrix profile at i in our indexing system. Visually speaking, we shift the matrix profile to the right by $m - 1$.

2306 To conclude this part, given the left matrix profile (index), we can compute, for
 2307 each m -subsequence in T , the information on its left nearest neighbor, including its
 2308 similarity and location. Besides, with the location (it now refers to the end point
 2309 of the subsequence), we can retrieve the points after it and form the immediate
 2310 subsequence with length = h of the nearest neighbor.

2311 A natural setting for m and the size of the immediate subsequence would be
 2312 the w and h as defined in Figure 5.1, respectively.

2313 5.4 Experiments

Table 5.1: Dataset Statistics. N is the number of time series in the dataset, while $|T| = n$ is the length of each time series. “rate” refers to the measuring rate. w is the size of the look-back window. h is the size of the forecasting window, also known as the forecasting horizon. T_{train} is the training subsequence of T . T_{test} is the test subsequence of T . To note, $|T_{\text{train}}| + |T_{\text{test}}| = n$.

Dataset	Data			Forecasting Task		
	N	n	rate	w, h	$ T_{\text{train}} $	$ T_{\text{test}} $
Electricity [103]	70	26,136	hourly	24	25,968	168
Traffic [103]	90	10,560	hourly	24	10,392	168
PeMSD7 [103]	228	12,672	/5 mins	9	11,232	1,440
Exchange-Rate [74]	8	7,536	daily	24	6,048	1,488

2314 The code and data are available at <https://github.com/colemanyu/matri>
 2315 **x-profile-motif-forecasting**. In this study, we focus on univariate time series
 2316 forecasting. There is only one single target variable Y . We predict the future of
 2317 Y only based on the past of it. The dataset used is listed in Table 5.1. For each
 2318 time series T in the dataset, it is split into two contiguous time series, namely
 2319 $T_{\text{train}} = T(1 : \text{split})$ and $T_{\text{test}} = T(\text{split} + 1 : |T|)$, where split defines the training-
 2320 test split, which is shown in the column 6 in Table 5.1. To note, the N time
 2321 series in a dataset are considered as multiple, independent univariate time series
 2322 instead of a multivaraite time series with channels = N . The original covariates
 2323 are constructed from the timestamp information. The settings of w and h are
 2324 adopted from the original corresponding papers [2]. It is not necessary for them
 2325 to be the same.

2326 GBRT-NN refers to a model that incorporates immediate sequence informa-
 2327 tion. GBRT-NN-S refers to a model that incorporates immediate sequence infor-

mation with the similarity information. The experimental results are shown in 2328
Table 5.2 and Table 5.3. 2329

Table 5.2: Experimental Results without original covariates (bold represents the best result and underlined represents the second best) (* refers to the results reported from [2]).

Dataset	Metric	LSTNet* [74]	TRMF* [104]	DARNN* [105]	ARIMA* [106]	GBRT [2]	GBRT-NN	GBRT-NN-S
Electricity [103]	RMSE	1095.309	<u>136.400</u>	404.056	181.210	136.254	142.035	138.354
	WAPE	0.997	0.095	0.343	0.310	0.103	0.101	<u>0.100</u>
	MAE	474.845	53.250	194.449	154.390	57.929	56.464	<u>55.972</u>
Traffic [103]	RMSE	0.042	0.023	0.015	0.044	<u>0.012</u>	0.016	0.008
	WAPE	0.102	0.161	0.132	0.594	0.108	<u>0.079</u>	0.037
	MAE	0.014	0.009	0.007	0.032	0.006	<u>0.004</u>	0.002
PeMSD7 [103]	RMSE	55.405	5.462	5.983	15.357	5.610	5.575	<u>5.557</u>
	WAPE	0.981	<u>0.057</u>	0.060	0.183	0.051	0.051	0.051
	MAE	53.336	3.329	3.526	10.304	2.984	<u>2.965</u>	2.957
Exchange-Rate [74]	RMSE	0.018	0.018	0.025	0.123	0.020	<u>0.019</u>	<u>0.019</u>
	WAPE	0.017	0.015	0.022	0.170	<u>0.016</u>	0.015	0.015
	MAE	0.013	0.011	0.016	0.101	<u>0.012</u>	<u>0.011</u>	<u>0.012</u>

Table 5.3: Experimental Results with original covariates (bold represents the best result and underlined represents the second best) (* refers to the results reported from [2]).

Dataset	Metric	DeepGlo* [103]	GBRT [2]	GBRT-NN	GBRT-NN-S
Electricity [103]	RMSE	141.285	132.669	123.591	<u>124.215</u>
	WAPE	0.094	0.0929	0.089	0.089
	MAE	53.036	52.0232	49.606	<u>49.739</u>
Traffic [103]	RMSE	0.026	<u>0.014</u>	0.018	0.009
	WAPE	0.239	0.109	<u>0.101</u>	0.062
	MAE	0.013	0.006	<u>0.006</u>	0.003
PeMSD7 [103]	RMSE	6.490	5.191	<u>5.163</u>	5.156
	WAPE	<u>0.070</u>	0.048	0.048	0.048
	MAE	3.530	2.796	<u>2.779</u>	2.778
Exchange-Rate [74]	RMSE	0.038	<u>0.020</u>	0.019	0.019
	WAPE	0.038	<u>0.016</u>	0.015	0.015
	MAE	<u>0.029</u>	0.012	0.012	0.012

5.5 Concluding Remarks

5.5.1 Future Work

Leveraging nearest neighbors' location information: It would be beneficial 2332 to retrieve the nearest neighbors for each subsequence in a specific range with 2333 respect to it. Real-world applications often require the separation of information of 2334 short-term and long-term repeating patterns for making accurate predictions [74]. 2335

2336 Notably, the matrix profile also provides the locations of the nearest neighbors from
2337 the matrix profile index. Using this location (index) information, we can retrieve
2338 the nearest neighbors of each subsequence in a specified range with respect to it
2339 to find those “short-term” and “long-term” patterns.

2340 **Extend to multidimensional case:** This study focuses on univariate time series
2341 forecasting, where there is a single target and no exogenous inputs. It only requires
2342 us to find one-dimensional nearest neighbors. When there are multiple targets or a
2343 single target with multiple exogenous inputs, we need to identify multidimensional
2344 nearest neighbors [107] and leverage their information for forecasting.

2345 **Top- k neighbors and motifs:** A simple extension is to consider the information
2346 not just from the nearest neighbor but from the k -nearest neighbors. Besides, we
2347 can use motifs instead of neighbors to obtain more stable “future” information for
2348 each window. Recall that a time series motif is a repeated pattern that consists
2349 of at least two occurrences. A motif can be considered as a family of nearest
2350 neighbors. A nearest neighbor is a historical occurrence that instantiates this motif.
2351 The motif captures the ideal behavior. By finding the occurrences of a motif and
2352 considering their immediate subsequences, we can make a more confident guess
2353 about this motif. We outline the approach for finding members of a motif¹. Given
2354 a subsequence A in a time series T , we denote the left-hand side of A in T as T_L .
2355 We find A ’s nearest neighbor in T_L , denoted as B . They are the two members of
2356 a motif M . We want to identify other subsequences in T_L that belong to M . We
2357 define a threshold $\theta = r \times \text{ED}(A, B)$, where $r > 1$. The center M_C of M is defined
2358 as the average of A and B . Then, we compute the distance profile between M_C
2359 and T_L . Any part of the distance profile that is smaller than θ points to a member
2360 of M in T_L . These members can then be added to M . After identifying all the
2361 members of M and excluding these members in the next consideration, we can find
2362 the next left nearest neighbor of A in T_L , and repeat the same process for finding
2363 the next motif. Given a set of immediate subsequences of members (occurrences)
2364 of M , we can compute a more stable immediate subsequence (future) associated
2365 with M by excluding the outliers among them or using the ensemble value, such
2366 as the mean or median of them, to cancel the noise.

2367 **Identify outliers of immediate subsequences:** When we have a set of im-
2368 mediate subsequences, we can determine whether an immediate subsequence is an
2369 outlier or not by comparing it with others. We provide a heuristic to identify an
2370 outlier as follows. Recall that the length of a nearest neighbor and its immediate
2371 subsequence is m and h , respectively. We concatenate all nearest neighbors into a

¹The idea has been mentioned in <https://www.cs.ucr.edu/~eamonn/TimeSeriesMotifs/>.

single long time series T' . To establish a clear boundary, we append a NaN value 2372 after each of them. It ensures that all matrix profile computations do not consider 2373 subsequences that span multiple neighbors. Then, we compute a distance profile 2374 of T' to find the nearest neighbor distance d_i of each neighbor i . Let S_i be the 2375 sequence consisting of neighbor i of length m and its immediate subsequence of 2376 length h . The expected nearest neighbor distance of S_i (found within the set of all 2377 extended sequences) should be proportional to the increase in length: $d_i \times \frac{m+h}{m}$. 2378 If the actual nearest neighbor distance of S_i is greater than $r' \times (d_i \times (m+h)/m)$ 2379 among the others, where r' is a user-given value, the immediate subsequence in S_i 2380 is considered as an outlier. 2381

Chapter 6

2382

Conclusion and Future Directions

2383

In this thesis, we contribute to time series analysis by addressing two aspects, with 2384 applications in bioinformatics. The first is to frame the prediction of biological 2385 sequence problems as time series classification tasks. The second addresses a 2386 fundamental limitation in existing time series distance measures. 2387

In the first study, we investigate the prediction of human Dicer cleavage sites. 2388 This task is important for the biogenesis of microRNAs (miRNAs). Accurate 2389 prediction of Dicer cleavage sites is crucial for elucidating mechanisms of post- 2390 transcriptional gene regulation. Computationally, this task is a classification prob- 2391 lem. First, we curate the dataset based on existing studies. The resulting datasets 2392 are 14-strings. Then, they are transformed into time series. We employ ROCKET- 2393 based classifiers for the classification. The main contributions are summarized as 2394 follows. We are the first to frame this problem as a multivariate time series classifi- 2395 cation problem. We introduced nine encoding methods for the transformation. In 2396 the transformation, to our surprise, we are the first to use the base-pair probabil- 2397 ities derived from the predicted secondary structure. We employ state-of-the-art 2398 time-series classifiers, namely ROCKET-based classifiers. They use random con- 2399 volutional kernels to generate the summary statistics and then use a simple ridge 2400 classifier to generate the final results. Because of the simplicity of the transforma- 2401 tion method and the classifiers we adopted, our framework, namely MTSCCleave, 2402 is fast. It achieved predictive performance comparable to or even better than 2403 deep learning-based state-of-the-art methods. Furthermore, MTSCCleave demon- 2404 strated substantial computational efficiency, with speedups ranging from 3.7X to 2405 28.8X relative to existing methods. We carried out perturbation-based experi- 2406 ments to identify the subsequence that are important for the classification. We 2407 found that regions near the center of the pre-miRNA secondary structure are most 2408 critical for Dicer cleavage site determination. It aligns with the existing study. Fu- 2409

ture work for this study is as follows. We make use of the predicted secondary structure information to construct the complementary strand and the base pair probability sequence for the input strand. However, there is more than one predicted secondary structure for the given RNA sequence. One future work is to make use of all potential secondary structures, each with its own pair probability sequence, and encode this data into a multivariate time series with more channels. Another area for future work is to use interpretable time series classifiers, such as those based on time series shapelets. By doing this, we can study which subsequence is critical for the definition of the classes, namely “5p cleav”, “5p non-cleav”, “3p leav”, and “3p non-cleav” because shapelets serve as the subsequence that has the most discriminating power between classes.

The second study develops a new distance measure framework, namely PSD. It aims to release a fundamental assumption that the prior studies have overlooked. There is only one scaling rate throughout the entire time series. However, there are much data that exhibits multiple rates. For example, human motion or music performance. They consist of phases. Each phase has its own expression rate. Existing distance measures cannot account for such variations. For example, DTW is designed for handling local distortions. US assumes that there is only one scaling factor in the whole series. To address this, we introduced the Piecewise Scaling Distance (PSD) framework, the first of its kind to account for multiple scaling factors. Recall that PSD is agnostic to the base measure we used. We can use any existing distance measure as the base measure. We studied the two instantiations of it. They are PSED (using Euclidean Distance as the base measure) and PSDTW (using DTW as the base measure). We provided an exact dynamic programming solution to compute PSD and three general ways to speed it up. In particular, we proposed a constrained version of it that limits the search space based on allowed segment lengths derived from scaling factor bounds. Besides, we use parallel computing and early abandoning to further accelerate it. For PSDTW, due to its quadratic complexity, we can further speed it up using lower-bounding techniques. Experiments show that PSD, and in particular PSED, perform best when the query contains multi-rate distortions, compared with ED, DTW and the other five DTW-based methods.

Future works on it are as follows. Currently, the number of segments P is given by users. It is preferable to develop a heuristic or algorithmic approach to automatically determine P . A simple heuristic is to test a range of possible P . Besides, while we have successfully applied a lower bound on PSDTW and accelerated it, the computational overhead of calculating a lower bound on PSED

outweighs the pruning benefit and makes the computation slower eventually. Developing a specialized lower bound for PSED could further improve its running time. In addition, some existing works on speeding up DTW such as “incremental DTW” can reuse the accumulated cost matrix D . However, it is challenging to apply a similar method to USDTW and PSDTW due to time series interpolation.

The third study develops a new method to create covariates for time series data using the immediate subsequences of the left nearest neighbor of each forecasting windows. We have studied the effect of the length of the immediate subsequences on the forecaster. Future work of this study includes finding nearest neighbors in a specific range to capture the short pattern and long pattern, extending the framework to a multivariate time series forecasting task, using motif family instead of simply top- k nearest neighbors, and how to handle the outliers among the immediate subsequences.

Bibliography

2460

- [1] M. Middlehurst, P. Schäfer, and A. Bagnall, “Bake off redux: A review and experimental evaluation of recent time series classification algorithms,” *Data Mining and Knowledge Discovery*, vol. 38, no. 4, pp. 1958–2031, Jul. 2024. 2461
2462
2463
- [2] S. Elsayed, D. Thyssens, A. Rashed, H. S. Jomaa, and L. Schmidt-Thieme, “Do we really need deep learning models for time series forecasting?” Oct. 2464
2465
2021. 2466
- [3] H. Sakoe and S. Chiba, “Dynamic programming algorithm optimization for spoken word recognition,” *IEEE Transactions on Acoustics, Speech, and Signal Processing*, vol. 26, no. 1, pp. 43–49, Feb. 1978. 2467
2468
2469
- [4] E. J. Keogh and M. J. Pazzani, “Derivative dynamic time warping,” in *Proceedings of the 2001 SIAM International Conference on Data Mining (SDM)*, ser. Proceedings. Society for Industrial and Applied Mathematics, Apr. 2001, pp. 1–11. 2470
2471
2472
2473
- [5] Y.-S. Jeong, M. K. Jeong, and O. A. Omitaomu, “Weighted dynamic time warping for time series classification,” *Pattern Recognition*, vol. 44, no. 9, pp. 2231–2240, Sep. 2011. 2474
2475
2476
- [6] J. Zhao and L. Itti, “**shapeDTW**: Shape dynamic time warping,” *Pattern Recognition*, vol. 74, pp. 171–184, Feb. 2018. 2477
2478
- [7] E. Keogh, K. Chakrabarti, M. Pazzani, and S. Mehrotra, “Dimensionality reduction for fast similarity search in large time series databases,” *Knowledge and Information Systems*, vol. 3, no. 3, pp. 263–286, Aug. 2001. 2479
2480
2481
- [8] B.-K. Yi and C. Faloutsos, “Fast time sequence indexing for arbitrary **Lp Norms**,” in *Proceedings of the 26th International Conference on Very Large Data Bases*, ser. VLDB ’00. San Francisco, CA, USA: Morgan Kaufmann Publishers Inc., Sep. 2000, pp. 385–394. 2482
2483
2484
2485

- 2486 [9] J. Zhao and L. Itti, “Decomposing time series with application to temporal
2487 segmentation,” in *2016 IEEE Winter Conference on Applications of Com-*
2488 *puter Vision (WACV)*, Mar. 2016, pp. 1–9.
- 2489 [10] M. Herrmann and G. I. Webb, “**Americing**: An intuitive and effective con-
2490 straint for dynamic time warping,” *Pattern Recognition*, vol. 137, p. 109333,
2491 May 2023.
- 2492 [11] L. A. Urry, M. L. Cain, S. A. Wasserman, P. V. Minorsky, R. B. Orr, and
2493 N. A. Campbell, *Campbell Biology*, twelfth ed. New York, NY: Pearson,
2494 2020.
- 2495 [12] B. Alberts, *Molecular Biology of the Cell*, 7th ed. New York: W. W. Norton
2496 & Company, 2022.
- 2497 [13] W. W. Cohen, *A Computer Scientist’s Guide to Cell Biology: A Travelogue*
2498 *from a Stranger in a Strange Land*. New York, NY: Springer-Verl, 2007.
- 2499 [14] Y. Lee, K. Jeon, J.-T. Lee, S. Kim, and V. N. Kim, “**MicroRNA** matura-
2500 tion: Stepwise processing and subcellular localization,” *The EMBO Journal*,
2501 vol. 21, no. 17, pp. 4663–4670, Sep. 2002.
- 2502 [15] S. Gu, L. Jin, Y. Zhang, Y. Huang, F. Zhang, P. N. Valdmanis, and M. A.
2503 Kay, “The loop position of **shRNAs** and **Pre-miRNAs** is critical for the
2504 accuracy of dicer processing *in vivo*,” *Cell*, vol. 151, no. 4, pp. 900–911, Nov.
2505 2012.
- 2506 [16] Y. Feng, X. Zhang, P. Graves, and Y. Zeng, “A comprehensive analysis of
2507 **Precursor microRNA** cleavage by human dicer,” *RNA*, vol. 18, no. 11,
2508 pp. 2083–2092, Nov. 2012.
- 2509 [17] I. J. MacRae, K. Zhou, and J. A. Doudna, “Structural determinants of **RNA**
2510 recognition and cleavage by dicer,” *Nature Structural & Molecular Biology*,
2511 vol. 14, no. 10, pp. 934–940, Oct. 2007.
- 2512 [18] F. Ahmed, R. Kaundal, and G. P. Raghava, “**PHDcleav**: A **SVM** based
2513 method for predicting human dicer cleavage sites using sequence and sec-
2514 ondary structure of **miRNA** precursors,” *BMC Bioinformatics*, vol. 14,
2515 no. 14, p. S9, Oct. 2013.

- [19] Y. Bao, M. Hayashida, and T. Akutsu, “**LBSizeCleav**: Improved support vector machine (**SVM**)-based prediction of dicer cleavage sites using loop/bulge length,” *BMC Bioinformatics*, vol. 17, no. 1, p. 487, Nov. 2016.
- [20] P. Liu, J. Song, C.-Y. Lin, and T. Akutsu, “**ReCGBM**: A gradient boosting-based method for predicting human dicer cleavage sites,” *BMC Bioinformatics*, vol. 22, no. 1, p. 63, Feb. 2021.
- [21] L. Mu, J. Song, T. Akutsu, and T. Mori, “**DiCleave**: A deep learning model for predicting human dicer cleavage sites,” *BMC Bioinformatics*, vol. 25, no. 1, p. 13, Jan. 2024.
- [22] L. Mu and T. Akutsu, “**DiCleavePlus**: A transformer-based model to detect human dicer cleavage sites within cleavage patterns,” *Genes to Cells*, vol. 31, no. 1, p. e70074, 2026.
- [23] S. Griffiths-Jones, H. K. Saini, and S. van Dongen, “**miRBase**: Tools for **microRNA** genomics,” *Nucleic Acids Research*, vol. 36, no. suppl_1, pp. D154–D158, Jan. 2008.
- [24] T. Xu, N. Su, L. Liu, J. Zhang, H. Wang, W. Zhang, J. Gui, K. Yu, J. Li, and T. D. Le, “**miRBaseConverter**: An r/bioconductor package for converting and retrieving **miRNA** name, accession, sequence and family information in different versions of **miRBase**,” *BMC Bioinformatics*, vol. 19, no. 19, p. 514, Dec. 2018.
- [25] M. J. Zvelebil, J. O. Baum, and M. Zvelebil, *Understanding Bioinformatics*. New York: Garland Science, 2008.
- [26] R. Lorenz, S. H. Bernhart, C. Höner zu Siederdissen, H. Tafer, C. Flamm, P. F. Stadler, and I. L. Hofacker, “**ViennaRNA** package 2.0,” *Algorithms for Molecular Biology*, vol. 6, no. 1, p. 26, Nov. 2011.
- [27] C. C. Aggarwal, *Data Mining: The Textbook*. Cham: Springer International Publishing, 2015.
- [28] G. Mendizabal-Ruiz, I. Román-Godínez, S. Torres-Ramos, R. A. Salido-Ruiz, and J. A. Morales, “On **DNA** numerical representations for genomic similarity computation,” *PLOS ONE*, vol. 12, no. 3, p. e0173288, Mar. 2017.
- [29] D. Anastassiou, “Genomic signal processing,” *IEEE Signal Processing Magazine*, vol. 18, no. 4, pp. 8–20, Jul. 2001.

- 2548 [30] T. Rakthanmanon, B. Campana, A. Mueen, G. Batista, B. Westover,
2549 Q. Zhu, J. Zakaria, and E. Keogh, “Searching and mining trillions of time
2550 series subsequences under dynamic time warping,” in *Proceedings of the 18th*
2551 *ACM SIGKDD International Conference on Knowledge Discovery and Data*
2552 *Mining*, ser. KDD ’12. New York, NY, USA: Association for Computing
2553 Machinery, Aug. 2012, pp. 262–270.
- 2554 [31] P. D. Cristea, “Conversion of nucleotides sequences into genomic signals,”
2555 *Journal of Cellular and Molecular Medicine*, vol. 6, no. 2, pp. 279–303, 2002.
- 2556 [32] N. Chakravarthy, A. Spanias, L. D. Iasemidis, and K. Tsakalis, “Autoregres-
2557 sive modeling and feature analysis of **DNA** sequences,” *EURASIP Journal*
2558 *on Advances in Signal Processing*, vol. 2004, no. 1, pp. 1–16, Dec. 2004.
- 2559 [33] J. Zhao, X. W. Yang, J. P. Li, and Y. Y. Tang, “**DNA** sequences clas-
2560 sification based on wavelet packet analysis,” in *Wavelet Analysis and Its*
2561 *Applications*. Springer, Berlin, Heidelberg, 2001, pp. 424–429.
- 2562 [34] T. Holden, R. Subramaniam, R. Sullivan, E. Cheung, C. Schneider, G. T. Jr,
2563 A. Flamholz, D. H. Lieberman, and T. D. Cheung, “**ATCG** nucleotide fluc-
2564 tuation of deinococcus radiodurans radiation genes,” in *Instruments, Meth-
2565 ods, and Missions for Astrobiology X*, vol. 6694. SPIE, Oct. 2007, pp.
2566 402–411.
- 2567 [35] A. S. Nair and S. P. Sreenadhan, “A coding measure scheme employing
2568 electron-ion interaction pseudopotential (**EIIP**),” *Bioinformation*, vol. 1,
2569 no. 6, pp. 197–202, Oct. 2006.
- 2570 [36] M. Akhtar, J. Epps, and E. Ambikairajah, “On **DNA** numerical represen-
2571 tations for period-3 based exon prediction,” in *2007 IEEE International*
2572 *Workshop on Genomic Signal Processing and Statistics*, Jun. 2007, pp. 1–4.
- 2573 [37] R. Zhang and C.-T. Zhang, “**Z Curves**, an intutive tool for visualizing
2574 and analyzing the **DNA** sequences,” *Journal of Biomolecular Structure and*
2575 *Dynamics*, vol. 11, no. 4, pp. 767–782, Feb. 1994.
- 2576 [38] J. A. Berger, S. K. Mitra, M. Carli, and A. Neri, “Visualization and analysis
2577 of **DNA** sequences using **DNA** walks,” *Journal of the Franklin Institute*,
2578 vol. 341, no. 1, pp. 37–53, Jan. 2004.

- [39] A. Bagnall, J. Lines, A. Bostrom, J. Large, and E. Keogh, “The great time series classification bake off: A review and experimental evaluation of recent algorithmic advances,” *Data Mining and Knowledge Discovery*, vol. 31, no. 3, pp. 606–660, May 2017. 2579
2580
2581
2582
- [40] A. P. Ruiz, M. Flynn, J. Large, M. Middlehurst, and A. Bagnall, “The great multivariate time series classification bake off: A review and experimental evaluation of recent algorithmic advances,” *Data Mining and Knowledge Discovery*, vol. 35, no. 2, pp. 401–449, Mar. 2021. 2583
2584
2585
2586
- [41] A. Dempster, F. Petitjean, and G. I. Webb, “**ROCKET**: Exceptionally fast and accurate time series classification using random convolutional kernels,” *Data Mining and Knowledge Discovery*, vol. 34, no. 5, pp. 1454–1495, Sep. 2020. 2587
2588
2589
2590
- [42] A. Dempster, D. F. Schmidt, and G. I. Webb, “**MiniRocket**: A very fast (almost) deterministic transform for time series classification,” in *Proceedings of the 27th ACM SIGKDD Conference on Knowledge Discovery & Data Mining*, ser. KDD ’21. New York, NY, USA: Association for Computing Machinery, Aug. 2021, pp. 248–257. 2591
2592
2593
2594
2595
- [43] C. W. Tan, A. Dempster, C. Bergmeir, and G. I. Webb, “**MultiRocket**: Multiple pooling operators and transformations for fast and effective time series classification,” *Data Mining and Knowledge Discovery*, vol. 36, no. 5, pp. 1623–1646, Sep. 2022. 2596
2597
2598
2599
- [44] A. Dempster, D. F. Schmidt, and G. I. Webb, “**Hydra**: Competing convolutional kernels for fast and accurate time series classification,” *Data Mining and Knowledge Discovery*, vol. 37, no. 5, pp. 1779–1805, Sep. 2023. 2600
2601
2602
- [45] B. W. Matthews, “Comparison of the predicted and observed secondary structure of **T4** phage lysozyme,” *Biochimica et Biophysica Acta (BBA) - Protein Structure*, vol. 405, no. 2, pp. 442–451, Oct. 1975. 2603
2604
2605
- [46] J. Gorodkin, “Comparing two k-category assignments by a k-category correlation coefficient,” *Computational Biology and Chemistry*, vol. 28, no. 5, pp. 367–374, Dec. 2004. 2606
2607
2608
- [47] T.-c. Fu, “A review on time series data mining,” *Engineering Applications of Artificial Intelligence*, vol. 24, no. 1, pp. 164–181, Feb. 2011. 2609
2610

- 2611 [48] C. Rose, B. Guenter, B. Bodenheimer, and M. F. Cohen, “Efficient genera-
2612 tion of motion transitions using spacetime constraints,” in *Proceedings of the*
2613 *23rd Annual Conference on Computer Graphics and Interactive Techniques*,
2614 ser. SIGGRAPH ’96. New York, NY, USA: Association for Computing
2615 Machinery, Aug. 1996, pp. 147–154.
- 2616 [49] Y. Li, T. Wang, and H.-Y. Shum, “**Motion Texture**: A two-level statistical
2617 model for character motion synthesis,” *ACM Trans. Graph.*, vol. 21, no. 3,
2618 pp. 465–472, Jul. 2002.
- 2619 [50] R. B. Dannenberg, W. P. Birmingham, G. P. Tzanetakis, C. P. Meek, N. P.
2620 Hu, and B. P. Pardo, “The **MUSART** testbed for query-by-humming eval-
2621 uation,” *Comput. Music J.*, vol. 28, no. 2, pp. 34–48, Jun. 2004.
- 2622 [51] K.-C. Li, M. Yan, and S. Yuan, “A simple statistical model for depicting
2623 the **Cdc15**-synchronized yeast cell-cycle regulated gene expression data,”
2624 *Statistica Sinica*, vol. 12, no. 1, pp. 141–158, 2002.
- 2625 [52] G. E. A. P. A. Batista, E. J. Keogh, O. M. Tataw, and V. M. A. de Souza,
2626 “**CID**: An efficient complexity-invariant distance for time series,” *Data Min-
2627 ing and Knowledge Discovery*, vol. 28, no. 3, pp. 634–669, May 2014.
- 2628 [53] A. W.-C. Fu, E. Keogh, L. Y. H. Lau, C. A. Ratanamahatana, and R. C.-
2629 W. Wong, “Scaling and time warping in time series querying,” *The VLDB
2630 Journal*, vol. 17, no. 4, pp. 899–921, Jul. 2008.
- 2631 [54] Y. Shen, Y. Chen, E. Keogh, and H. Jin, “Searching time series with invari-
2632 ance to large amounts of uniform scaling,” in *2017 IEEE 33rd International
2633 Conference on Data Engineering (ICDE)*, Apr. 2017, pp. 111–114.
- 2634 [55] ——, “Accelerating time series searching with large uniform scaling,” in
2635 *Proceedings of the 2018 SIAM International Conference on Data Mining
(SDM)*, ser. Proceedings. Society for Industrial and Applied Mathematics,
2636 May 2018, pp. 234–242.
- 2638 [56] C. C. Aggarwal and C. K. Reddy, Eds., *Data Clustering: Algorithms and
2639 Applications*, 1st ed. Boca Raton: Chapman and Hall/CRC, Aug. 2013.
- 2640 [57] P. Esling and C. Agon, “Time-series data mining,” *ACM Computing Sur-
2641 veys*, vol. 45, no. 1, pp. 1–34, Nov. 2012.

- [58] T. Rakthanmanon, B. Campana, A. Mueen, G. Batista, B. Westover, Q. Zhu, J. Zakaria, and E. Keogh, “Addressing big data time series: Mining trillions of time series subsequences under dynamic time warping,” *ACM Trans. Knowl. Discov. Data*, vol. 7, no. 3, pp. 10:1–10:31, Sep. 2013.
- [59] C. W. Tan, F. Petitjean, and G. I. Webb, “Elastic bands across the path: A new framework and method to lower bound **DTW**,” in *Proceedings of the 2019 SIAM International Conference on Data Mining (SDM)*, ser. Proceedings. Society for Industrial and Applied Mathematics, May 2019, pp. 522–530.
- [60] A. Shifaz, C. Pelletier, F. Petitjean, and G. I. Webb, “Elastic similarity and distance measures for multivariate time series,” *Knowledge and Information Systems*, vol. 65, no. 6, pp. 2665–2698, Jun. 2023.
- [61] S. Salvador and P. Chan, “Toward accurate dynamic time warping in linear time and space,” *Intelligent Data Analysis*, vol. 11, no. 5, pp. 561–580, Oct. 2007.
- [62] E. Keogh, T. Palpanas, V. B. Zordan, D. Gunopoulos, and M. Cardle, “Indexing large human-motion databases,” in *Proceedings of the Thirtieth International Conference on Very Large Data Bases - Volume 30*, ser. VLDB ’04. Toronto, Canada: VLDB Endowment, Aug. 2004, pp. 780–791.
- [63] D. Yankov, E. Keogh, J. Medina, B. Chiu, and V. Zordan, “Detecting time series motifs under uniform scaling,” in *Proceedings of the 13th ACM SIGKDD International Conference on Knowledge Discovery and Data Mining*, ser. KDD ’07. New York, NY, USA: Association for Computing Machinery, Aug. 2007, pp. 844–853.
- [64] Y. Zhu and D. Shasha, “Warping indexes with envelope transforms for query by humming,” in *Proceedings of the 2003 ACM SIGMOD International Conference on Management of Data*, ser. SIGMOD ’03. New York, NY, USA: Association for Computing Machinery, Jun. 2003, pp. 181–192.
- [65] F. Itakura, “Minimum prediction residual principle applied to speech recognition,” *IEEE Transactions on Acoustics, Speech, and Signal Processing*, vol. 23, no. 1, pp. 67–72, Feb. 1975.

- 2673 [66] E. Keogh and C. A. Ratanamahatana, “Exact indexing of dynamic time
2674 warping,” *Knowledge and Information Systems*, vol. 7, no. 3, pp. 358–386,
2675 Mar. 2005.
- 2676 [67] S.-W. Kim, S. Park, and W. Chu, “An index-based approach for similarity
2677 search supporting time warping in large sequence databases,” in *Proceedings*
2678 *17th International Conference on Data Engineering*, Apr. 2001, pp. 607–614.
- 2679 [68] C. W. Tan, M. Herrmann, G. Forestier, G. I. Webb, and F. Petitjean, “Ef-
2680 ficient search of the best warping window for dynamic time warping,” in
2681 *Proceedings of the 2018 SIAM International Conference on Data Mining*
2682 (*SDM*), ser. Proceedings. Society for Industrial and Applied Mathematics,
2683 May 2018, pp. 225–233.
- 2684 [69] C. A. Ratanamahatana and E. Keogh, “Everything you know about dy-
2685 namic time warping is wrong,” in *3 Rd International Workshop on Mining*
2686 *Temporal and Sequential Data (TDM-04)*. Citeseer, 2004.
- 2687 [70] H. A. Dau, A. Bagnall, K. Kamgar, C.-C. M. Yeh, Y. Zhu, S. Gharghabi,
2688 C. A. Ratanamahatana, and E. Keogh, “The **UCR** time series archive,”
2689 *IEEE/CAA Journal of Automatica Sinica*, vol. 6, no. 6, pp. 1293–1305,
2690 Nov. 2019.
- 2691 [71] M. Middlehurst, A. Ismail-Fawaz, A. Guillaume, C. Holder, D. Guijo-Rubio,
2692 G. Bulatova, L. Tsaprounis, L. Mentel, M. Walter, P. Schäfer, and A. Bag-
2693 nall, “**Aeon**: A python toolkit for learning from time series,” *Journal of*
2694 *Machine Learning Research*, vol. 25, no. 289, pp. 1–10, 2024.
- 2695 [72] N. Tatbul, T. J. Lee, S. Zdonik, M. Alam, and J. Gottschlich, “Precision
2696 and recall for time series,” in *Advances in Neural Information Processing*
2697 *Systems*, vol. 31. Curran Associates, Inc., 2018.
- 2698 [73] M. Leodolter, C. Plant, and N. Brändle, “**IncDTW**: An R package for
2699 incremental calculation of dynamic time warping,” *Journal of Statistical*
2700 *Software*, vol. 99, pp. 1–23, Sep. 2021.
- 2701 [74] G. Lai, W.-C. Chang, Y. Yang, and H. Liu, “Modeling long- and short-term
2702 temporal patterns with deep neural networks,” in *The 41st International*
2703 *ACM SIGIR Conference on Research & Development in Information Re-*
2704 *trieval*, ser. SIGIR ’18. New York, NY, USA: Association for Computing
2705 Machinery, Jun. 2018, pp. 95–104.

- [75] C. Chatfield, *The Analysis of Time Series: An Introduction, Sixth Edition*, 2706
6th ed. New York: Chapman and Hall/CRC, Jul. 2003. 2707
- [76] O. Y. Al-Jarrah, P. D. Yoo, S. Muhaidat, G. K. Karagiannidis, and K. Taha, 2708
“Efficient machine learning for big data: A review,” *Big Data Research*, 2709
vol. 2, no. 3, pp. 87–93, Sep. 2015. 2710
- [77] W. Li and K. L. E. Law, “Deep learning models for time series forecasting: 2711
A review,” *IEEE Access*, vol. 12, pp. 92 306–92 327, 2024. 2712
- [78] N. I. Sapankevych and R. Sankar, “Time series prediction using support 2713
vector machines: A survey,” *IEEE Computational Intelligence Magazine*, 2714
vol. 4, no. 2, pp. 24–38, May 2009. 2715
- [79] Z. Chen, M. Ma, T. Li, H. Wang, and C. Li, “Long sequence time-series 2716
forecasting with deep learning: A survey,” *Information Fusion*, vol. 97, p. 2717
101819, Sep. 2023. 2718
- [80] J. F. Torres, D. Hadjout, A. Sebaa, F. Martínez-Álvarez, and A. Troncoso, 2719
“Deep learning for time series forecasting: A survey,” *Big Data*, vol. 9, no. 1, 2720
pp. 3–21, Feb. 2021. 2721
- [81] D. B. da Silva, D. Schmidt, C. A. da Costa, R. da Rosa Righi, and B. Es- 2722
kofier, “Deepsigns: A predictive model based on deep learning for the early 2723
detection of patient health deterioration,” *Expert Systems with Applications*, 2724
vol. 165, p. 113905, Mar. 2021. 2725
- [82] N. Wu, B. Green, X. Ben, and S. O’Banion, “Deep transformer models for 2726
time series forecasting: The influenza prevalence case,” Jan. 2020. 2727
- [83] F. Martínez-Álvarez, G. Asencio-Cortés, J. F. Torres, D. Gutiérrez-Avilés, 2728
L. Melgar-García, R. Pérez-Chacón, C. Rubio-Escudero, J. C. Riquelme, 2729
and A. Troncoso, “Coronavirus optimization algorithm: A bioinspired meta- 2730
heuristic based on the **COVID-19** propagation model,” *Big Data*, vol. 8, 2731
no. 4, pp. 308–322, Aug. 2020. 2732
- [84] F. Martínez, M. P. Frías, M. D. Pérez, and A. J. Rivera, “A methodology for 2733
applying k-nearest neighbor to time series forecasting,” *Artificial Intelligence 2734
Review*, vol. 52, no. 3, pp. 2019–2037, Oct. 2019. 2735

- 2736 [85] S. Tajmouati, B. E. L. Wahbi, A. Bedoui, A. Abarda, and M. Dakkon, “Ap-
2737 plying k-nearest neighbors to time series forecasting: Two new approaches,”
2738 *Journal of Forecasting*, vol. 43, no. 5, pp. 1559–1574, 2024.
- 2739 [86] D. T. Thi, N. T. Phong, and N. D. Bui, “Forecast timeseries based on matrix
2740 profile,” *Journal of Informatics and Innovative Technologies (JIIT)*, 2021.
- 2741 [87] C.-C. M. Yeh, Y. Zhu, L. Ulanova, N. Begum, Y. Ding, H. A. Dau, D. F.
2742 Silva, A. Mueen, and E. Keogh, “Matrix profile i: All pairs similarity
2743 joins for time series: A unifying view that includes motifs, discords and
2744 shapelets,” in *2016 IEEE 16th International Conference on Data Mining*
2745 (*ICDM*). Barcelona, Spain: IEEE, Dec. 2016, pp. 1317–1322.
- 2746 [88] Y. Zhu, M. Imamura, D. Nikovski, and E. Keogh, “Matrix profile vii: Time
2747 series chains: A new primitive for time series data mining,” in *2017 IEEE*
2748 *International Conference on Data Mining (ICDM)*, Nov. 2017, pp. 695–704.
- 2749 [89] S. M. Law, “**STUMPY**: A powerful and scalable python library for time
2750 series data mining,” *Journal of Open Source Software*, vol. 4, no. 39, p. 1504,
2751 Jul. 2019.
- 2752 [90] G. E. P. Box, G. M. Jenkins, G. C. Reinsel, and G. M. Ljung, *Time Series
2753 Analysis: Forecasting and Control*. John Wiley & Sons, May 2015.
- 2754 [91] G. E. P. Box and D. A. Pierce, “Distribution of residual autocorrelations
2755 in autoregressive-integrated moving average time series models,” *Journal of
2756 the American Statistical Association*, vol. 65, no. 332, pp. 1509–1526, 1970.
- 2757 [92] B. Lim and S. Zohren, “Time-series forecasting with deep learning: A
2758 survey,” *Philosophical Transactions of the Royal Society A: Mathematical,
2759 Physical and Engineering Sciences*, vol. 379, no. 2194, p. 20200209, Feb.
2760 2021.
- 2761 [93] G. U. Yule, “On a method of investigating periodicities in disturbed series,
2762 with special reference to Wolfer’s sunspot numbers,” *Philosophical Trans-
2763 actions of the Royal Society of London. Series A, Containing Papers of a
2764 Mathematical or Physical Character*, vol. 226, pp. 267–298, 1927.
- 2765 [94] R. J. Williams and D. Zipser, “A learning algorithm for continually running
2766 fully recurrent neural networks,” *Neural Computation*, vol. 1, no. 2, pp.
2767 270–280, Jun. 1989.

- [95] K. P. Murphy, *Probabilistic Machine Learning: An Introduction*, ser. Adaptive Computation and Machine Learning. Cambridge, Massachusetts London, England: The MIT Press, 2022. 2768
2769
2770
- [96] S. Kolassa and W. Schütz, “Advantages of the **MAD**/mean ratio over the **MAPE**,” *Foresight: The International Journal of Applied Forecasting*, vol. 6, pp. 40–43, 2007. 2771
2772
2773
- [97] J. H. Friedman, “Greedy function approximation: A gradient boosting machine.” *The Annals of Statistics*, vol. 29, no. 5, pp. 1189–1232, Oct. 2001. 2774
2775
- [98] L. G. Serrano and S. Thrun, *Grokking Machine Learning*. Shelter Island: 2776
Manning, 2021. 2777
- [99] A. Géron, *Hands-On Machine Learning with Scikit-Learn and PyTorch: Concepts, Tools, and Techniques to Build Intelligent Systems*. US: O'Reilly 2778
Media, 2025. 2779
2780
- [100] T. Chen and C. Guestrin, “**XGBoost**: A scalable tree boosting system,” in *Proceedings of the 22nd ACM SIGKDD International Conference on Knowledge Discovery and Data Mining*, ser. KDD '16. New York, NY, USA: 2781
Association for Computing Machinery, Aug. 2016, pp. 785–794. 2782
2783
2784
- [101] A. V. Dorogush, V. Ershov, and A. Gulin, “**CatBoost**: Gradient boosting with categorical features support,” in *Workshop on ML Systems at NIPS 2017*, 2017. 2785
2786
2787
- [102] G. Ke, Q. Meng, T. Finley, T. Wang, W. Chen, W. Ma, Q. Ye, and T.-Y. Liu, “**LightGBM**: A highly efficient gradient boosting decision tree,” in *Advances in Neural Information Processing Systems*, vol. 30. Curran 2788
Associates, Inc., 2017. 2789
2790
2791
- [103] R. Sen, H.-F. Yu, and I. S. Dhillon, “Think globally, act locally: A deep neural network approach to high-dimensional time series forecasting,” in *Advances in Neural Information Processing Systems*, vol. 32. Curran As- 2792
sociates, Inc., 2019. 2793
2794
2795
- [104] H.-F. Yu, N. Rao, and I. S. Dhillon, “Temporal regularized matrix factorization for high-dimensional time series prediction,” in *Advances in Neural Information Processing Systems*, vol. 29. Curran Associates, Inc., 2016. 2796
2797
2798

- 2799 [105] Y. Qin, D. Song, H. Cheng, W. Cheng, G. Jiang, and G. W. Cottrell, “A
2800 dual-stage attention-based recurrent neural network for time series predic-
2801 tion,” in *Proceedings of the 26th International Joint Conference on Artificial*
2802 *Intelligence*, ser. IJCAI’17. Melbourne, Australia: AAAI Press, Aug. 2017,
2803 pp. 2627–2633.
- 2804 [106] S. Makridakis and M. Hibon, “**ARMA** models and the **Box–Jenkins**
2805 methodology,” *Journal of Forecasting*, vol. 16, no. 3, pp. 147–163, 1997.
- 2806 [107] C.-C. M. Yeh, N. Kavantzas, and E. Keogh, “Matrix profile vi: Meaningful
2807 multidimensional motif discovery,” in *2017 IEEE International Conference*
2808 *on Data Mining (ICDM)*, Nov. 2017, pp. 565–574.